Centre Val de Loire UNIVERSITÉ
Spirit of the Loire Valley

UNIVERSITÉ D'ORLÉANS

UNIVERSITE D'ORLEANS

ÉCOLE DOCTORALE MIPTIS

Laboratoire PRISME

THÈSE présentée par :

Grégory Hellbourg

soutenue le : **31 janvier 2014**

pour obtenir le grade de : **Docteur de l'Université d'Orléans**

Discipline/ Spécialité : **Automatique et Traitement du Signal**

Traitement spatial des interférences pour les radiotélescopes de nouvelle génération

Radio Frequency Interference spatial processing for modern radio telescopes

THÈSE dirigée par:

Rachid HARBA	Professeur, Université d'Orléans
Gilles THEUREAU	Astronome, OSUC

RAPPORTEURS:

Asoke NANDI	Professeur, Brunel University, UK
Amir LESHEM	Professeur, Bar-Ilan University, Israel

JURY:

Karim ABED-MERAIM	Professeur, Université d'Orléans - Président
Rodolphe WEBER	Maître de conférence, Université d'Orléans
Albert-Jan BOONSTRA	Directeur de recherche, ASTRON, The Netherlands
David VALLS-GABAUD	Directeur de recherche, Observatoire de Paris-Meudon


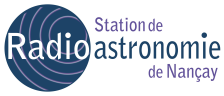

Radio Frequency Interference Spatial Processing for Modern Radio Telescopes

Grégory Hellbourg

PhD Directors
Professor Rachid Harba - University of Orléans
Professor Gilles Theureau - Nançay Observatory
PhD Advisors
Doctor Rodolphe Weber - University of Orléans
Doctor Albert-Jan Boonstra - ASTRON, The Netherlands
Doctor Cécile Capdessus - PRISME Laboratory
Professor Karim Abed-Meraim - University of Orléans

Contents

0.1 Acknowledgment

First of all, I would like to deeply thank Dr. Rodolphe Weber for giving me the opportunity to work on this project - but more than that - supervising, advising and mentoring me. It was really great to work with you.

I would like to thank my advisors Dr. Cécile Capdessus, Prof. Karim Abed-Meraim and Dr. Albert-Jan Boonstra for the discussions and the time spent helping me understanding and solving my problems. Thank you for having shared your large expertise with me.

Thank you Prof. Gilles Theureau and Prof. Rachid Harba for co-supervising my thesis, being here and assisting me.

Prof. Asoke Nandi and Prof. Amir Leshem, thank you so much for reviewing my thesis and for all the advices you provided me.

Prof. David Valls-Gabaud, thank you very much for having being part of my Ph.D. Committee.

Dr. Stephen Torchinsky, Mr. Christophe Taffoureau and Dr. Benjamin Censier, thank you for your amazing help with the RFI mitigation algorithm implementation on EMBRACE. Without you, nothing would have been done. Thank you.

Thank you Mrs. Elizabeth Rowley-Jolivet and Mrs. Sybille Dubois for your important help with correcting and improving my English.

Thank you also to Mrs. Sylvie Plessard, Mrs. Véronique Etieve, Mrs. Chantal Guillen, Mrs. Geneviève Béguin and Mrs. Laure Spina for taking care of different administrative and logistical problems I encountered at the University of Orléans and at the Nançay radio observatory.

Thank you to all the people I met at Prisme Laboratory, ASTRON and the Nançay radio observatory.

Thank you to my Friends in France and in the Netherlands, and to my Family. You cannot imagine how important you were during these last three years.

0.2 Notations

a	Scalar
$\mathbf{a}$	Vector
$\mathbf{A}$	Matrix
$\mathbf{I_{M\times M}}$	$M \times M$ identity matrix
$(.)^{-1}$	Inverse operator
$\dagger$	Moore-Penrose pseudo inverse operator
$(.)^*$	Conjugate operator
$(.)^T$	Transpose operator
$(.)^H$	Hermitian transpose operator
$\mathbb{E}\{.\}$	Expectation operator
$< . >_T$	Finite time average operator:
	$< . >_T = \frac{1}{T}\int_{-\frac{T}{2}}^{+\frac{T}{2}}(.)dt$ for continuous signals
	$< . >_T = \frac{1}{T}\sum_{-\frac{T}{2}}^{+\frac{T}{2}}(.)$ for discrete signals
$< . >_\infty$	Infinite time average operator:
	$< . >_\infty = \lim_{T\to\infty}\frac{1}{T}\int_{-\frac{T}{2}}^{+\frac{T}{2}}(.)dt$ for non-probabilistic processes
	$< . >_\infty = \mathbb{E}\{.\}$ for stochastic processes
$\lvert.\rvert$	Absolute value
$\lVert.\rVert$	Vector or matrix Euclidean norm
$\lVert.\rVert_F$	Frobenius norm
Re(.)	Real part
Rank(.)	Matrix rank
tr(.)	Matrix trace
vec(.)	Stacks the columns of a matrix into a vector
diag(.)	Stacks the diagonal coefficients of a matrix into a vector
undiag(.)	Transforms a vector into a diagonal matrix, where the vector becomes the diagonal of the matrix
$\circ$	Khatri-Rao product
$\odot$	Element-wise multiplication
$\oplus$	Direct sum
$\hat{(.)}$	Estimated value
$\mathbf{1}_{M\times 1}$	$(M \times 1)$ vector containing ones

Chapter 1

Introduction

1.1 Radio astronomy

For a long time, astronomy was limited to optical astronomy, i.e. astronomy based on observations made with optical telescopes. In the late XIX$^{\text{th}}$ century, Sir Oliver Lodge [70, 49] had an intuition about radio waves emitted by extraterrestrial sources, and particularly the sun.

Almost half a century later, radio astronomy was born with Karl Jansky [58]. Jansky, an engineer at Bell Laboratories, was working on a project regarding radio interference during transatlantic communications when he discovered the first radio emission from an extraterrestrial source : the Milky Way.

In the spectral sense, two types of cosmic emissions exist in radio astronomy : continuum emissions and spectral lines:

- Continuum emissions correspond to broa dBand radiation, i.e. radiation slowly varying over the wavelengths. Their origin is either thermal or non-thermal. Thermal radiation means that the emission of a cosmic object depends on its temperature. Non-thermal radiation can be of various kinds, such as synchrotron radiation (when particles close to the speed of light cross a magnetic field) for instance.

- Spectral line emissions are narrow band radiation due to quantum state changes in atomic or molecular components of a cosmic source. They provide information about the composition of a cosmic source, but also about its movement and expansion.

In the temporal sense, cosmic signals are either classified as continuous emissions or transients (e.g. pulsars).

1.2 Radio astronomy instrumentation

1.2.1 Single dish radio telescopes

The first single dish radio telescope was built by Grote Reber in 1937. He conducted the first radio sky survey ever. After World War II, technological

progress allowed astronomers to build much more sensitive radio telescopes, and radio astronomy started to develop.

Since the intensity of a cosmic source decreases as the inverse squared distance from the source to the radio telescope, the receivers have to be extremely sensitive. Current receivers are much more sensitive than communication systems, and allow sky imaging and accurate cosmic signal processing.

Sky imaging

Sky imaging can be performed with single dish radio telescopes. It consists in scanning a region of the sky in azimuth and elevation, so that integrated data recovered from the observation fill a pixel matrix. The resolution achieved by such an instrument depends on the dish size and on the observed wavelength.

The angular resolution of a single dish radio telescope is given by the Rayleigh criterion:

$$\sin(\theta_{\min}) \approx \theta_{\min} = 1.22\frac{\lambda}{D} \tag{1.1}$$

with:

- $\theta_{\min}$ the minimum angle in radians between two point sources that can be distinguished by the instrument,
- λ the wavelength in meters at which the observation is made,
- D the aperture diameter in meters of the instrument (diameter of the dish).

The factor 1.22 is related to the first zero of the diffraction pattern of the instrument.

This limitation is an issue for low frequency observations. Suppose an observation is made at frequency $f_0 = 100$ MHz with a $D = 100$m single dish radio telescope. The corresponding wavelength at this frequency is:

$$\lambda_0 = \frac{c}{f_0} = \frac{c}{100 \times 10^6} \approx 3\text{m} \tag{1.2}$$

with c the speed of light in vaccum.

The minimum resolution between two point sources is then:

$$\theta_0 = 1.22\frac{\lambda_0}{D} = \frac{3}{100} \approx 2.1^\circ \tag{1.3}$$

The current largest single dish radio telescope is located in Arecibo, Porto Rico (see Figure 1.1.(a)), with a diameter $D = 305$m. This radio telescope allows observations in a 40° cone around the local zenith by moving its receiver. The world's largest fully steerable radio telescope is the Green Bank telescope, located in West Virginia, USA (see Figure 1.1.(b)). Its dish is 100m wide.

The Five hundred meter Aperture Spherical Telescope (FAST) is currently being built in southwest China, and will become the world's largest single dish radio telescope, once operational.

The spatial resolution of an instrument, especially at low frequencies, can be increased with radio telescope arrays.

(a)

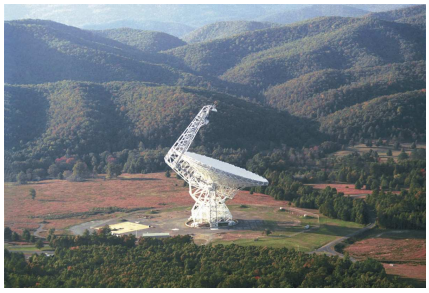

(b)

Figure 1.1: (a) Arecibo radio telescope, located in Porto Rico. 305m single dish radio telescope. (b) Green Bank telescope, located in West Virginia, USA. 100m fully steerable single dish radio telescope.

1.2.2 Radio telescope arrays

Different kinds of radio telescope arrays exist:

- Phased antenna arrays,
- Single dish radio telescope arrays,
- Arrays of phased antenna arrays,
- Phased Array Feeds (PAF), i.e. phased antenna arrays at the location of single dish receivers.

A radio telescope array can either work as a single (big) dish radio telescope, or as an interferometer.

In order to work as a single radio telescope, the signals from each element of the array are digitally combined in such a way that the global radiation pattern steers in one particular direction of interest. This process is called beamforming and is presented in chapter 3. Sky imaging can then also be performed in the same way as with a single dish radio telescope, i.e. by filling a grid with power reached in different directions in the sky.

With enough computational power, such systems can also perform simultaneous multiple observations (multiple beams).

The spatial resolution achieved with a radio telescope array performing aperture synthesis interferometry becomes:

$$\theta_{\min} = 1.22\frac{\lambda}{B} \tag{1.4}$$

with B the maximum distance between two radio telescopes of the array (called baseline).

For instance, a technique called Very Long Baseline Interferometry (VLBI) allows very high resolution observations by combining multiple single dish radio telescopes located on different places around the world. The synthesized aperture of the equivalent radio telescope can thereby reach the size of a continent.

Van Cittert - Zernike Theorem

The Van Cittert-Zernike Theorem [110] is a generalization of the Wiener-Khinchin Theorem, stating that the Fourier transform of the autocorrelation function of a wide-sense stationary random process corresponds to its Power Spectral Density (PSD).

Suppose one cosmic point source emits an electromagnetic field $E(t)$. This field is probed by a sensor located at the spatial position defined by the vector $\mathbf{u}$. If $s(\mathbf{u}, t)$ is the centered signal probed by the sensor, the intensity of the radiation is defined as:

$$I(\mathbf{u}) = \mathbb{E}\{s(\mathbf{u}, t)s^*(\mathbf{u}, t)\} \tag{1.5}$$

$I(\mathbf{u})$ is actually the autocorrelation of $s(\mathbf{u}, t)$

The mutual coherence between two locations defined by the spatial vectors $\mathbf{u}$ and $\mathbf{v}$ is:

$$\Gamma(\mathbf{u}, \mathbf{v}, \tau) = \mathbb{E}\{s(\mathbf{u}, t + \frac{\tau}{2})s^*(\mathbf{v}, t - \frac{\tau}{2})\} \tag{1.6}$$

In other words, the mutual coherence $\Gamma(\mathbf{u}, \mathbf{v}, \tau)$ is the covariance of signals probed at locations $\mathbf{u}$ and $\mathbf{v}$. The Pearson correlation coefficient is defined as:

$$\gamma(\mathbf{u}, \mathbf{v}, \tau) = \frac{\Gamma(\mathbf{u}, \mathbf{v}, \tau)}{I(\mathbf{u})I(\mathbf{v})} \tag{1.7}$$

and is called the degree of coherence.

In the same way as the autocorrelation function $\Gamma(\mathbf{u}, \mathbf{u}, \tau)$ is linked to the Power Spectral Density of $s(\mathbf{u}, t)$, the coherence function $\Gamma(\mathbf{u}, \mathbf{v}, 0)$ is linked to an intensity spatial distribution, e.g. the skymap, following the Van Cittert-Zernike Theorem:

$$\Gamma(\mathbf{u}, \mathbf{v}, 0) = \iint I(l, m)e^{-i2\pi(\mathbf{u}l + \mathbf{v}m)}dldm \tag{1.8}$$

with l and m defining spatial coordinates in the field of view of the instrument. More practical details about Fourier imaging can be found in [12].

An example of an interferometer is the European radio telescope LOFAR, currently the most sensitive instrument at low frequencies.

The LOw Frequency ARray (LOFAR)

LOFAR [2] is a radio interferometer built by the Netherlands Institute for Radio Astronomy (ASTRON) [47]. Its core is located in Exloo, The Netherlands, and is composed of 18 core stations (see Figure 1.2.(a)). 18 remote stations are also spread over The Netherlands, as well as 8 international stations, located in France, the United Kingdom, Sweden and Germany. The United Kingdom - LOFAR international station is shown on Figure 1.2.(b), and the Nançay observatory with the French LOFAR station is shown on Figure 1.2.(c).

Each station is composed of Low Band Antennas (LBA), with a frequency bandwidth $\Delta f = 30 - 80$ MHz, and High Band Antennas, with a frequency bandwidth $\Delta f = 120 - 240$ MHz. The stations perform digital beamforming,

(a)

(b)

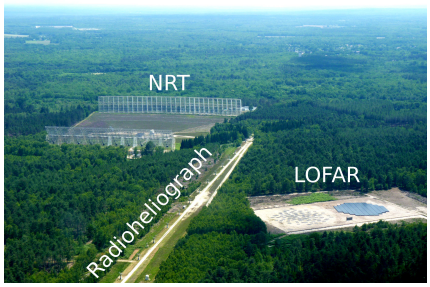

(c)

Figure 1.2: (a) LOFAR core, located in Exloo, The Netherlands. (b) LOFAR international station located in Chilbolton, UK. (c) Nançay observatory, with the French LOFAR station, the radioheliograph and the Nançay Radio Telescope (NRT).

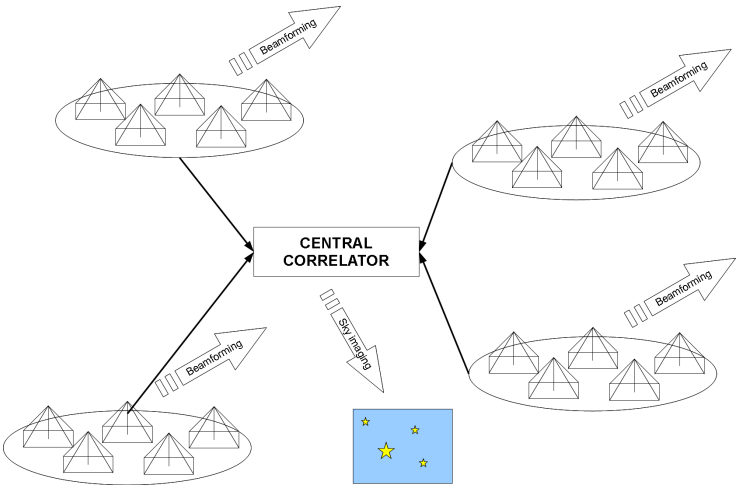

Figure 1.3: LOFAR principle. Each station beamforms in the direction of interest. The signals from all the stations are then sent to the central correlator for further processing.

and the signals from each station are sent via optical fiber to the central correlator consisting of a Blue Gene/P supercomputer for further processing (see Figure 1.3).

LOFAR achieves a frequency resolution of $\delta f = 0.76$ kHz, with baselines going from 100m up to 1500km. The stations can also steer 8 independent directions in the sky (8 simultaneous beams).

Toward the Square Kilometre Array

The Square Kilometre Array (SKA) [3] will become the largest radio telescope in the world. The instrument will be located in the Australian and South African deserts and will have a total collecting area of approximately one square kilometre. Its frequency bandwidth will go from 70 MHz, up to 10 GHz, with a sensitivity around 50 times higher than any other radio telescope. It will be composed of antennas and single dish arrays. The radio telescope should be fully operational in 2021. LOFAR is an SKA pathfinder.

1.3 RFI mitigation for radio astronomy

1.3.1 Radio Frequency Interference

Radio astronomy studies cosmic sources through their radio emissions. Radio frequencies form the lower part of the electromagnetic spectrum, with frequencies going from 3 kHz up to 300 GHz (wavelength from 100km up to 1mm). Because of atmospheric considerations (opacity of the atmosphere and ionosphere at low frequencies), ground-based radio astronomy is usually limited to a smaller frequency range going from 30 MHz up to 100 GHz.

As radio astronomy is considered as an official passive radio spectrum user, some frequency bands of the spectrum are protected and dedicated to radio astronomy. A list of these protected frequencies can be found on the International Telecommunication Union (ITU) website [1]. These frequencies correspond to well-known spectral line emissions.

However, astronomers are increasingly interested in observing outside the protected frequency bands. For instance, the Doppler effect applied to cosmic sources leads to shift in the frequency of spectral lines. The spectral lines considered may then be located outside their dedicated bandwidths. Another example is broad band radiation, such as continuum emissions, which is only in part taken in account in radio astronomy frequencies protection.

Observing outside the protected frequency bandwidths is a major issue in radio astronomy. Since the radio spectrum is extensively occupied by active users, electromagnetic pollution makes it hard to perform observations. Radio communication signals can be around 50 dB above radio telescope system noise, or weaker, while cosmic source signals can be up to 60 dB below the noise level [60, 108].

Radio frequency interference in radio astronomy can be of different kinds. For instance, the LOFAR low frequency band ($30 - 80$ MHz) contains 74 different frequency allocations, as many as the LOFAR high frequency bandwidth ($120 - 240$ MHz) [75]. Typical examples of frequency allocations are Communication / Global Positioning System (GPS) satellite downlinks, land / maritime mobile communications, Global System for Mobile (GSM) communica-

tions, wireless microphones, Digital Audio or Video Broadcasts (DAB/DVB), medical implants, home automation, paging systems, radars, aviation communications, etc.

Figure 1.4 shows examples of RFI acquired with a LOFAR LBA station.

Even when observing strictly in the frequency bandwidths dedicated to radio astronomy, interference can occur. This is due to two main reasons. The first is the non-respect of required communication systems low and high cutoff frequencies, leading to spectral sidelobes emissions. Another reason is receivers non linearities, leading to interference harmonics due to intermodulation products.

Natural phenomena, such as terrestrial lightings, can also interfere with radio telescopes due to their high sensitivities (as mentioned in [108]).

1.3.2 RFI mitigation techniques

Radio telescopes are usually located at sites with low radio frequency occupation. An electromagnetic environmental study is performed before any site decision, in order to evaluate the radio pollution impact regarding the instrument observation frequencies (see [8] for example). Radio quiet zones do exist on the earth but can not be perfectly free of RFI since aerial communications (satellites, aviation) do not restrict their emissions, or because of reflections from ground-based emissions.

RFI mitigation is one of the major issues in radio astronomy, as well as in communications fields. Many studies have been conducted, based on different approaches.

The first step in interference mitigation is to make it possible to distinguish the Signal of Interest (SOI, i.e. cosmic sources in radio astronomy) from other emitted signals (RFI). The criteria, or parameters, used to distinguish the two types of signals are then exploited in order to remove (or attenuate) the contributions of jammers and recover the SOI as well as possible. RFI mitigation techniques are however highly dependent on the type of radio telescope and the type of observation performed.

A polluted radio astronomical subband can easily be processed with well known signal processing techniques as long as the SOI and the RFI do not share the Time and Frequency slots. For short and intermittent interference, the obvious solution is to remove the corrupted time samples before signal integration and further processing on astronomical data. Thresholding the radio telescope output, based on power [10, 84, 20], statistical [73, 37] or cyclostationary [82, 102, 22, 7] parameters, then allows a real-time flagging and/or excision process to be applied. The power strength and duration of the interference can quickly become an issue with this approach.

The temporal approach cannot be applied in continuous interference scenarios. But the diversity between RFI and SOI can also take place in the frequency domain. Analog and digital filtering can then be applied in order to filter out the corrupted frequency bands. Adaptive filtering can either be applied to the radio telescope raw data [53, 99], associated with a reference antenna [11, 23] or based on jammers' properties, such as cyclostationarity [43]. This technique is restricted to narrow band interference, and cannot be applied to broadband interference when it covers large parts of the observed astronomical band.

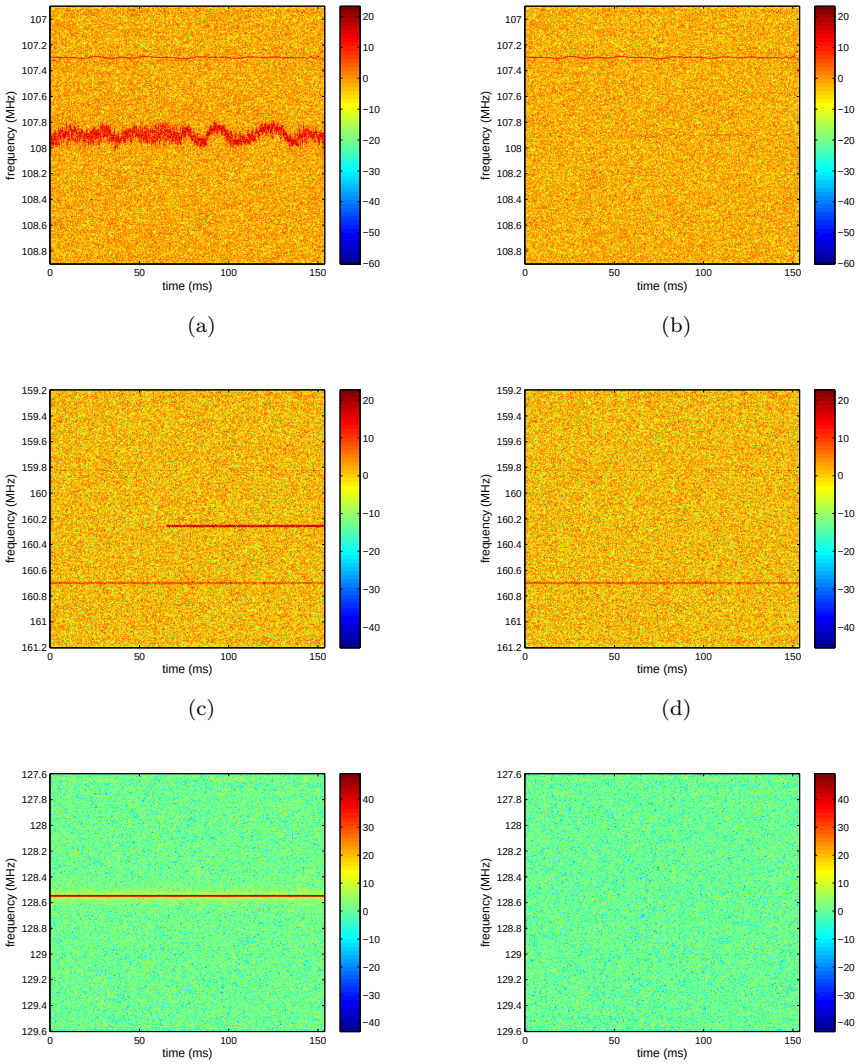

Figure 1.4: RFI and interference mitigation (orthogonal projection) examples with LOFAR HBA data. (a) Strong FM signals. (b) Example of RFI mitigation on the strongest FM signal. (c) Coast communication station signals. (d) Example of RFI mitigation on the intermittent coast communication station signal. (e) Strong aviation signal. (f) Example of RFI mitigation on the aviation signal.

Time and frequency approaches can also be combined [76]. When interference and cosmic sources occupy all observed Time-Frequency slots, these approaches can no longer be applied for RFI mitigation purposes.

The spatial diversity can be exploited with multiple-element radio telescopes. As SOI and RFI have different directions of arrival, they also have different spatial signatures. Different types of processing based on this difference have been proposed. The first kind of processing takes into account a reference antenna (or an antenna sub-array) to track and remove the interference subspace from the observation data [80, 81, 24]. Another approach, called adaptive beamforming, consists in designing an antenna array radiation pattern by taking into account the interference direction of arrival [62, 50, 87, 34]. Other approaches are based on interference subspace cancellation by building spatial filters. The interference subspace is estimated according to statistical or cyclostationary [18, 95, 69, 35] properties.

Finally, another RFI mitigation approach consists in subtracting the interference contributions instead of projecting or filtering them out. This approach assumes however a data model based on the additivity and uncorrelation of the different signals [33, 31, 35].

Further readings about RFI mitigation for radio astronomy can be found in [68, 19, 38]

1.4 Contributions

This thesis focuses on spatial interference mitigation with phased antenna array radio telescopes. In this context, the different signals impinging on a radio telescope (RFI, cosmic sources and system noise) lie in a data vector space, and RFI and SOI are forced into separate subspaces after processing. One popular technique consists in applying an orthogonal projector to the data in order to project out the interference subspace [67]. The problem with the orthogonal projector is that recovering the subspace of interest (cosmic sources) depends on its orthogonality with the interference subspace. To address this problem, an oblique projection is considered. This projection technique no longer depends on the orthogonality between subspaces, and is presented in section 3.3.2.

Another approach for RFI mitigation with multi-element radio telescopes is interference subspace subtraction. After estimating the interference subspace, its contribution is subtracted from the classical covariance matrix. The interference subspace is defined by a basis, made of the different jammers' spatial signatures. But subtracting this subspace from the classical covariance matrix also requires estimating the jammers' powers. A closed form solution of this estimate, once the interference spatial signatures have been estimated, is given in section 3.4.

The accuracy of interference spatial signatures estimation is an important parameter for spatial filtering. Based on (non-)whiteness assumptions, a time-lagged covariance is introduced in section 4.1.3. This covariance matrix allows a more accurate estimation of the interference subspace than the technique based on the classical covariance matrix, especially for weak interference.

Using multiple covariance matrices has also been considered, as can be seen in section 4.2. Three techniques are presented (Mean covariance matrix diagonalization, section 4.2.1, Joint SVD of time-lagged covariance matrices, section

4.2.2 and Joint-diagonalization, section 4.2.3).

Finally, an RFI mitigation algorithm has been implemented on the French station of the radio telescope demonstrator EMBRACE and is presented in section 5.3. This algorithm involves an RFI subspace estimation based on a classical covariance matrix and an oblique projector. Preliminary results are given in this section. Different techniques presented in this thesis have also been tested on LOFAR data, and are presented in section 5.2.

1.5 Publications

- **G.Hellbourg**, R.Weber, A.Millot, C.Capdessus. Transmission des mesures d'un réseau de capteurs environnementaux en bande ISM. Une approche semi-logicielle. *Colloque Sciences et Techniques de l'Information et de la Communication Pour l'Environnement*, ENSM, Saint-Etienne, France, May 11-13 2011, ISBN : 9782911256462
  http://hal.archives-ouvertes.fr/hal-00647529

- **G.Hellbourg**, R.Weber, C.Capdessus, A.J.Boonstra, R.Feliachi. Cyclostationary approaches for spatial RFI mitigation in radio astronomy. *Les radiotélescopes du futur, Technologies et avancées scientifiques*, URSI France, Journées Scientifiques, CNAM, Paris, France, March 29-30 2011
  http://hal.archives-ouvertes.fr/hal-00647574

- **G.Hellbourg**, R.Weber, C.Capdessus, A.J.Boonstra. Cyclostationary approaches for spatial RFI mitigation in radio astronomy. *Comptes Rendus Physique*, 13(1), 71-79, 2012, ISSN : 1631-0705
  http://hal.archives-ouvertes.fr/hal-00668944

- **G.Hellbourg**, R.Weber, C.Capdessus, A.J.Boonstra. Oblique projection beamforming for RFI mitigation in radio astronomy. *IEEE Statistical Signal Processing Workshop (SSP)*, Ann Arbor, MI, USA, August 5-8 2012, ISBN : 978-1-4673-0181-7
  http://ieeexplore.ieee.org/xpls/abs_all.jsp?arnumber=6319860

- **G.Hellbourg**, T.Trainini, R.Weber, E.Moreau, C.Capdessus, A.J.Boonstra. RFI subspace estimation techniques for new generation radio telescopes. *20th IEEE European Signal Processing Conference (EUSIPCO)*, Bucharest, Romania, August 27-31 2012, ISSN : 2219-5491
  http://ieeexplore.ieee.org/xpls/abs_all.jsp?arnumber=6334141

- R.Weber, **G.Hellbourg**, C.Dumez-Viou, A.J.Boonstra, S.Torchinsky, C.Capdessus, K.Abed-Meraim. RFI Mitigation in Radio Astronomy : an Overview *L'électromagnétisme, Une science en pleine action.* URSI France, Journées Scientifiques, CNAM, Paris, France, March 26-27 2013
  http://ursi-france.mines-telecom.fr//index.php?id=67

- **G.Hellbourg**, R.Weber, K.Abed-Meraim, A.J.Boonstra. RFI spatial processing at Nançay observatory : Approaches and experiments. *IEEE International Conference on Acoustics, Speech and Signal Processing (ICASSP)*, Florence, Italy, 2014 (submitted)

1.6 Thesis outline

Chapter 2 states a general data model for phased antenna array radio telescopes. This chapter starts with a single antenna data model, that is then extended to a vectorized data model. The latter leads to the definition of spatial signatures of signals impinging the array. Finally, a classical covariance data model is given. Several assumptions are made concerning either RFI, cosmic sources or the system noise. Some particular statistical properties of these signals are also considered, leading to particular types of covariance matrices.

Chapter 3 starts by presenting four popular beamforming techniques. Three of them are adaptive beamforming techniques. The second part of this chapter deals with projection-based spatial filtering techniques. Two projectors are considered : the orthogonal and the oblique projector. Their performances in terms of RFI attenuation and SOI gain are compared to the performances of the beamforming techniques, regarding different data model parameters, in the conclusion of the section. Finally, an interference subspace subtraction technique is presented in the last part of the chapter. This technique is applied to the classical covariance matrix once the interference subspace has been estimated.

Chapter 4 concerns interference subspace estimation. Different approaches are considered, based on the classical covariance matrix, cyclic or conjugate cyclic covariance matrix and the time-lagged covariance matrix. The second part of the chapter presents multiple covariance matrices approaches, that improve the accuracy of the statistical information recovered with the previous techniques. All these techniques are compared through simulations. In a third section, two popular high resolution interference spatial signature estimation techniques are presented. However, they require a perfect antenna array calibration.

Chapter 5 starts with an overview of the interference mitigation techniques presented in this thesis, applied to corrupted LOFAR Low and High Band Antenna data. The performances of these techniques are qualitatively discussed. In the second part of this chapter, an RFI mitigation algorithm implementation is presented. The RFI mitigation algorithm has been implemented on the French station of the radio telescope demonstrator EMBRACE. Some preliminary results are shown and discussed.

The performances of the techniques presented in this thesis are compared through simulations, either on simulated data or on real data acquired with LOFAR and EMBRACE.

Chapter 2

Data model

In this chapter, we model the data provided by an antenna array radio telescope. The model is additive, and takes into account the cosmic sources, the system noise and the interference contributions. In order to simplify the model, and exploit all the information available, different assumptions concerning the signals are presented. Depending on the type of observation, the type of radio telescope, and its location (close to fixed jammers for instance), these assumptions remain valid or not.

The different data models derived in this chapter will then be used for simulations and the comparison of interference mitigation techniques that are later applied to measured data.

2.1 General data model

Consider an antenna array radio telescope made of M antenna elements. Each antenna receives a signal that can be written as a finite sum of the contributions of all the sources located in the field of view of the antenna array. These sources are of various kinds : cosmic sources, i.e. natural signals emitted by cosmic objects, or man-made sources defined by various parameters (e.g. modulation parameters, power or polarization). Man-made sources will be referred to as Radio Frequency Interference (RFI) in the following.

We will assume that all these sources are point sources. This assumption is mainly due to a compromise between the distance between the source and the instrument and the resolution of the instrument itself. Projected onto a hypothetical sphere centered at an arbitrary antenna of the array, called *celestial sphere*, these sources are spatially described by a set of two spherical coordinates θ and ϕ, respectively named polar and azimuth angles (their radial coordinates being the celestial sphere radius).

Define $x_k(t)$, $k = 1..M$, as the output signal of the k^{th} antenna element at time t. $x_k(t)$ is then expressed in complex baseband form as:

$$
\begin{aligned}
x_k(t) &= \sum_{n=1}^{N_s} a_{s_{n,k}}(t, \theta_{s_n}, \phi_{s_n}) s_n(t - \tau_{n,k}) + n_k(t) \\
&= \sum_{n=1}^{N_c} a_{c_{n,k}}(t, \theta_{c_n}, \phi_{c_n}) c_n(t - \tau_{c_{n,k}}) + \sum_{n=1}^{N_r} a_{r_{n,k}}(t, \theta_{r_n}, \phi_{r_n}) r_n(t - \tau_{r_{n,k}}) + n_k(t)
\end{aligned} \tag{2.1}
$$

with:

- $s_n(t)$, $n = 1 \dots N_s$ the n^{th} signal impinging the antenna array at time t. The number of signals N_s is such that $N_s = N_c + N_r$, with N_s, resp. N_r, the number of cosmic source signals, resp. interference signals, impinging the radio telescope.
- $a_{s_{n,k}}(t, \theta_{s_n}, \phi_{s_n})$ the system gain between the k^{th} antenna and the direction $(\theta_{s_n}, \phi_{s_n})$ on the celestial sphere at time t.
- $c_n(t)$, $n = 1 \dots N_c$ (resp. $r_n(t)$, $n = 1 \dots N_r$) the n^{th} cosmic (resp. RFI) source signal at time t.
- $a_{c_{n,k}}(t, \theta_{c_n}, \phi_{c_n})$ (resp. $a_{r_{n,k}}(t, \theta_{r_n}, \phi_{r_n})$) the system gain related to the k^{th} antenna and the direction $(\theta_{c_n}, \phi_{c_n})$ (resp. $(\theta_{r_n}, \phi_{r_n})$) on the celestial sphere at time t.
- $n_k(t)$ the system noise contribution on the k^{th} antenna.

The time shifts $\tau_{n,k}$, $\tau_{c_{n,k}}$ and $\tau_{r_{n,k}}$ correspond to the signals electromagnetic wave propagation delay between the k^{th} antenna considered and an arbitrary reference antenna of the array.

2.2 Assumptions

2.2.1 Narrowband assumption

The narrow band assumption can be expressed in two domains : the frequency domain and the spatial domain. Suppose the narrowband assumption holds in the frequency domain. Then, by definition, the frequency bandwidth Δf, centered at a frequency f_0, of any signal $s(t)$ impinging the array is much smaller than f_0:

$$\frac{\Delta f}{f_0} \ll 1$$

Being narrowband, the signal $s(t)$ received at the k^{th} antenna ($s_k(t)$) can be defined as a product between a band-limited baseband signal, $b(t)$, and a carrier signal at frequency f_0:

$$s_k(t) = b(t) e^{j 2\pi f_0 t} \tag{2.2}$$

The spatial narrow band assumption concerns the electromagnetic wave propagation of the sources through the antenna array [109]. We define the wave

propagation delay between two antennas k and l of the array as $\tau_{kl} = \tau_l - \tau_k$, where τ_k is the wave propagation delay between the signal source considered and the k^{th} antenna. τ_{kl} depends on the relative orientation and distance from the source to the two antennas. Considering the antennas k and l as the most distant antenna pair of the antenna array, the spatial narrowband assumption is then expressed by:

$$\Delta f \ll (2\pi\tau_{kl})^{-1} \tag{2.3}$$

The signal $s_l(t)$ received at the l^{th} antenna is by nature a time delayed version of $s_k(t)$:

$$\begin{aligned} s_l(t) &= s_k(t - \tau_{kl}) && (2.4)\\ &= b(t - \tau_{kl})e^{j2\pi f_0(t-\tau_{kl})} && (2.5)\\ &= b(t - \tau_{kl})e^{-j2\pi f_0\tau_{kl}}e^{j2\pi f_0 t} && (2.6) \end{aligned}$$

We now apply the inverse Fourier Transform and its translation property to $b(t)$ and $b(t - \tau_{ij})$. If $B(f)$ is the Fourier Transform of $b(t)$, we have:

$$\begin{aligned} b(t) &= \int_{-\frac{1}{2}\Delta f}^{+\frac{1}{2}\Delta f} B(f)e^{j2\pi ft}df && (2.7)\\ b(t - \tau_{ij}) &= \int_{-\frac{1}{2}\Delta f}^{+\frac{1}{2}\Delta f} B(f)e^{-j2\pi f\tau_{ij}}e^{j2\pi ft}df && (2.8) \end{aligned}$$

Using the assumption made in Equation 2.3 on Equation 2.8, we have:

$$b(t) \sim b(t - \tau_{ij}) \tag{2.9}$$

Hence, working at the frequency f_0 at the output of the antenna array radio telescope, the propagation delay of a narrowband source wave between two antennas k and l of the array is expressed as a signal phase shift. Its closed-form expression, according to Equation 2.6, is $e^{-j2\pi f_0\tau_{kl}}$. In other words, the envelope fluctuations of the narrowband signals are neglected. Only the influence of the geometric delay on the carrier is considered. This influence is expressed as signal phase shifts.

The data model expressed in equation 2.1 can now be rewritten as:

$$x_k(t) = \sum_{n=1}^{N_c} a_{c_{n,k}}(t, \theta_{c_n}, \phi_{c_n})c_n(t) + \sum_{n=1}^{N_r} a_{r_{n,k}}(t, \theta_{r_n}, \phi_{r_n})r_n(t) + n_k(t) \tag{2.10}$$

where the signals complex gains $a_{c_{n,k}}(t, \theta_{c_n}, \phi_{c_n})$ and $a_{r_{n,k}}(t, \theta_{r_n}, \phi_{r_n})$ absorb the phase shifts induced by the wave propagation through the antenna array.

In the following, all the signals impinging the antenna array will be considered as narrowband. This condition holds because of the nature of the sources or because of a sub-band filtering pre-processing at the entrance of the system. Henceforth, the signals' frequency dependence will be neglected, and the signals expressed in base band. Radio telescope receivers usually process narrow band signals by applying a frequency downshift onto the received signals.

2.2.2 Near/far field assumption

Any change in a (cosmic or RFI) source location would induce a structure change in its space-time signature. If a source $s(t)$ is moving toward or away from the radio telescope while keeping its angular coordinates (θ_s, ϕ_s) constant, i.e. only its radial coordinate changes, the radius of its spherical or cylindrical (e.g. for long line antennas) wavefront at the radio telescope changes. The far field assumption applies when its spatial signature structure change can be neglected. In other words, the source is considered as being far enough from the radio telescope for its wavefront at the antenna array to be approximated as being flat. If D is the antenna array diameter, λ the emitted signal wavelength and d the distance between the source and the antenna array, then the far field assumption holds if [105]:

$$d > \frac{2D^2}{\lambda} \tag{2.11}$$

This assumption is mostly important for sky imaging and beamforming applications. Section 2.3.3 shows the influence of the far field assumption on spatial signature structures.

2.2.3 Signal model

System noise

The system noise term $n_k(t)$ in Equation 2.1 is itself a sum of the contributions of different noise components, e.g. cosmic background noise, atmospheric noise, receiver noise... Applying the Central Limit Theorem on signals that can already be considered as centered, temporally independent and identically distributed (i.i.d.) with complex Gaussian distribution, this noise term is also centered, i.i.d. with Gaussian distribution.

The noise contributions are temporally stationary over short time intervals. The non-stationary contributions are due to slowly varying physical effects (e.g. night / day cycles...). One aim of the calibration process consists in compensating these non-stationary contributions. However, at a short time scale, the system noise can be considered as stationary. For longer time scales, calibration is necessary to keep this noise stationary.

Cosmic sources

The radio frequency emissions of cosmic sources are due to underlying stochastic processes happening within objects themselves or during their interactions with their near-environment. Therefore, applying again the Central Limit Theorem, cosmic source signals are assumed to be centered, temporally i.i.d. with complex Gaussian distribution [105].

Except for some specific types of sources, such as pulsars for instance, their signals are stationary. However, from an earth local point of view, these signals are no longer stationary. Slowly varying changes in the atmosphere and in the interstellar medium make their statistics vary.

But again, at a short observation scale, cosmic source signals are assumed to be stationary. Their resulting spectra are either wide band (e.g. continuum

emissions), or narrow band peaks corresponding to red-shifted (Doppler) absorption and/or emission spectral lines. Moreover, as was said earlier, all the cosmic sources are assumed to be statistically independent of each other.

Radio frequency interference

Interference is a generic term that depends on the application. Basically, interference is all kinds of signals that corrupt the signal of interest (SOI). Radio frequency interference for radio astronomy can be of various kinds. Impulsive thunderstorm emissions, wind turbine amplitude modulation signals and overhead power line emissions are typical RFI examples. However, most of the interference signals encountered in radio astronomy are due to man-made wireless applications, e.g. Global Positioning System (GPS) satellites, Digital Audio Broadcasting (DAB), amateur radio, paging systems, cell phones, home automation, etc. We will focus in this thesis on man-made modulated signals. We chose three different signal properties to model RFI : centered narrowband Gaussian stationary, Second Order (SO) non-circular and SO cyclostationary (see section 2.4.2).

2.3 Algebraic model

2.3.1 Vectorized data model

The data model defined in Equation 2.1 can also be expressed in the following vector form:

$$\mathbf{x}(t) = \mathbf{A_c} \cdot \mathbf{c}(t) + \mathbf{A_r} \cdot \mathbf{r}(t) + \mathbf{n}(t) \tag{2.12}$$

where:

- $\mathbf{x}(t) = [x_1(t) \cdots x_M(t)]^T$ is the $M \times 1$ phased antenna array output data vector at time t,
- $\mathbf{c}(t) = [c_1(t) \cdots c_{N_c}(t)]^T$ is the $N_c \times 1$ cosmic sources signal vector at time t,
- $\mathbf{A_c} = [\mathbf{a}_{c_1}(t, \theta_{c_1}, \phi_{c_1}) \cdots \mathbf{a}_{c_{N_c}}(t, \theta_{c_{N_c}}, \phi_{c_{N_c}})]$ is the $M \times N_c$ cosmic sources space-time signature vectors matrix, with:
- $\mathbf{a}_{c_n}(t, \theta_{c_n}, \phi_{c_n}) = [a_{c_{n,1}}(t, \theta_{c_n}, \phi_{c_n}) \cdots a_{c_{n,M}}(t, \theta_{c_n}, \phi_{c_n})]^T$ the space-time signature vector corresponding to the n^{th} cosmic source,
- $\mathbf{r}(t) = [r_1(t) \cdots r_{N_r}(t)]^T$ is the $N_r \times 1$ RFI signal vector at time t,
- $\mathbf{A_r} = [\mathbf{a}_{r_1}(t, \theta_{r_1}, \phi_{r_1}) \cdots \mathbf{a}_{r_{N_r}}(t, \theta_{r_{N_r}}, \phi_{r_{N_r}})]$ is the $M \times N_r$ RFI space-time signature vectors matrix, with:
- $\mathbf{a}_{r_n}(t, \theta_{r_n}, \phi_{r_n}) = [a_{r_{n,1}}(t, \theta_{r_n}, \phi_{r_n}) \cdots a_{r_{n,M}}(t, \theta_{r_n}, \phi_{r_n})]^T$ the space-time signature vector corresponding to the n^{th} RFI,
- $\mathbf{n}(t) = [n_1(t) \cdots n_M(t)]^T$ is the $M \times 1$ system noise vector at time t.

2.3.2 Covariance matrix data model

The astronomical information coming from cosmic sources is provided by their signal's second order statistics [105]. Antenna array radio telescopes either provide them as a beamformed power over time, or as an integrated array covariance matrix. The covariance matrix of the vectorized data model defined in Equation 2.12 is expressed by:

$$\mathbf{R}(t,\tau) = \mathbb{E}\{\mathbf{x}(t+\frac{\tau}{2}) \cdot \mathbf{x}^H(t-\frac{\tau}{2})\} \tag{2.13}$$

Assuming independence between RFI, cosmic sources and system noise, i.e.

$$\begin{aligned}
\mathbb{E}\{c_n(t+\frac{\tau}{2}){r_m}^*(t-\frac{\tau}{2})\} &= 0, \quad \forall\ \tau, n \in [1 \dots N_c], m \in [1 \dots N_r] \\
\mathbb{E}\{c_n(t+\frac{\tau}{2}){n_m}^*(t-\frac{\tau}{2})\} &= 0, \quad \forall\ \tau, n \in [1 \dots N_c], m \in [1 \dots M] \\
\mathbb{E}\{r_n(t+\frac{\tau}{2}){n_m}^*(t-\frac{\tau}{2})\} &= 0, \quad \forall\ \tau, n \in [1 \dots N_r], m \in [1 \dots M]
\end{aligned}$$

the covariance matrix $\mathbf{R}(t,\tau)$ can be written as:

$$\mathbf{R}(t,\tau) = \mathbf{A_c} \cdot \mathbf{R_c}(t,\tau) \cdot {\mathbf{A_c}}^H + \mathbf{A_r} \cdot \mathbf{R_r}(t,\tau) \cdot {\mathbf{A_r}}^H + \mathbf{R_n}(t,\tau) \tag{2.14}$$

with:

- $\mathbf{R_c}(t,\tau) = \mathbb{E}\{\mathbf{c}(t+\frac{\tau}{2})\mathbf{c}^H(t-\frac{\tau}{2})\}$
- $\mathbf{R_r}(t,\tau) = \mathbb{E}\{\mathbf{r}(t+\frac{\tau}{2})\mathbf{r}^H(t-\frac{\tau}{2})\}$
- $\mathbf{R_n}(t,\tau) = \mathbb{E}\{\mathbf{n}(t+\frac{\tau}{2})\mathbf{n}^H(t-\frac{\tau}{2})\}$

Multipath effects and noise coupling aspects have been investigated respectively in appendices A and B.

2.3.3 Calibration and spatial signature vector structure

Far field sources

Cosmic sources are usually considered as being far field [63]. As long as the antenna array is perfectly calibrated, their spatial signature vectors are predictable as soon as their location and trajectory are known. The structure of these vectors is based on a dot product between the source direction, given by its angular coordinates, and the antenna array baseline coordinates [90].

Let (θ_s, ϕ_s) be the spherical coordinates of the source s at time t and frequency f_0 impinging an M-antenna array radio telescope. The spatial signature vector of s, $\mathbf{a_s}(\theta_s, \phi_s)$, also known as *steering vector*, is then expressed as:

$$\mathbf{a_s}(\theta_s, \phi_s) = e^{j2\pi \frac{f_0}{c} \mathbf{C}_{array}^T \mathbf{d}_{\theta_s, \phi_s}} \tag{2.15}$$

with:

- c the speed of light in vacuum,

- $\mathbf{C}_{array}$ a $3 \times M$ matrix containing in its columns the cartesian coordinates of each antenna of the array. These coordinates are either given relative to a reference antenna or to an arbitrary point in space,

- $\mathbf{d}_{\theta_s,\phi_s}$ a 3×1 cartesian vector pointing the direction (θ_s, ϕ_s) on the celestial sphere.

Without calibration, complex gains on each antenna of a phased antenna array radio telescope might not be equal. The spatial signature vector is then modeled as follows:

$$\mathbf{a_s}(\theta_s, \phi_s) = \mathbf{a} \cdot e^{j2\pi\mathbf{r}} \tag{2.16}$$

with $\mathbf{a}$ and $\mathbf{r}$ two $M \times 1$ arbitrary (but fixed) uniformly distributed random vectors. In the following, we will consider $\mathbf{a} = \mathbf{1}_{M\times 1}$, neglecting any amplification difference between antenna elements.

A calibration step is therefore required before any observation for the radio telescope to provide exploitable astronomical data [104].

There are two kinds of uncalibration. The first one, concerning the antenna's directivity and the ionospheric and atmospheric disturbances, is direction dependent. The second one concerns the receiver's signal processing path, and is direction independent.

Considering the antenna array uncalibrated, its covariance matrix is expressed as:

$$\mathbf{R}(t,\tau) = \mathbf{G}(\mathbf{A_c} \cdot \mathbf{R_c}(t,\tau) \cdot \mathbf{A_c}^H + \mathbf{A_r} \cdot \mathbf{R_r}(t,\tau) \cdot \mathbf{A_r}^H)\mathbf{G}^H + \mathbf{R_n}(t,\tau) \tag{2.17}$$

where $\mathbf{G}$ is a $M \times M$ diagonal matrix defined by $\mathbf{G} = diag(g_1, \ldots, g_M)$, with g_k, the relative complex gain associated with the k^{th} antenna of the array.

With a perfectly calibrated antenna array, the gain matrix $\mathbf{G}$ is such that:

$$\mathbf{G} = \mathbf{I}_{\mathrm{M\times M}} \tag{2.18}$$

In the following, the assumption 2.18 will be considered as true. The antenna array spatial distribution will not be taken into account, i.e. the sources spatial signature will be considered as arbitrary, but fixed, random complex-valued vectors, and complex antenna gains are distributed into them. The spatial signature vector structures considered will therefore follow the equation 2.16.

Near field sources

A near-field signal impinging the array does not meet the condition expressed in Equation 2.11. In this case, its wavefront cannot be considered as being flat when reaching the antenna array. The relative phase difference distribution can however still be predicted by knowing the exact source location relative to the array location and structure by applying basic solid geometry. However, without loss of generality, the source's spatial signature will also be considered as being arbitrary, but fixed, random complex valued vectors.

2.4 RFI properties

2.4.1 Non-circularity

The non-circularity property of a signal is based on the random complex variable theory [79]. This circularity property says that the statistics of the two random complex variables z and $ze^{j\theta}$ are the same for any rotation over an angle $\theta \in [0 \dots 2\pi]$. For example, let us consider the SO statistics of a complex variable. These statistics are defined by both the covariance function (Equation 2.19) and the conjugate covariance function (Equation 2.20) expressed by:

$$\Gamma_z(t,\tau) = \mathbb{E}\{z(t+\frac{\tau}{2})z^*(t-\frac{\tau}{2})\} \tag{2.19}$$

$$\tilde{\Gamma}_z(t,\tau) = \mathbb{E}\{z(t+\frac{\tau}{2})z(t-\frac{\tau}{2})\} \tag{2.20}$$

The variable z is said SO circular if both the covariance and conjugate covariance functions of z and $ze^{j\theta}$ are equal for any $\theta \in [0 \dots 2\pi]$. The covariance functions of z and $ze^{j\theta}$ are equal for any θ. Concerning the conjugate covariance function, we have:

$$\tilde{\Gamma}_{ze^{j\theta}}(t,\tau) = \mathbb{E}\{(z(t+\frac{\tau}{2})e^{j\theta})(z(t-\frac{\tau}{2})e^{j\theta})\} \tag{2.21}$$

$$= \mathbb{E}\{z(t+\frac{\tau}{2})z(t-\frac{\tau}{2})e^{j2\theta}\} \tag{2.22}$$

$$= \tilde{\Gamma}_z(t,\tau)e^{j2\theta} \tag{2.23}$$

Therefore, the only condition for z to be circular is $\tilde{\Gamma}_z(t,\tau) = 0$. A non-circular complex variable is then a variable z such that $\tilde{\Gamma}_z(t,\tau) \neq 0$. In a multidimensional way, an SO non-circular complex vector $\mathbf{z}$ is a vector such that:

$$\tilde{\mathbf{R}}_{\mathbf{z}}(t,\tau) = \mathbb{E}\{\mathbf{z}(t+\frac{\tau}{2})\mathbf{z}^T(t-\frac{\tau}{2})\} \neq \mathbf{0}, \quad \forall\{t,\tau\} \in \mathbb{R}^2 \tag{2.24}$$

$\tilde{\mathbf{R}}_{\mathbf{z}}(t,\tau)$ is called the *conjugated covariance matrix*. Contrary to cosmic sources and system noise, some modulated RFI such as Amplitude Modulated or Binary Phase Shift Keying modulated signals, present the non-circularity property.

2.4.2 Second order cyclostationarity

Consider an SO stationary complex process $z(t)$. By definition, its autocovariance function is time independent:

$$\Gamma_z(t,\tau) = \Gamma_z(\tau) \tag{2.25}$$

Some non stationary processes exhibit a periodicity in their covariance function:

$$\Gamma_z(t+T_0,\tau) = \Gamma_z(t,\tau), \quad T_0 \in \mathbb{R}^* \tag{2.26}$$

These kinds of processes are said to be *wide sense SO cylostationary* [42, 44, 86]. Being periodic with a period T_0, also called the *cyclic period*, their covariance function admits the following Fourier decomposition:

$$\Gamma_z(t,\tau) = \sum_{n=-\infty}^{+\infty} \gamma_{\alpha_n}(\tau) e^{j2\pi \frac{n}{T_0} t}, \quad n \in \mathbb{N} \tag{2.27}$$

with

$$\gamma_{\alpha_n}(\tau) = \frac{1}{T_0} \int_{-\frac{T_0}{2}}^{+\frac{T_0}{2}} \Gamma_z(t,\tau) e^{-j2\pi \frac{n}{T_0} t} dt \tag{2.28}$$

$$= \left\langle z(t+\frac{\tau}{2}) z^*(t-\frac{\tau}{2}) e^{-j2\pi \frac{n}{T_0} t} \right\rangle_\infty \tag{2.29}$$

$\gamma_{\alpha_n}(\tau)$ is called the *cyclic covariance function* of z at cyclic frequency $\alpha_n = \frac{n}{T_0}$. Since z is a complex process, it also admits a *conjugate cyclic covariance function* defined by:

$$\tilde{\gamma}_{\alpha_n}(\tau) = \frac{1}{T_0} \int_{-\frac{T_0}{2}}^{+\frac{T_0}{2}} \tilde{\Gamma}_z(t,\tau) e^{-j2\pi \frac{n}{T_0} t} dt \tag{2.30}$$

$$= \left\langle z(t+\frac{\tau}{2}) z(t-\frac{\tau}{2}) e^{-j2\pi \frac{n}{T_0} t} \right\rangle_\infty \tag{2.31}$$

with $\tilde{\Gamma}_z(t,\tau)$ as expressed in Equation 2.20. Henceforth, SO cyclostationary processes with a cyclic frequency α will be denoted *α-cyclostationary processes*. When the only cyclic frequency of a process is $\alpha = 0$, this process is stationary.

Cyclic and conjugated cyclic covariance functions can easily be generalized to multidimensional SO α-cyclostationary processes. If $\mathbf{z}(t)$ is a random complex vector with SO α-cyclostationary entries, its *cyclic correlation matrix* is defined by:

$$\mathbf{R}_{\mathbf{z}}^{\alpha}(\tau) = \mathbb{E}\{\mathbf{z}(t+\frac{\tau}{2}) \left(\mathbf{z}^H(t-\frac{\tau}{2}) \odot (e^{-j2\pi\alpha t}.\mathbf{1}^T) \right)\} \tag{2.32}$$

In the same way, the *conjugate cyclic correlation matrix* of $\mathbf{z}(t)$ is defined by:

$$\tilde{\mathbf{R}}_{\mathbf{z}}^{\alpha}(\tau) = \mathbb{E}\{\mathbf{z}(t+\frac{\tau}{2}) \left(\mathbf{z}^T(t-\frac{\tau}{2}) \odot (e^{-j2\pi\alpha t}.\mathbf{1}^T) \right)\} \tag{2.33}$$

Consider now the data model described in Equation 2.12, but with only one single α-cyclostationary interference $r_{cyc}(t)$ (with $\alpha \neq 0$). The model becomes:

$$\mathbf{x}(t) = \mathbf{a}_{r_{cyc}} r_{cyc}(t) + \mathbf{A}_{\mathbf{c}} \cdot \mathbf{c}(t) + \mathbf{n}(t) \tag{2.34}$$

(In order to simplify the equations, we have omitted the three parameters (t, θ, ϕ) of the interference spatial signature)

Using the linearity of the average operator, the cyclic correlation matrix of $\mathbf{x}(t)$ can be written as:

$$\mathbf{R}_{\mathbf{x}}^{\alpha}(\tau) = \mathbf{R}_{r_{cyc}}^{\alpha}(\tau) + \mathbf{R}_{\mathbf{c}}^{\alpha}(\tau) + \mathbf{R}_{\mathbf{n}}^{\alpha}(\tau) \tag{2.35}$$

	AM	BPSK	M-PSK	M-QAM
Cyclic frequencies (α)	none	$\frac{n}{T_{sym}}$	$\frac{n}{T_{sym}}$	$\frac{n}{T_{sym}}$
Conjugated cyclic frequencies ($\tilde{\alpha}$)	$2f_0$	$2f_0 + \frac{n}{T_{sym}}$	none	none

Table 2.1: Cyclic and conjugated cyclic frequencies for AM, BPSK, M-PSK and M-QAM modulated signals. f_0 corresponds to the modulated signal carrier frequency, and T_{sym} to its symbol duration period. n is an integer.

Cosmic sources and the system noise are assumed to be stationary signals [105], and therefore do not admit any cyclic power for $\alpha \neq 0$. We have:

$$\mathbf{R}_{\mathbf{x}}^{\alpha}(\tau) = \mathbf{R}_{r_{cyc}}^{\alpha}(\tau) = \gamma_{\alpha_{r_{cyc}}}(\tau).\mathbf{a}_{r_{cyc}}\mathbf{a}_{r_{cyc}}^{H} \tag{2.36}$$

with $\gamma_{\alpha_{r_{cyc}}}$ the cyclic covariance function of $r_{cyc}(t)$.

Some SO cyclostationary modulated signals also present conjugated cyclic frequencies. In the same way, the stationary contributions of the data model will no longer contribute to the conjugated cyclic covariance matrix:

$$\tilde{\mathbf{R}}_{\mathbf{x}}^{\alpha}(\tau) = \left\langle \mathbf{x}(t+\frac{\tau}{2}) \left(\mathbf{x}^{T}(t-\frac{\tau}{2}) \odot (e^{-j2\pi\alpha t}.\mathbf{1}^{T}) \right) \right\rangle_{\infty} \tag{2.37}$$

$$= \tilde{\gamma}_{\alpha_{r_{cyc}}}(\tau).\mathbf{a}_{r_{cyc}}\mathbf{a}_{r_{cyc}}^{H} \tag{2.38}$$

When the conjugate cyclic frequency $\alpha = 0$, the conjugate covariance matrix expressed in equation 2.37 corresponds to the conjugate covariance matrix expressed in equation 2.24. A non-circular signal can therefore also be seen as a cyclostationary signal with, at least, one conjugate cyclic frequency : $\alpha = 0$.

The Table 2.1 shows the cyclic and conjugated cyclic frequencies corresponding to Amplitude Modulated (AM), Binary Phase Shift Keying (BPSK), M-Phase Shift Keying (M-PSK) and M-Quadrature Amplitude Modulation (M-QAM) signals [40, 41].

Figure 2.1 shows the Power spectral Density, the cyclic power spectrum and the conjugated cyclic power spectrum of a simulated Binary Phase Shift Keying modulated signal. The peaks that can be seen on spectra 2.1.(b) and 2.1.(c) correspond to the modulation's cyclic and conjugated cyclic frequencies.

2.5 Conclusions on the data model

Understanding the data is an important step for any signal processing. Concerning interference mitigation for phased antenna array radio telescopes, three kind of signals are recovered at the system output:

- The cosmic sources, or signals of interest. These signals usually have low power and can most of the time be modeled as white stationary processes with Normal distribution over a short time scale. Pulsing sources also exist, and the approach will then be completely different (see [6] for more details).
- The system noise. System noise is always present in the data. The system is here understood in the broad sense, i.e. taking into account cosmic noise,

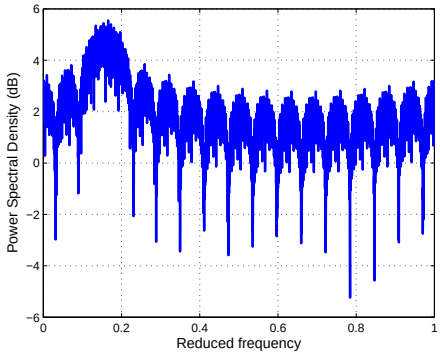

(a)

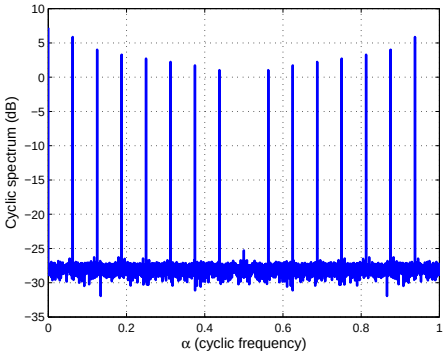

(b)

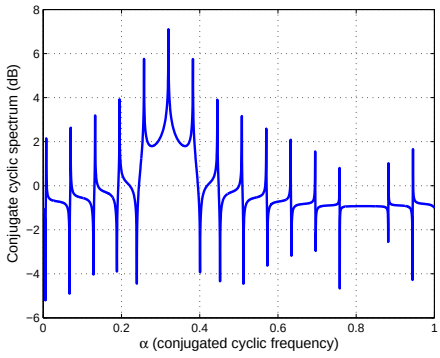

(c)

Figure 2.1: Cyclostationary properties of the BPSK modulation. (a) Power Spectral Density of a simulated BPSK modulated signal (reduced carrier frequency $f_0 = 0.16$ (reduced frequency) and symbol duration period $T_{sym} = 16$ samples). (b) Cyclic power spectrum. (c) Conjugate cyclic power spectrum.

the electronic noise, thermal noise, analog to digital conversion noise, etc. Applying the Central Limit Theorem, this noise is commonly modeled as a white stationary Gaussian process. Unlike cosmic sources, the system noise is also considered as spatially white.

- Radio Frequency Interference. RFI are signals impinging the antenna array without being of interest. Different sources can emit interfering signals, especially telecommunication devices. These signals have high power, and their modeling depends on their nature : natural (cosmic or due to natural phenomena) or man-made signals.

The full data model is an additive model. The phased antenna array output therefore contains contributions from cosmic sources, system noise, and, depending on the frequency bandwidth of interest, in certain cases the observation time, radio frequency interference.

Figure 2.2 shows a data Power Spectral Density and Time-Frequency representation of an acquisition made with a LOFAR High Band Antenna over 150ms and 100 MHz frequency bandwidth. Interference is not present over the whole bandwidth, but its power is far stronger than that of cosmic sources, which are not visible at all on this figure (requiring a longer integration time). The strong interference located around 170 MHz corresponds to a pager system emitting in the Netherlands. As an example, Figure 2.3 shows the cyclic and conjugated cyclic power spectra of this interference. Different cyclic frequencies define the modulation scheme of the interference, and can be used in order to estimate this interference spatial signature and mitigate it, as will be seen in the following chapters.

Modifying the radio telescope correlator input data, the antenna array covariance model can be generalized in order to take into account the different RFI properties seen in this chapter:

$$\mathbf{R}(t,\tau,\alpha) = \mathbb{E}\{\mathbf{y}_\alpha(t-\frac{\tau}{2})\mathbf{y}_{-\alpha}(t+\frac{\tau}{2})^H\} \tag{2.39}$$

where $\mathbf{y}_\alpha(t) = \mathbf{x}(t)e^{-j\pi\alpha t}$.

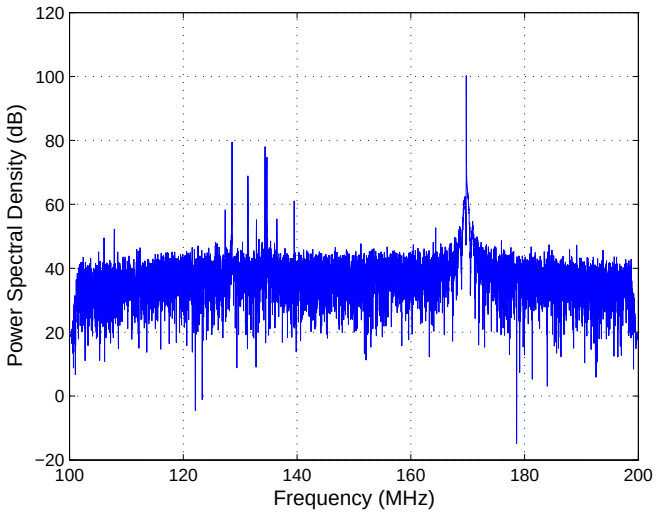

(a)

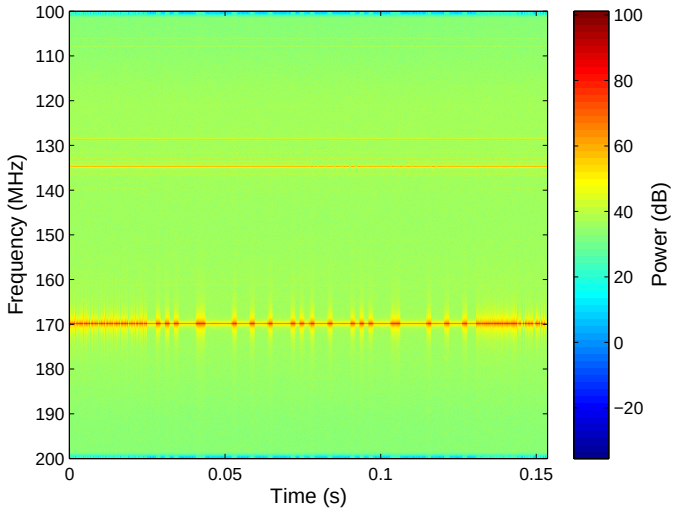

(b)

Figure 2.2: 150ms data acquired with a single LOFAR High Band Antenna in the Netherlands. A strong pager signal can be seen at 170 MHz. (a) Power Spectral Density of an acquisition made with a single LOFAR antenna over 100 MHz frequency bandwidth. (b) Time-Frequency representation of the acquisition.

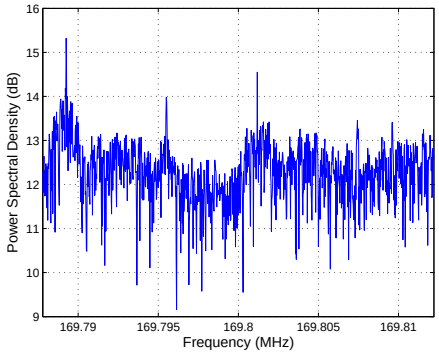

(a)

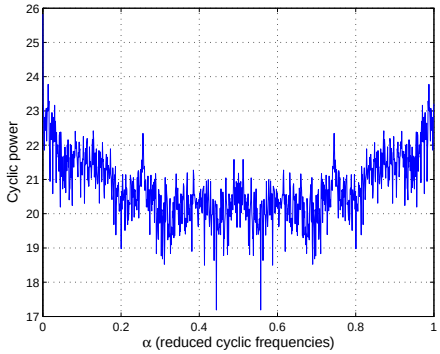

(b)

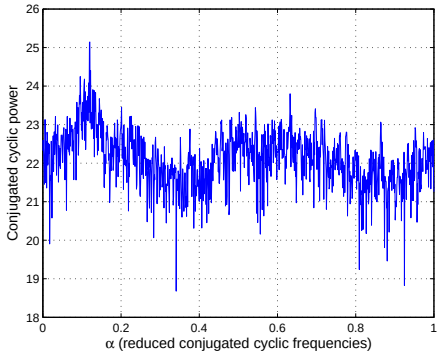

(c)

Figure 2.3: Cyclostationary properties of a pager system signal acquired with a LOFAR High Band Antenna. (a) Power Spectral Density. (b) Cyclic spectrum. (c) Conjugated cyclic spectrum. The spectral lines seen on (b) and (c) correspond to the pager cyclic frequencies.

Chapter 3

Spatial filtering

3.1 Introduction

The major advantage of phased antenna arrays is their ability to steer a direction-of-interest electronically by coherently summing the signals coming from each antenna. This operation is called 'beamforming'. However, the corresponding radiation pattern presents sidelobes (see figure 3.1 for instance). Even if the sidelobe gains are small compared to the main lobe gain, a strong interference impinging the array through these lobes will corrupt the data.

RFI entering via side lobes are not the only way in which data for a phased antenna radio telescope can be corrupted. Depending on its main lobe width, flying transmitters such as in satellites or airplanes can also impinge the array through the main lobe steering a source of interest. A third source of radio telescope data corruption is intermodulation products, i.e. strong interference polluting other frequency bands than the one of interest might also corrupt the observation when the array receiver presents non-linearities.

RFI mitigation for radio astronomy is not only a matter of cancelling the interfering signals. More importantly for astronomers, the cosmic signal of interest has to remain as far as possible intact.

Currently, the RFI mitigation strategy used for most antenna array radio telescopes is called 'flagging'. The idea behind this technique is to monitor the spectrum during an observation and simply excise the corrupted frequency subbands at corrupted time-slots. This process can be done automatically in real time, as well as manually with offline post processing tools. For instance, the European radio telescope LOFAR provides a post-correlation RFI classification tool based on combinatorial thresholding [77].

Flagging techniques do not exploit all the information provided by the system : spatial information, in particular, is not taken into account. Spatial filtering techniques have been developed for several decades to avoid interference impinging telecommunication and radar antenna array systems [64]. Spatial filtering is also extensively used in the field of microphone array systems [15].

In radio astronomy, antenna arrays are used either for beamforming applications, i.e. used as a sensitive and electronically steerable single antenna radio telescope, or for radio interferometry applications, i.e. correlating the antenna array output in order to create wide-field-of-view radio images. Depending on

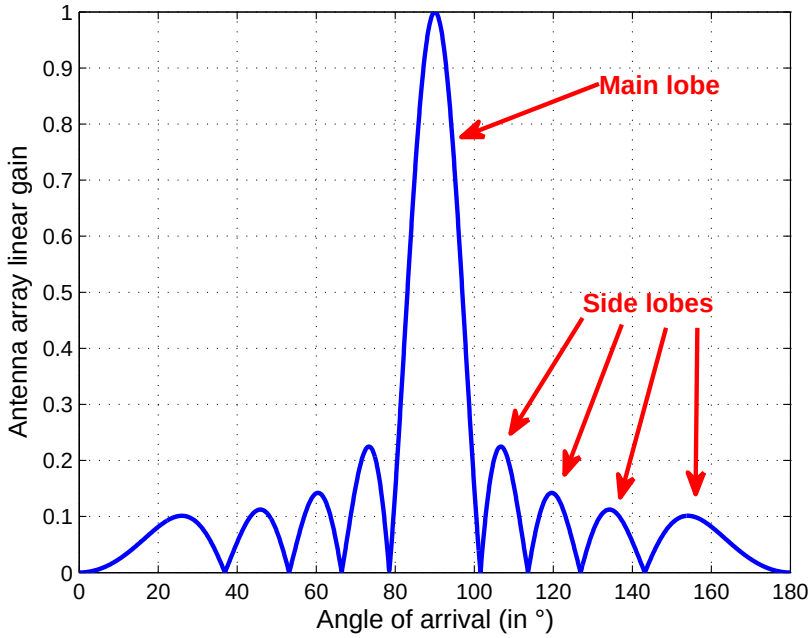

Figure 3.1: Directivity diagram of a 10-antenna Uniform Linear Array (ULA), with $\frac{\lambda}{2}$ spacing, beamforming in the direction 90°. The main lobe is centered at 90° with unitary maximum gain.

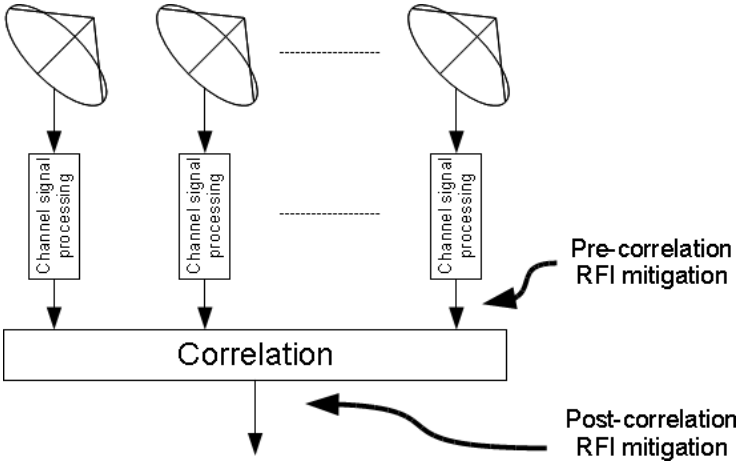

Figure 3.2: Antenna array radio telescope system. Signals acquired by antennas are pre-processed (subband filtering and frequency shifting), then correlated. Spatial RFI filtering can be applied either before or after the correlation process.

the use of the radio telescopes, spatial filtering techniques are preferably used before the correlation process, for example during the tracking of a cosmic source of interest, or after correlation, for example before imaging the radio sky. Figure 3.2 shows where these processes can take place in an antenna array system.

The spatial filtering technique (or techniques) chosen depend on different parameters, such as the type of observation, the expected performances, and also the available computational power.

The aim of this chapter is to present and compare spatial filtering techniques that can be used for radio astronomy. We will consider the following narrow band data model based on the one given in Equation 2.12:

$$\mathbf{x}(t) = \mathbf{a}_c c(t) + \mathbf{A}_\mathbf{r} \cdot \mathbf{r}(t) + \mathbf{n}(t) \tag{3.1}$$

The signal $c(t)$ is here the cosmic signal-of-interest. The signal spatial signatures are here considered as being known. The following chapter presents techniques allowing their estimation. We omit here the source spatial signature vectors time-dependence (t) and spatial-dependence (ϕ, θ) for the sake of notation simplicity.

The different techniques presented in this chapter can be applied either before or after the correlation process. However, the post-correlation approach is generally preferred since in most observational systems an observation covariance matrix is produced by default.

3.2 Beamforming

The idea of beamforming is to form a linear combination of the outputs of each antenna of the array [97, 98]. Weights applied to the antenna array output are chosen according to the direction of the source-of-interest $(c(t))$, but also the desired attenuations in the directions of corrupting sources $(\mathbf{r}(t))$ [52]. We present in this section four popular beamforming techniques. The first of them,

the *delay and sum beamformer*, only takes the source-of-interest direction into account. It is a so-called data-independent beamformer since no information about its environment is injected in its calculation.

3.2.1 Classical delay and sum beamforming

Knowing the source-of-interest location, defined by $\mathbf{a}_c$, the basic idea of the *delay and sum beamformer* is to build the Moore-Penrose inverse of this vector, and apply it to the antenna array output vector:

$$\tilde{c}(t) = (\mathbf{a}_c^H \mathbf{a}_c)^{-1} \mathbf{a}_c^H \mathbf{x}(t) \tag{3.2}$$

where $\tilde{c}(t)$ is the estimate of the source-of-interest signal. This kind of beamformer is the optimal solution in the least-squares sense in a single source environment. Applied to the data model defined in Equation 3.1, we have:

$$\tilde{c}(t) = \frac{1}{\|\mathbf{a}_c\|^2} \left(\|\mathbf{a}_c\|^2 c(t) + \sum_{n=1}^{N_r} \mathbf{a}_c^H \mathbf{a}_{r_n} r_n(t) + \mathbf{a}_c^H \mathbf{n}(t) \right) \tag{3.3}$$

with $\mathbf{a}_c^H \mathbf{a}_c = \|\mathbf{a}_c\|^2$. The resulting noise contribution is a linear combination of each antenna's noise term. The attenuation factor for the interference signals $r_n(t)$ can be seen as dot products between the signal-of-interest steering vector and the interference steering vector:

$$\mathbf{a}_c^H \mathbf{a}_{r_n} = \|\mathbf{a}_c\| . \|\mathbf{a}_{r_n}\| . \cos(\theta_{\mathbf{a}_c, \mathbf{a}_{r_n}}) \tag{3.4}$$

where $\theta_{\mathbf{a}_c, \mathbf{a}_{r_n}}$ is the angle between the two vectors $\mathbf{a}_c$ and $\mathbf{a}_{r_n}$ in the M-dimensional antenna array data vector space. Depending on the value of this angle, the attenuation factor varies between $-\|\mathbf{a}_c\| . \|\mathbf{a}_{r_n}\|$ and $+\|\mathbf{a}_c\| . \|\mathbf{a}_{r_n}\|$. In the event of non-orthogonality between these pairs of vectors ($\mathbf{a}_c$ and $\mathbf{a}_{r_n}$ with $n = 1..N_r$), a remaining interference signal contribution cannot be avoided after processing.

As an example, figure 3.3 shows the directivity pattern obtained with a delay and sum beamformer while steering at the direction highlighted by the green line on the figure. The beamformer has here been applied to a uniform linear array made of 10 antennas with a spacing corresponding to half the observed wavelength. The nulls in the pattern (maximum rejection) are located at angles where the respective steering vector is orthogonal with the beamforming vector. The maximum gain is obtained in the direction of interest.

This beamformer is the easiest to implement, since it does not require any further calculation to implement it. Its performances can however be improved by using an apodization window [51]. In the same way as when designing a Finite Impulse Reponse digital filter, applying an apodization window to the beamformer coefficients (that are usually of equal magnitude) helps control the main lobe width and the side lobes gain and thus obtain the desired spatial response. Figure 3.4 shows the modified directivity pattern after applying a Gaussian window (figure 3.4.(a)) to the previous beamformer (figure 3.3). The side lobe gains are lower after apodization, but the main lobe width is larger, potentially allowing more interference to impinge the array through this lobe.

The delay and sum beamformer is not suitable for multiple radio sources environments since there is no option for attenuating any particular direction

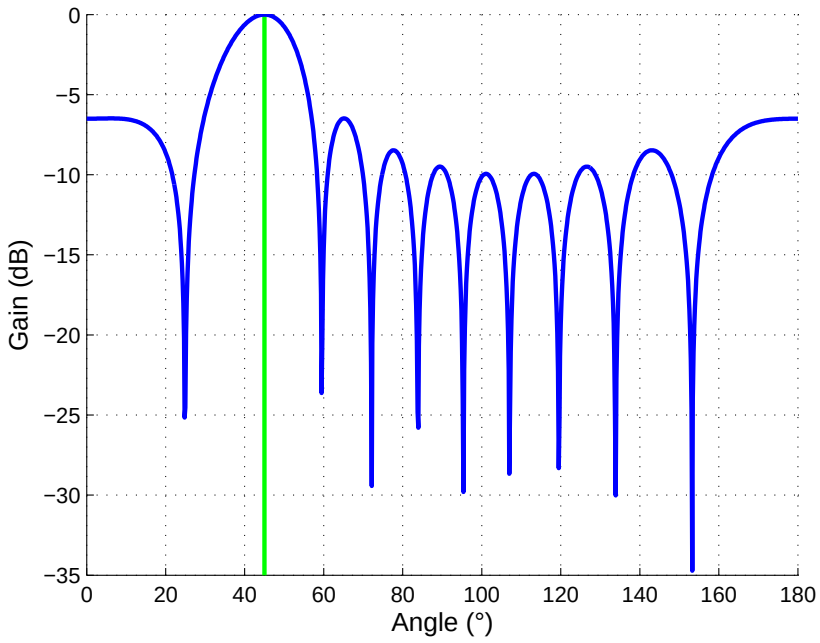

Figure 3.3: Directivity diagram obtained with a classical delay and sum beamformer. Computed using a simulated uniform linear antenna array made of 10 antennas with $\frac{\lambda}{2}$ spacing. The green line corresponds to the signal of interest direction.

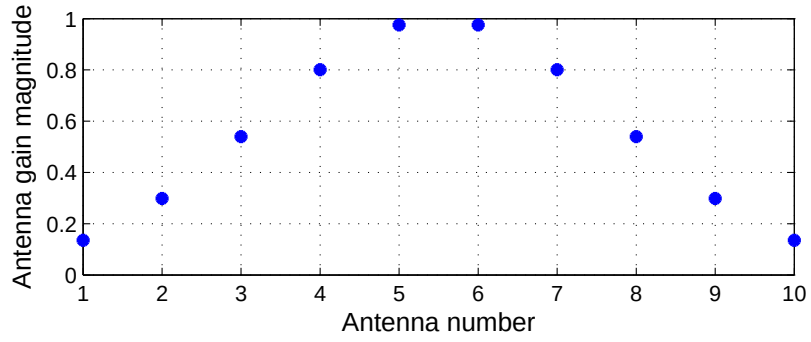

(a)

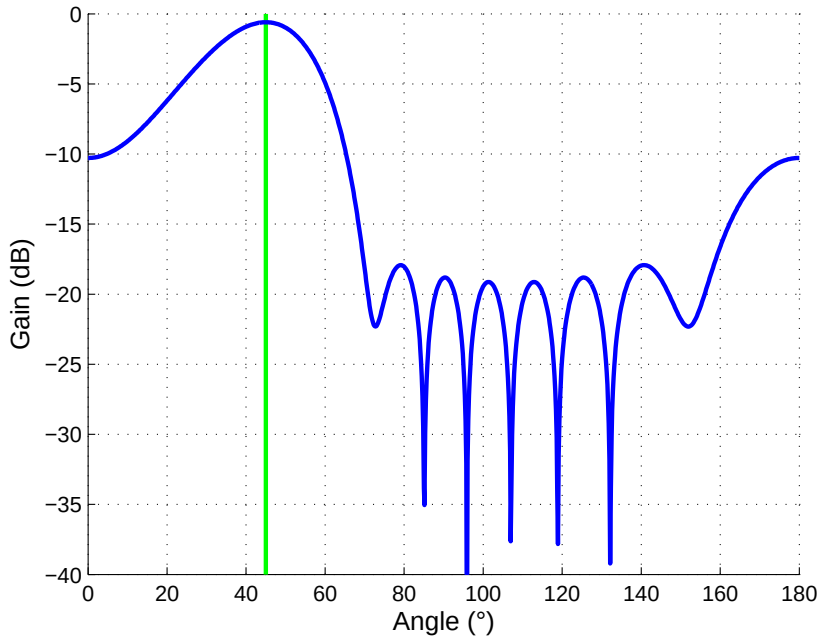

(b)

Figure 3.4: Directivity diagram obtained with a classical delay and sum beamformer after apodization. (a) Gaussian apodization window applies to the delay and sum beamforming vector coefficients. (b) Directivity pattern computed using a simulated calibrated uniform linear antenna array made of 10 antennas with $\frac{\lambda}{2}$ spacing. The green line corresponds to the signal of interest direction.

in the field of view of the antenna array. Even with apodizing the beamformer coefficients, the interference might still be strong enough to saturate the radio telescope receiver and/or corrupt the data, although data can still be corrupted without receiver saturation. However, in a non-corrupted environment, the delay and sum beamformer presents the advantage of being easy to implement and to update (while tracking a source of interest) and computationally cheap. These advantages are even more important when the antenna array contains a large number of antennas. This approach is the one implemented on current antenna array radio telescopes, either on antenna array stations or at the central correlation stage.

3.2.2 Multiple Sidelobe Canceller

The *Multiple Sidelobe Canceller (MSC)* [74, 48] uses two sub-arrays of the antenna array radio telescope. The first one, called *primary array*, beamforms in the direction of the source-of-interest. The beamforming technique used can for example be a classical *delay and sum beamformer*, but can also be a single antenna. The idea is to optimize a beamforming weight vector for the second sub-array, called *auxiliary array*, in order to minimize the mean squared error between the output of these two sub-arrays in the absence of the signal-of-interest. We call $x_{prim}(t)$ the primary sub-array output and $\mathbf{w}^H\mathbf{x}_{aux}(t)$ the output of the auxiliary sub-array, with $\mathbf{w}$ the beamforming weight vector to be optimized. The mean squared error between these two sub-arrays is formulated as:

$$\begin{aligned} \mathrm{MSE}(\mathbf{w}) &= \mathbb{E}\{\mid x_{prim}(t) - \mathbf{w}^H\mathbf{x}_{aux}(t) \mid^2\} && (3.5)\\ &= \sigma^2_{x_{prim}} - \mathbf{w}^H\mathbf{r}_{\mathbf{x_{aux}x_{prim}}} - \mathbf{w}^T{\mathbf{r}_{\mathbf{x_{aux}x_{prim}}}}^* + \mathbf{w}^H\mathbf{R}_{aux}\mathbf{w} && (3.6)\end{aligned}$$

with:

- $\sigma^2_{x_{prim}}$ the power of the primary sub-array output,
- $\mathbf{r}_{\mathbf{x_{aux}x_{prim}}}$ the correlation vector between the beamformed primary sub-array output and the auxiliary sub-array output vector,
- $\mathbf{R}_{aux}$ the auxiliary sub-array output vector correlation matrix.

The function MSE($\mathbf{w}$) has to be minimal in the absence of the source-of-interest's signal. Its derivative function with respect to $\mathbf{w}$ is [56]:

$$\frac{\partial}{\partial \mathbf{w}} MSE(\mathbf{w}) = -\mathbf{r}_{\mathbf{x_{aux}x_{prim}}} + \mathbf{R}_{aux}\mathbf{w} \tag{3.7}$$

Nulling this derivative function leads to the statistically optimal MSC beamformer:

$$\mathbf{w}_{MSC} = \mathbf{R}^{-1}_{aux}\mathbf{r}_{\mathbf{x_{aux}x_{prim}}} \tag{3.8}$$

Even if this beamforming technique requires the absence of the signal-of-interest, it might still be suitable for radio astronomical applications. The weak power of cosmic sources makes their contribution to the total output power very low compared to the system noise and interference signals. Therefore, applying

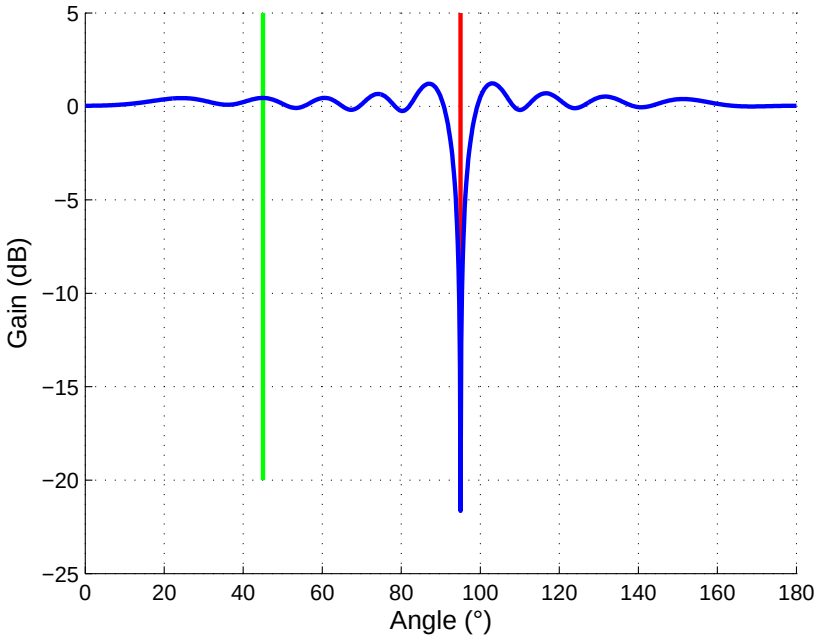

Figure 3.5: Directivity pattern obtained with a multiple sidelobe canceller beamformer. Computed using a simulated uniform linear antenna array made of 10 antennas with $\frac{\lambda}{2}$ spacing. One antenna was used as a primary channel, the nine other antennas were used as the auxiliary sub-array. Covariance matrices calculated over 32768 samples. SNR = 0 dB. INR = 0 dB. The green line corresponds to the signal of interest direction, the red line is the RFI direction.

the MSC beamformer on a phased antenna array radio telescope would improve the observation in a corruptive environment anyway, even with a continuous weak cosmic source of interest impinging the array.

Figure 3.5 shows an example of a Multiple Sidelobe Canceller directivity pattern. This pattern was calculated after simulating a white Gaussian signal of interest (with direction highlighted with a green line) and a white Gaussian interference (with direction highlighted with a red line), with a 0 dB Signal to Noise Ratio and a 0 dB interference to noise ratio, impinging a uniform linear antenna array made of 10 antennas with $\frac{\lambda}{2}$ spacing. The covariance matrices were calculated over n = 32768 samples. One antenna was used here as a primary channel (instead of a sub-array), and the nine remaining antennas as the auxiliary sub-array.

As long as cosmic sources can be neglected regarding the interfering signals, the MSC beamformer automatically rejects the interference direction of arrival. If the latter condition does not hold, it would be necessary to consider another kind of spatial filtering.

3.2.3 Maximum SNR beamformer

The aim of the *Maximum Signal-to-Noise Ratio* beamformer is to maximize the signal-to-noise ratio at the output of the antenna array beamformer $\mathbf{w}_{maxSNR}$. Both system noise and interference are here considered as a global noise term. We consider here the data model based on the one expressed in Equation 2.14:

$$\mathbf{R} = \sigma_c^2 \mathbf{a}_c \mathbf{a}_c^H + \mathbf{R}_{\mathbf{r+n}} \tag{3.9}$$

where $\mathbf{R}_{\mathbf{r+n}} = \mathbf{A}_\mathbf{r} \cdot \mathbf{R}_\mathbf{r} \cdot {\mathbf{A}_\mathbf{r}}^H + \mathbf{R}_\mathbf{n}$. According to this covariance data model, the Signal-to-Noise Ratio at the output of a beamformer $\mathbf{w}$ is defined as:

$$\text{SNR} = \sigma_c^2 \frac{\mathbf{w}^H \mathbf{a}_c \mathbf{a}_c^H \mathbf{w}}{\mathbf{w}^H \mathbf{R}_{\mathbf{r+n}} \mathbf{w}} \tag{3.10}$$

The problem of the SNR beamformer is then written as [97]:

$$\hat{\mathbf{w}}_{maxSNR} = \underset{\mathbf{w}}{\text{argmax}}\ \sigma_c^2 \frac{\mathbf{w}^H \mathbf{a}_c \mathbf{a}_c^H \mathbf{w}}{\mathbf{w}^H \mathbf{R}_{\mathbf{r+n}} \mathbf{w}} \tag{3.11}$$

With $\hat{\mathbf{w}}_{maxSNR}$ the estimate of the Maximum SNR beamformer weights vector.

The solution of this optimization problem is given by the following Generalized Eigenvalue problem:

$$\sigma_c^2 \mathbf{a}_c \mathbf{a}_c^H \mathbf{w}_{maxSNR} = \lambda_{maxSNR} \mathbf{R}_{\mathbf{r+n}} \mathbf{w}_{maxSNR} \tag{3.12}$$

where $\mathbf{w}_{maxSNR}$ is the eigenvector of the matrix $\sigma_c^2 {\mathbf{R}_{\mathbf{r+n}}}^{-1} \mathbf{a}_c \mathbf{a}_c^H$ associated with its larger eigenvalue λ_{maxSNR}, assuming $\mathbf{R}_{\mathbf{r+n}}$ is invertible. This assumption usually holds since the system noise covariance matrix is by nature full rank. Therefore, $\mathbf{R}_{\mathbf{r+n}}$ is full rank and invertible.

However, this technique requires an estimate or knowledge of $\mathbf{R}_{\mathbf{r+n}}$ and $\mathbf{a}_c$. The vector $\mathbf{a}_c$ corresponds to the direction of interest (cosmic source of interest direction). The matrix $\mathbf{R}_{\mathbf{r+n}}$ corresponds to the antenna array covariance matrix $\mathbf{R}$ when the cosmic source of interest is not located in its field of view or is weak enough to be neglected. This matrix can therefore be estimated using the antenna array correlator output if the cosmic source is absent. Techniques to estimate the interference-only covariance matrix are presented in the following chapter.

Figure 3.6 shows the directivity pattern obtained with a maximum SNR beamformer on a uniform linear array made of 10 antennas with $\frac{\lambda}{2}$ spacing. The covariance matrix was simulated using a single interference and a calibrated uncoupled system noise with a 0 dB interference to noise ratio. The interference direction is highlighted by a red line on the figure, and the direction of interest by a green line.

The Maximum Signal-to-Noise Ratio beamformer achieves the best SNR possible at the output of the antenna array radio telescope. However, this condition only holds if the noise covariance matrix $\mathbf{R}_{\mathbf{r+n}}$ is known. Any estimation error for this matrix would lower the expected performance.

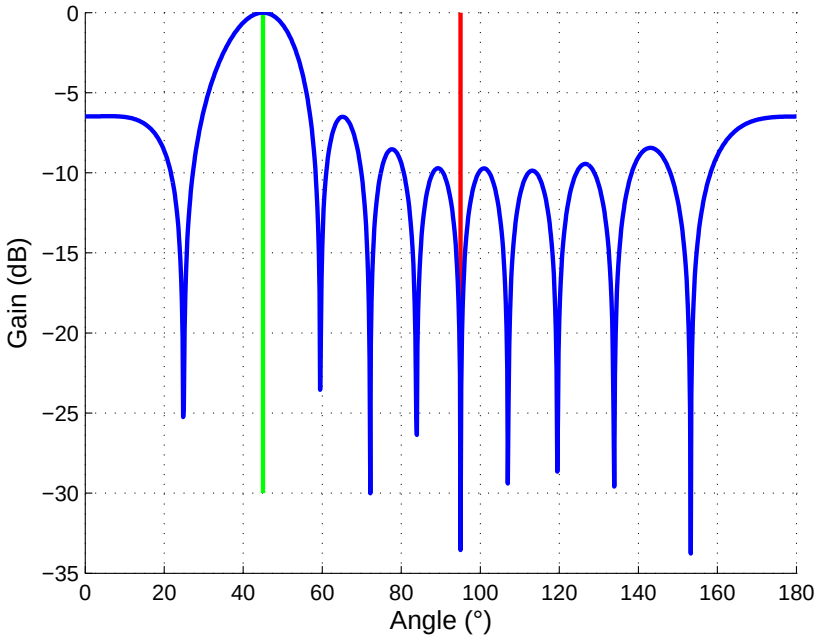

Figure 3.6: Directivity diagram obtained with a maximum SNR beamformer. Computed using a simulated uniform linear antenna array made of 10 antennas with $\frac{\lambda}{2}$ spacing. Single interference and calibrated uncoupled system noise (INR = 0 dB) .The green line corresponds to the signal of interest's direction, the red line is the RFI direction.

3.2.4 LCMV beamformer

The *Linearly Constrained Minimum Variance (LCMV)* beamformer is a technique based on the minimization of the antenna array output variance constrained to a constant gain g in the direction of the source-of-interest. The constrained optimization problem is formulated as follows:

$$\mathbf{w}_{LCMV} = \underset{\mathbf{w}}{\operatorname{argmin}}\ \mathbf{w}^H \mathbf{R} \mathbf{w}, \quad \text{subject to } \mathbf{w}^H \mathbf{a}_c = g \tag{3.13}$$

This optimization can be solved using the Lagrange multipliers technique. Using this technique, the Lagrange function related to this problem becomes:

$$\mathbb{L}(\mu, \mathbf{w}) = \mathbf{w}^H \mathbf{R} \mathbf{w} - \mu(\mathbf{w}^H \mathbf{a}_c - g) \tag{3.14}$$

with μ the Lagrange multiplier related to the constraint of the problem. The beamforming vector maximizing this constrained problem is then given by:

$$\mathbf{w}_{LCMV} = g \frac{1}{\mathbf{a}_c^H \mathbf{R}^{-1} \mathbf{a}_c} \mathbf{R}^{-1} \mathbf{a}_c \tag{3.15}$$

When the gain factor g is unitary, this beamformer is also known as the *Minimum Variance Distortionless Response* (MVDR) or Capon beamformer.

The LCMV beamformer can also be extended to multiple constraints [96]. For instance, in the case of known static interference, it can be interesting to add a nulling of the interference direction of arrival as a beamformer constraint. Consider the $(M \times N_r + 1)$ constraint matrix $\mathbf{C}$ containing column wise the steering vector corresponding to the direction of interest (first column) and N_r steering vectors corresponding to N_r static interference. The constraints of this beamformer are then described as:

$$\mathbf{C}^H \mathbf{w}_{LCMV} = \mathbf{g} \tag{3.16}$$

with $\mathbf{g}$ a constraints gain vector such that : $\begin{pmatrix} g & 0 & \cdots & 0 \end{pmatrix}^T$. The corresponding LCMV vector $\mathbf{w}_{LCMV}$ is then defined by the following expression:

$$\mathbf{w}_{LCMV} = \mathbf{R}^{-1} \mathbf{C} (\mathbf{C}^H \mathbf{R}^{-1} \mathbf{C})^{-1} \mathbf{g} \tag{3.17}$$

Figure 3.7 is a directivity pattern obtained using a LCMV beamformer. This beamformer was applied to a uniform linear antenna array made of 10 antennas with $\frac{\lambda}{2}$ spacing. The simulated covariance matrix involves one signal of interest, with direction highlighted by a green line on the figure, and an interference, with direction highlighted by a red line. The signal to noise ratio and interference to noise ratio are both 0 dB.

Even if this beamforming technique seems computationally expensive and hard to implement, its major advantage is that it does not require any a priori knowledge concerning the interference and system noise contributions in order to build it. However, injecting a priori knowledge concerning the jammers locations is possible with multiple constraints, and can improve its performances as long as jammers remain static.

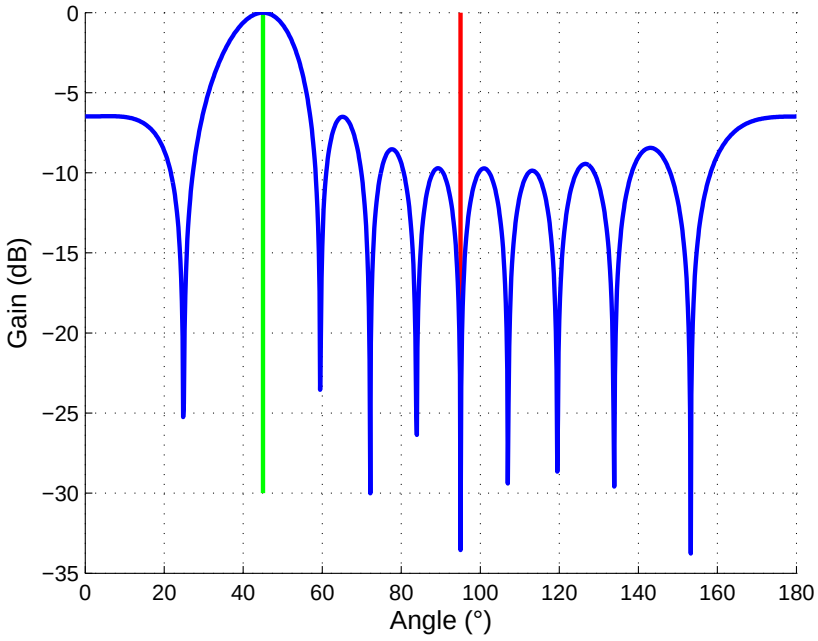

Figure 3.7: Directivity pattern obtained with a LCMV beamformer. Computed using a simulated uniform linear antenna array made of 10 antennas with $\frac{\lambda}{2}$ spacing. One signal of interest, One interference, SNR = 0 dB, INR = 0 dB. The green line corresponds to the signal of interest direction, the red line is the RFI direction.

3.2.5 Conclusions on beamforming techniques

Beamforming has been extensively studied [103, 65, 100], especially for telecommunication applications [106]. These techniques are usually based on the signal of interest properties (like wideband [32] or cyclostationary [27, 26] properties).

In radio astronomy, the signals of interest do not present particular characteristics since cosmic sources can be described as white Gaussian noise signals. That is the reason why most of the beamforming techniques cannot be applied to this field. Some radio astronomical beamforming applications can still be found in the literature [36, 87].

Spatial filtering is not limited to beamforming techniques. The next section presents other approaches based on projections that use a phased antenna array covariance matrix.

3.3 Projection techniques

The phased antenna array radio telescope data covariance matrix can be seen, from a linear algebra point of view, as a linear transform matrix. This matrix generates a vector space called the *data vector space*. By construction, this vector space is made of three subspaces known as *RFI subspace*, *cosmic source subspace* and *system noise subspace*. While the system noise subspace is considered as spatially white, i.e. uniformly distributed along the data vector space, the RFI and cosmic source subspaces are defined by sub-basis. The steering vectors of all interferences (respectively cosmic sources) are seen as an RFI (respectively cosmic source) subspace basis. However, a subspace basis is not unique, i.e. different sets of vectors can generate the same subspace. This topic will be addressed in the following chapter.

The general idea of projection is to extend the kernel of a data covariance matrix, usually limited by the vector $\mathbf{0}$, to the interference subspace. This operation is called *nulling* the RFI subspace. The consequence on the radio astronomical observation is then the nulling of the power coming from the jammers directions of arrival.

3.3.1 Orthogonal projection

Concept

Figure 3.8 illustrates an example of a 2-dimensional data vector space in a noise-free scenario. Both red and black vectors represent the steering vectors associated with respectively a cosmic source and an RFI source. They therefore generate the cosmic source and the RFI subspaces. The norm of these vectors represents the power of each one of these sources.

The underlying concept of interference mitigation using an orthogonal projector is to project the data vector space onto a subspace that is orthogonal to the RFI subspace, and parallelly to it [83]. The projected RFI subspace is completely nulled. The resulting data then contain only the cosmic source contribution. It can clearly be seen on the figure that the recovered cosmic source power, after projection, is attenuated by a factor depending on the angle between interference and cosmic source. Geometrically, if $\sigma^2_{s_{proj}}$ is the recovered cosmic source's power after projection, then:

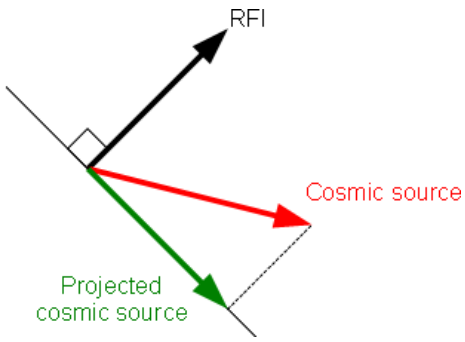

Figure 3.8: Illustration of the orthogonal projection applied to a 2-dimensional data vector space

$$\sigma^2_{s_{proj}} = \sigma^2_s . \sin(\theta_{\mathbf{a}_c,\mathbf{a}_{r_n}}) \tag{3.18}$$

with σ^2_s the true cosmic source power and $\theta_{\mathbf{a}_c,\mathbf{a}_{r_n}}$ the angle between the cosmic source and interference. Except in the case of orthogonality, the cosmic source will not be recovered perfectly without attenuation.

Orthogonal projector construction

Consider a finite-dimensional vector space V and two vector subspaces V_1 and V_2 so that V can be written as a direct sum $V = V_1 \oplus V_2$. For each vector $\mathbf{x} \in V$, a unique couple $(\mathbf{x_1}, \mathbf{x_2}) \in (V_1 \times V_2)$ exists so that $\mathbf{x} = \mathbf{x_1} + \mathbf{x_2}$. The projection p onto V_1 and parallel to V_2 is a linear transform defined by the following projection equation:

$$p(\mathbf{x}) = p(\mathbf{x_1} + \mathbf{x_2}) = \mathbf{x_1} \tag{3.19}$$

Moreover, if V_1 and V_2 are orthogonal, then the transform p is an orthogonal projection.

A projection has the following properties:

- $p(\mathbf{x}) = \mathbf{x} \quad \leftrightarrow \quad \mathbf{x} \in V_1$
- $\operatorname{Ker} p = V_2$
- $\operatorname{Im} p = V_1$
- p is idempotent : $p \circ p = p$

Like any linear transform, p can be written in a matrix form $\mathbf{P}$. Any projection matrix is diagonalizable. In the case of an orthogonal projection, the matrix is hermitian and therefore admits an orthogonal eigenvalue decomposition. Its eigenvalues are '0' or '1'. Unitary eigenvectors corresponding to the '0' eigenvalues generate the projection *kernel subspace*, and unitary eigenvectors corresponding to the '1' eigenvalues generate the *range subspace*. The rank of a projection matrix is therefore equal to the dimension of its range subspace. If $\mathbf{H}$ is a projection range subspace basis and $\mathbf{K}$ a projection kernel subspace basis, we have:

$$\begin{cases} \mathbf{P} \cdot \mathbf{H} &= \mathbf{H} \\ \mathbf{P} \cdot \mathbf{K} &= \mathbf{0} \end{cases}$$

The orthogonal projector with range generated by the basis matrix $\mathbf{H}$ is then defined by:

$$\mathbf{P} = \mathbf{H}(\mathbf{H}^H\mathbf{H})^{-1}\mathbf{H}^H \tag{3.20}$$

The orthogonal projector whose range is the subspace orthogonal to $\mathbf{H}$ is denoted $\mathbf{P}^\perp$ and defined by:

$$\mathbf{P}^\perp = \mathbf{I} - \mathbf{H}(\mathbf{H}^H\mathbf{H})^{-1}\mathbf{H}^H \tag{3.21}$$

Application to antenna array radio telescopes

Without any loss of generality, we consider here the following single interference data model:

$$\mathbf{x}(t) = \mathbf{a}_r r(t) + \mathbf{A_c} \cdot \mathbf{c}(t) + \mathbf{n}(t) \tag{3.22}$$

The interference subspace of this data model is here 1-dimensional. The orthogonal projector projecting data onto the interference subspace is defined by [5, 89]:

$$\mathbf{P} = \mathbf{a}_r(\mathbf{a}_r^H\mathbf{a}_r)^{-1}\mathbf{a}_r^H \tag{3.23}$$

The orthogonal projector projecting data onto a subspace orthogonal to the interference subspace, so that both of these subspaces are in a direct sum, is defined by:

$$\mathbf{P}^\perp = \mathbf{I} - \mathbf{a}_r(\mathbf{a}_r^H\mathbf{a}_r)^{-1}\mathbf{a}_r^H \tag{3.24}$$

In the case of a multiple interference scenario, such as the data model defined in equation 3.1 for example, the interference subspace is multi-dimensional. This subspace is the generated by the set of independent RFI steering vectors stored in the matrix $\mathbf{A_r}$. In the same way, the orthogonal projector projecting data onto a subspace orthogonal to the latter is defined by:

$$\mathbf{P}^\perp = \mathbf{I} - \mathbf{A_r}(\mathbf{A_r}^H\mathbf{A_r})^{-1}\mathbf{A_r}^H \tag{3.25}$$

An orthogonal projector can be applied at either *pre* or *post-correlation* stages on a phased antenna array radio telescope data flow. At the *pre-correlation* stage, the available data is the antenna array output data vector $\mathbf{x}(t)$. The corrected data vector $\mathbf{x}_{clean}(t)$ is then calculated in the following way:

$$\mathbf{x}_{clean}(t) = \mathbf{P}^\perp\mathbf{x}(t) \tag{3.26}$$

At the *post-correlation* stage, the available data is the antenna array output covariance matrix $\mathbf{R}$. The corrected covariance matrix $\mathbf{R}_{clean}$ is then obtained with:

$$\mathbf{R}_{clean} = \mathbf{P}^\perp\mathbf{R}\mathbf{P}^{\perp H} \tag{3.27}$$

$$= \mathbf{P}^\perp\mathbf{R}\mathbf{P}^\perp \tag{3.28}$$

Performances and correction

We consider here the following narrowband data model based on a single interference and a single cosmic source:

$$\mathbf{x}(t) = \mathbf{a_c} c(t) + \mathbf{a_r} r(t) + n(t) \tag{3.29}$$

The covariance matrix of this data model, assuming the array is calibrated and the signals mutually independent, is given by:

$$\begin{aligned} \mathbf{R} &= \mathbb{E}\{\mathbf{x}\mathbf{x}^H\} && (3.30)\\ &= \sigma_c^2 \mathbf{a_c}\mathbf{a_c}^H + \sigma_r^2 \mathbf{a_r}\mathbf{a_r}^H + \sigma_n^2 \mathbf{I} && (3.31) \end{aligned}$$

with σ_c^2, σ_r^2 and σ_n^2 respectively the powers of the cosmic source signal, the interference signal and the system noise. We will consider in the following the signals to be stationary and the covariance matrix only given for a time-lag $\tau = 0$. Thus, we will omit the time and time-lag dependence in the covariance data model.

The power reached in the arbitrary direction given by the steering vector $\mathbf{w}$ is:

$$\sigma_w^2 = \mathbf{w}^H \mathbf{R} \mathbf{w} \tag{3.32}$$

σ_w^2 is obviously corrupted by the interference and the cosmic sources impinging the antenna array through the side lobes generated by the spatial filter $\mathbf{w}$. We consider now the power $\sigma_{w_{clean}}^2$ calculated with the cleaned covariance matrix given in equation 3.28:

$$\begin{aligned} \sigma_{w_{clean}}^2 &= \mathbf{w}^H \mathbf{R}_{clean} \mathbf{w} && (3.33)\\ &= \mathbf{w}^H \mathbf{P}^\perp \mathbf{R} \mathbf{P}^\perp \mathbf{w} && (3.34)\\ &= \mathbf{w_{orth}}^H \mathbf{R} \mathbf{w_{orth}} && (3.35) \end{aligned}$$

with $\mathbf{w_{orth}} = \mathbf{P}^\perp \mathbf{w}$ the orthogonal projection beamforming vector. Expanding this equation, we find out its closed form expression:

$$\begin{aligned} \sigma_{w_{clean}}^2 = \sigma_c^2 \left(\|\rho_{a_c}\|^2 - 2\,\mathrm{Re}(\rho^* \rho_{a_c}^* \rho_{a_r}) + \|\rho\|^2 \|\rho_{a_r}\|^2 \right) && (3.36)\\ + \sigma_n^2 \left(1 - \|\rho_{a_r}\|^2\right) && (3.37) \end{aligned}$$

with:

- ρ the dot product between $\mathbf{a_r}$ and $\mathbf{a_c}$: $\rho = \mathbf{a_r}^H \mathbf{a_c}$
- ρ_{a_r} the dot product between $\mathbf{w}$ and $\mathbf{a_r}$: $\rho_{a_r} = \mathbf{w}^H \mathbf{a_r}$
- ρ_{a_c} the dot product between $\mathbf{w}$ and $\mathbf{a_c}$: $\rho_{a_c} = \mathbf{w}^H \mathbf{a_c}$

The interference no longer contributes to the recovered power $\sigma_{w_{clean}}^2$. If the source of interest is the cosmic source, beamforming in its direction leads to $\mathbf{w} = \mathbf{a_c}$. In this case, the cosmic source power is attenuated by a factor

depending on the dot product between the interference subspace and the cosmic source subspace:

$$\sigma^2_{a_{cclean}} = \sigma^2_c(1 - \|\rho\|^2)^2 + \sigma^2_n(1 - \|\rho\|^2) \tag{3.38}$$

If these subspaces are orthogonal (this configuration is not likely), we have $\rho = \rho_{a_r} = 0$ and $\rho_{a_c} = \|\mathbf{a_c}\|^2$. The recovered power $\sigma^{\perp 2}_{a_{cclean}}$ becomes:

$$\sigma^{\perp 2}_{a_{cclean}} = \sigma^2_c + \sigma^2_n \tag{3.39}$$

The orthogonal projector modifies the cosmic sources subspace. Raza et al. ([83], see also [93])proposed a correction technique allowing an unbiased estimation of the cosmic source and noise covariance matrix. Based on knowledge of the orthogonal projection matrix, the modified remaining subspace can then be corrected.

The correction matrix, applied to the projected covariance matrix $\mathbf{R}_{clean}$ is based on the projection matrix $\mathbf{P}^{\perp}$ and needs to be invertible. The technique proposed by Raza et al. therefore uses time-averaged short term projection matrices. The related issue is the interference subspace estimation error that increases with the covariance matrix time integration reduction. The projection matrices might then be inefficient to project the RFI subspace out of the data vector space. Moreover, the correction technique is computationally expensive (requiring multiple covariance matrices).

Based on these observations, we propose an oblique projection approach that does not require any correction to retrieve the signal of interest subspace [54]. This approach requires more a priori information, but presents the important advantage (in radio astronomy) of not distorting the cosmic source of interest subspace.

3.3.2 Oblique projection

Concept

Although the orthogonal projection performs deep RFI nulling, the distortion of the recovered cosmic source subspace remains an issue. This distortion is due to a data vector space projection onto a subspace depending on the interference subspace only, i.e. orthogonal to this subspace, without taking the cosmic source of interest into account. Figure 3.9 shows the 2-dimensional concept of an oblique projection. Here again, the black arrow represents the interference subspace, and the red arrow represents the cosmic source subspace. Their norms define their respective powers.

The projection is still done parallel to the interference subspace, but this time onto the cosmic source subspace. As can be seen on the figure, the cosmic source subspace is perfectly recovered. This projection is equivalent to an orthogonal projection in the case of orthogonality between the cosmic source and the interference subspaces. But this condition is no longer needed with an oblique projector.

Oblique projection construction

It has been seen in the previous section that the orthogonal projection can be defined according to either its range subspace or its kernel subspace since both

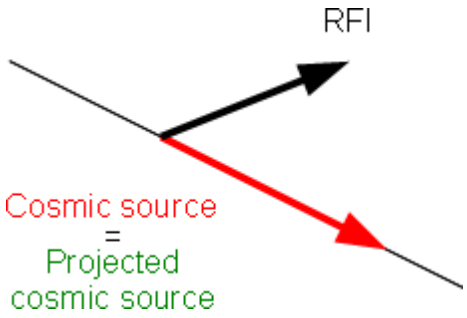

Figure 3.9: Illustration of the oblique projection applied to a 2-dimensional data vector space

subspaces are involved in a direct sum. The oblique projector [13] is based on the orthogonal projector, taking only its range subspace in account. Keeping the same notations as before, we saw that $\mathbf{H}$ is a matrix defining the range subspace of the orthogonal projector $\mathbf{P}$. No assumption was made on the orthogonality of this matrix. We can therefore split this basis matrix into two sub-bases $\mathbf{H_1}$ and $\mathbf{H_2}$ such that $\mathbf{H} = \mathbf{H_1} \oplus \mathbf{H_2}$, i.e. the subspaces generated by $\mathbf{H_1}$ and $\mathbf{H_2}$ are involved in a direct sum:

$$\mathbf{H} = [\mathbf{H_1}\ \mathbf{H_2}] \tag{3.40}$$

$\mathbf{H_1}$ and $\mathbf{H_2}$ therefore generate two distinct subspaces of $\mathbf{H}$, but do not have to be orthogonal. We can now write the expression of the orthogonal projection whose range subspace is defined by the matrix $\mathbf{H}$:

$$\mathbf{P} = \mathbf{H}(\mathbf{H}^H\mathbf{H})^{-1}\mathbf{H}^H \tag{3.41}$$

$$= \begin{bmatrix}\mathbf{H_1} & \mathbf{H_2}\end{bmatrix} \begin{bmatrix}\mathbf{H_1}^H\mathbf{H_1} & \mathbf{H_1}^H\mathbf{H_2} \\ \mathbf{H_2}^H\mathbf{H_1} & \mathbf{H_2}^H\mathbf{H_2}\end{bmatrix}^{-1} \begin{bmatrix}\mathbf{H_1}^H \\ \mathbf{H_2}^H\end{bmatrix} \tag{3.42}$$

Using the following analytic blockwise inversion formula:

$$\begin{bmatrix}\mathbf{A} & \mathbf{B} \\ \mathbf{C} & \mathbf{D}\end{bmatrix}^{-1} = \begin{bmatrix}\mathbf{A}^{-1} + \mathbf{A}^{-1}\mathbf{B}(\mathbf{D}-\mathbf{C}\mathbf{A}^{-1}\mathbf{B})^{-1}\mathbf{C}\mathbf{A}^{-1} & -\mathbf{A}^{-1}\mathbf{B}(\mathbf{D}-\mathbf{C}\mathbf{A}^{-1}\mathbf{B})^{-1} \\ -(\mathbf{D}-\mathbf{C}\mathbf{A}^{-1}\mathbf{B})^{-1}\mathbf{C}\mathbf{A}^{-1} & (\mathbf{D}-\mathbf{C}\mathbf{A}^{-1}\mathbf{B})^{-1}\end{bmatrix} \tag{3.43}$$

we get the following expression of $\mathbf{P}$:

$$\mathbf{P} = \mathbf{E}_{\mathbf{H_1H_2}} + \mathbf{E}_{\mathbf{H_2H_1}} \tag{3.44}$$

with:

$$\begin{cases} \mathbf{E}_{\mathbf{H_1H_2}} &= \begin{bmatrix}\mathbf{H_1} & \mathbf{0}\end{bmatrix}\begin{bmatrix}\mathbf{H}^H\mathbf{H}\end{bmatrix}^{-1}\begin{bmatrix}\mathbf{H}\end{bmatrix}^H \\ \mathbf{E}_{\mathbf{H_2H_1}} &= \begin{bmatrix}\mathbf{0} & \mathbf{H_2}\end{bmatrix}\begin{bmatrix}\mathbf{H}^H\mathbf{H}\end{bmatrix}^{-1}\begin{bmatrix}\mathbf{H}\end{bmatrix}^H \end{cases}$$

$$\begin{cases} \mathbf{E}_{\mathbf{H_1H_2}} &= \mathbf{H_1}(\mathbf{H_1}^H\mathbf{P}^{\perp}_{H_2}\mathbf{H_1})^{-1}\mathbf{H_1}^H\mathbf{P}^{\perp}_{H_2} \\ \mathbf{E}_{\mathbf{H_2H_1}} &= \mathbf{H_2}(\mathbf{H_2}^H\mathbf{P}^{\perp}_{H_1}\mathbf{H_2})^{-1}\mathbf{H_2}^H\mathbf{P}^{\perp}_{H_1} \end{cases}$$

with $\mathbf{P}^{\perp}_{H_2} = \mathbf{I} - \mathbf{H_2}(\mathbf{H_2}^H\mathbf{H_2})^{-1}\mathbf{H_2}^H$ and $\mathbf{P}^{\perp}_{H_1} = \mathbf{I} - \mathbf{H_1}(\mathbf{H_1}^H\mathbf{H_1})^{-1}\mathbf{H_1}^H$ respectively the orthogonal projectors with range the subspace orthogonal to $\mathbf{H_2}$ and $\mathbf{H_1}$. $\mathbf{E_{H_1H_2}}$ and $\mathbf{E_{H_2H_1}}$ are obviously idempotent and we have:

$$\begin{cases} \mathbf{E_{H_1H_2}H_1} &= \mathbf{H_1} \\ \mathbf{E_{H_1H_2}H_2} &= \mathbf{0} \\ \mathbf{E_{H_2H_1}H_1} &= \mathbf{0} \\ \mathbf{E_{H_2H_1}H_2} &= \mathbf{H_2} \end{cases}$$

$\mathbf{E_{H_1H_2}}$ (resp. $\mathbf{E_{H_2H_1}}$) is therefore a projection matrix with range $\mathbf{H_1}$ (resp. $\mathbf{H_2}$) and kernel $\mathbf{H_2}$ (resp. $\mathbf{H_1}$). This kind of projection allows the parametrization of the range and kernel subspaces without requiring orthogonality between them. Moreover, the kernel subspace of $\mathbf{P}$ being orthogonal to $\mathbf{H}$, this subspace is also part of the kernel subspaces of $\mathbf{E_{H_1H_2}}$ and $\mathbf{E_{H_2H_1}}$.

Applied to an antenna array radio telescope, the oblique projector requires the definition of a range and a kernel subspace. To fit with the problem, the interference subspace will be considered as being the projector's kernel subspace, whereas the direction of interest's steering vector will generate the range subspace of the projector.

Consider the data model defined in equation 3.22. The kernel subspace to choose for this data model will be the one generated by the interference steering vector $\mathbf{a}_r$. Suppose the direction-of-interest is defined by the arbitrary steering vector $\mathbf{w}$. The oblique projector is then defined by:

$$\mathbf{E_{wa}}_r = \mathbf{w}(\mathbf{w}^H\mathbf{P}^{\perp}_{a_r}\mathbf{w})^{-1}\mathbf{w}^H\mathbf{P}^{\perp}_{a_r} \tag{3.45}$$

with $\mathbf{P}^{\perp}_{a_r} = \mathbf{I} - \mathbf{a}_r(\mathbf{a}_r^H\mathbf{a}_r)^{-1}\mathbf{a_r}^H$. Again, if the interference subspace is multidimensional, i.e. the subspace is no longer generated by a single vector $\mathbf{a}_r$ but by an interference subspace basis matrix $\mathbf{A_r}$ (multiple interference scenario), the oblique projector is defined by:

$$\mathbf{E_{wa}}_r = \mathbf{w}(\mathbf{w}^H\mathbf{P}^{\perp}_{\mathbf{A_r}}\mathbf{w})^{-1}\mathbf{w}^H\mathbf{P}^{\perp}_{\mathbf{A_r}} \tag{3.46}$$

with $\mathbf{P}^{\perp}_{\mathbf{A_r}} = \mathbf{I} - \mathbf{A_r}(\mathbf{A_r}^H\mathbf{A_r})^{-1}\mathbf{A_r}^H$.

Like the orthogonal projector, the oblique projector can be applied either before or after the correlation process. Applied on a pre-correlation stage, the received corrected data vector $\mathbf{x}_{clean}(t)$ is obtained in the following way:

$$\mathbf{x}_{clean}(t) = \mathbf{E_{wa}}_r\mathbf{x}(t) \tag{3.47}$$

At the post-correlation stage, the received cleaned output covariance matrix is defined by:

$$\mathbf{R}_{clean} = \mathbf{E_{wa}}_r\mathbf{R}\mathbf{E}^H_{\mathbf{wa}_r} \tag{3.48}$$

The range subspace of the oblique projector can also be multidimensional and defined by a basis made of several steering vectors corresponding to different directions of arrival. However, the building of such a projection matrix has to respect a direct sum between the range and the kernel subspace.

Performances

The oblique projection matrix is applied in the same way as the orthogonal projector to the antenna array covariance matrix. Consider the steering vector $\mathbf{w}$ pointing in an arbitrary direction. The data model used is the one defined in equation 3.29. Applied to its covariance matrix, we have:

$$\sigma^2_{w_{clean}} = \mathbf{w}^H \mathbf{R}_{clean} \mathbf{w} \tag{3.49}$$
$$= \mathbf{w}^H \mathbf{E}_{\mathbf{wa}_r} \mathbf{R} \mathbf{E}^H_{\mathbf{wa}_r} \mathbf{w} \tag{3.50}$$
$$= \mathbf{w_{obl}}^H \mathbf{R} \mathbf{w_{obl}} \tag{3.51}$$

with $\mathbf{w_{obl}} = \mathbf{E}^H_{\mathbf{wa}_r} \mathbf{w}$ the oblique projection beamforming vector. With the same notations as 3.37, the closed form expression of $\sigma^2_{w_{clean}}$ for the considered data model becomes:

$$\sigma^2_{w_{clean}} = \sigma_c^2 \frac{1}{(1-|\rho_{a_r}|^2)^2} \left(|\rho_{a_c}|^2 - 2\,\mathrm{Re}(\rho^* \rho^*_{a_c} \rho_{a_r}) + |\rho|^2 |\rho_{a_r}|^2 \right) \tag{3.52}$$
$$+ \sigma_n^2 \frac{1}{1-|\rho_{a_r}|^2} \tag{3.53}$$

Beamforming the array in the direction of the cosmic source of interest leads again to $\mathbf{w} = \mathbf{a}_c$. This time, the recovered power is expressed by:

$$\sigma^2_{a_{cclean}} = \sigma_c^2 + \sigma_n^2 \frac{1}{1-|\rho|^2} \tag{3.54}$$

Reasoning in term of signals contributions recovery, the cosmic source contribution is totally recovered after an oblique projection beamforming. However, the noise contribution is amplified by a factor depending on the dot product between the interference and the cosmic source subspaces.

3.3.3 Comparison between oblique and orthogonal projection beamforming techniques

Table 3.1 summarizes the effect of the spatial filtering methods on SOI, RFI and noise powers (resp. P_{SOI}, P_{RFI} and P_{noise}) using the classic delay-and-sum beamforming (σ^2_{class}), orthogonal projection beamforming (σ^2_{orth}) and oblique projection beamforming (σ^2_{obl}), with σ_s^2 the true SOI power and σ_r^2 the true RFI power. According to this table, the oblique projection beamforming approach is able to recover the power reached in the SOI direction without any error whereas the orthogonal projection beamforming presents an error whose magnitude depends on the dot product ρ.

Figure 3.10 shows the relative error of these techniques in a noise-free scenario (i.e. $\sigma_n^2 = 0$). This relative error is defined as

$$\epsilon = \frac{P_{SOI} - \sigma_s^2}{\sigma_s^2} \tag{3.55}$$

The simulation parameters are:

	σ^2_{class}	σ^2_{orth}	σ^2_{obl}
P_{SOI}	σ^2_s	$\sigma^2_s(1-\lvert\rho\rvert^2)^2$	σ^2_s
P_{RFI}	$\sigma^2_r\rho^2$	0	0
P_{noise}	σ^2_n	$\sigma^2_n(1-\lvert\rho\rvert^2)$	$\sigma^2_n(1-\lvert\rho\rvert^2)^{-1}$

Table 3.1: SOI, RFI and noise power after classic delay-and-sum beamforming, orthogonal and oblique projection beamforming.

- 60 randomly distributed antennas array,
- One cosmic source with power -5 dB,
- One interference with Interference to Signal Ratio = $+30$ dB.

The relative errors made with the Delay and Sum beamformer and the Orthogonal projector are highly dependent on the dot product between the interference steering vector and the source of interest steering vectors. The relative error made with an oblique projector is constant over this dot product range (from 0 to 1), its value is around 10^{-14}. No matter what the method, the relative error will always be maximum when the dot product between the interference and the source of interest subspaces equals 1. In this case, both subspaces are mingled.

Figure 3.11 depicts maps made with beamforming over the field of view of a simulated randomly distributed $M = 48$-antenna array radio telescope. The interference is +10 dB stronger than the cosmic source, in a noise-free scenario. Covariance matrices are estimated over 2048 samples. Figure 3.11.(a) and Figure 3.11.(b) show respectively a skymap without interference and a skymap corrupted by a strong interference (INR = +10 dB). Figure 3.11.(c) and Figure 3.11.(d) are respectively the corrupted data after orthogonal and oblique projection. Figure 3.11.(e) and Figure 3.11.(f) show the relative error between the data processed by the orthogonal projector and the interference free data, and between the data processed by the oblique projection beamforming and the interference free data respectively, over a small area around the cosmic source of interest.

These simulations show that the oblique projection approach, although more information is required to build it than for the orthogonal projector approach, offers less distortion on the recovered power.

Closely related to the projection approach, the interference subspace subtraction is another spatial filtering approach based on the additive and uncorrelated radio astronomical data model. With this approach, each interference steering vector has to be known or estimated. The interference contributions are then removed one after the other from the data model after estimating their power.

3.4 Interference subspace subtraction

As the interference subspace has to be estimated anyway, another approach consists in subtracting it from the antenna array covariance matrix. Let's consider the following covariance data model:

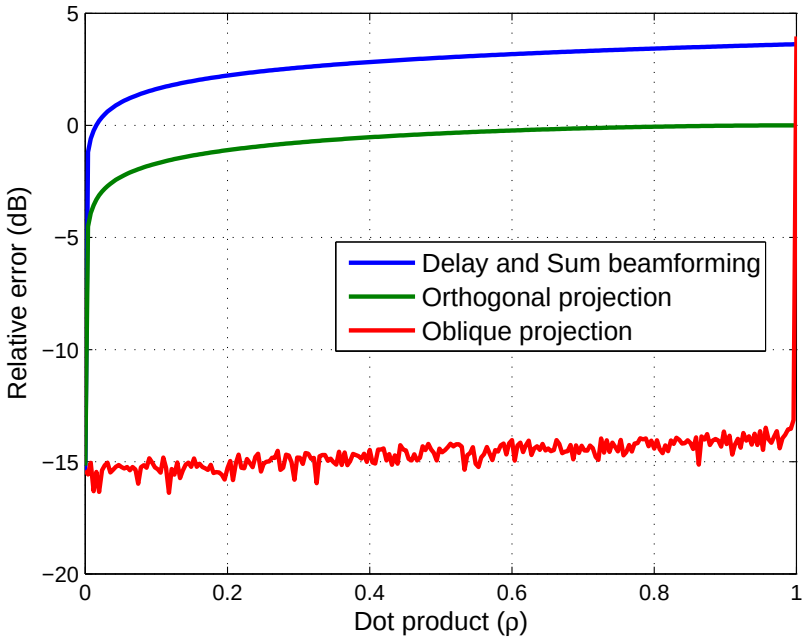

Figure 3.10: Relative error of the Delay and Sum beamforming, Orthogonal and Oblique projection beamforming techniques. $M = 60$ randomly distributed antennas, noise-free model, one cosmic source (power $= -5$ dB), one interference (Interference to Signal Ratio $= +30$ dB), averaged over 512 trials.

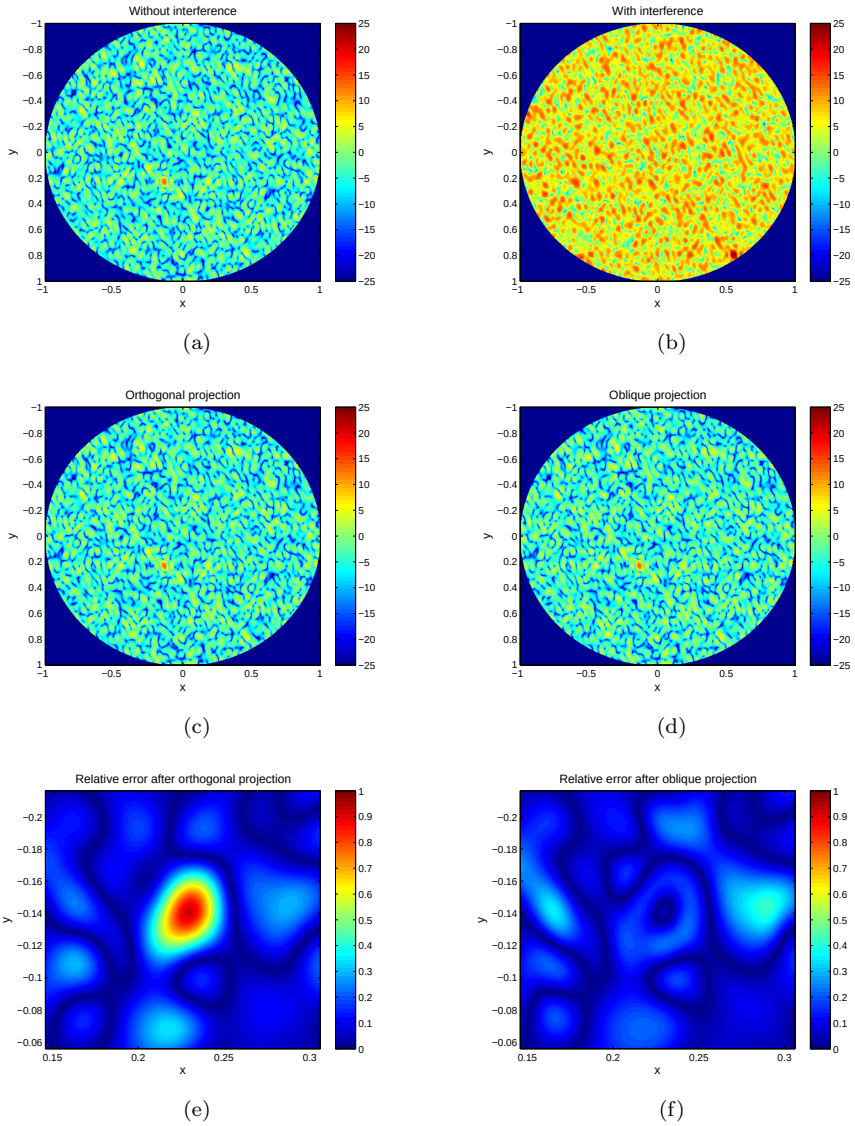

(a) (b) (c) (d) (e) (f)

Figure 3.11: Example of beamforming imaging with a simulated randomly distributed $M = 48$-antenna array radio telescope. Noise-free model, RFI to SOI ratio = +10 dB, NSamples = 2048. (a) Skymap without interference (in dB). (b) Skymap corrupted by an interference. The cosmic source is no longer visible (in dB). (c) Skymap after orthogonal projection (in dB). (d) Skymap after oblique projection (in dB). (e) Relative error near the cosmic source calculated between the data processed by orthogonal projection beamforming and the interference free data (linear scale). (f) Relative error near the cosmic source calculated between the data processed by oblique projection beamforming and the interference free data (linear scale).

$$\mathbf{R} = \sum_{i=1}^{N_r} \sigma_{r_i}^2 \mathbf{a_{r_i}} \mathbf{a_{r_i}}^H + \mathbf{A_c} \cdot \mathbf{R_c} \cdot \mathbf{A_c}^H + \mathbf{R_n} \tag{3.56}$$

Subtracting the interference contribution from this data model would allow one to recover an interference-free data model:

$$\mathbf{R} - \sum_{i=1}^{N_r} \sigma_{r_i}^2 \mathbf{a_{r_i}} \mathbf{a_{r_i}}^H = \mathbf{A_c} \cdot \mathbf{R_c} \cdot \mathbf{A_c}^H + \mathbf{R_n} \tag{3.57}$$

The next chapter presents different techniques to estimate the interference subspace. In order to apply the interference subspace subtraction technique, it is also necessary to estimate their individual power. We will first consider the case $N_r = 1$. We have then the following data model:

$$\mathbf{R} = \sigma_{r_i}^2 \mathbf{a_r} \mathbf{a_r}^H + \mathbf{R}_{\text{clean}} \tag{3.58}$$

with $\mathbf{R}_{\text{clean}}$ the cosmic sources and noise covariance matrix. The idea behind the subtraction technique is to estimate the right quantity $\sigma_{r_i}^2$ and use it to subtract $\sigma_{r_i}^2 \hat{\mathbf{a}}_\mathbf{r} \hat{\mathbf{a}}_\mathbf{r}^H$, with $\hat{\mathbf{a}}_\mathbf{r}$ the estimated interference steering vector, from $\mathbf{R}$.

The squared Frobenius norm of a covariance matrix is equal to the sum of its squared singular values. Moreover, the sum of a covariance matrix singular values is equal to the total power received at the antenna array. This quantity is therefore larger than or equal to zero. Estimating the interference power then consists in minimizing the following contrast function:

$$f(\xi, \hat{\mathbf{a}}_\mathbf{r}) = \left\| \mathbf{R} - \xi \hat{\mathbf{a}}_\mathbf{r} \hat{\mathbf{a}}_\mathbf{r}^H \right\|_F^2 \tag{3.59}$$

The powers of all signals in the data model (interference, cosmic sources and system noise) being second order statistics, they are positive and the function $f(\xi, \hat{\mathbf{a}}_\mathbf{r})$ admits therefore a global minimum. The interference power estimate $\hat{\sigma}_{r_i}^2$ is then given by:

$$\hat{\sigma}_{r_i}^2 = \underset{\xi}{\operatorname{argmin}}\ f(\xi, \hat{\mathbf{a}}_\mathbf{r}) \tag{3.60}$$

The estimate $\hat{\sigma}_{r_i}^2$ is easily found by derivating $f(\xi, \hat{\mathbf{a}}_\mathbf{r})$:

$$\frac{\partial f}{\partial \xi}(\xi, \hat{\mathbf{a}}_\mathbf{r}) = \frac{\partial}{\partial \xi} \left\| \mathbf{R} - \xi \hat{\mathbf{a}}_\mathbf{r} \hat{\mathbf{a}}_\mathbf{r}^H \right\|_F^2 \tag{3.61}$$

$$= \frac{\partial}{\partial \xi} \text{tr}((\mathbf{R} - \xi \hat{\mathbf{a}}_\mathbf{r} \hat{\mathbf{a}}_\mathbf{r}^H)(\mathbf{R} - \xi \hat{\mathbf{a}}_\mathbf{r} \hat{\mathbf{a}}_\mathbf{r}^H)^H) \tag{3.62}$$

$$= \frac{\partial}{\partial \xi} \text{tr}(\mathbf{R}\mathbf{R}^H) - 2\xi \text{tr}(\mathbf{R} \hat{\mathbf{a}}_\mathbf{r} \hat{\mathbf{a}}_\mathbf{r}^H) + \xi^2 \text{tr}(\hat{\mathbf{a}}_\mathbf{r} \hat{\mathbf{a}}_\mathbf{r}^H \hat{\mathbf{a}}_\mathbf{r} \hat{\mathbf{a}}_\mathbf{r}^H) \tag{3.63}$$

$$= -2\text{tr}(\mathbf{R} \hat{\mathbf{a}}_\mathbf{r} \hat{\mathbf{a}}_\mathbf{r}^H) + 2\xi \text{tr}(\hat{\mathbf{a}}_\mathbf{r} \hat{\mathbf{a}}_\mathbf{r}^H \hat{\mathbf{a}}_\mathbf{r} \hat{\mathbf{a}}_\mathbf{r}^H) \tag{3.64}$$

Nulling this derivative leads to the single global minimum, regarding ξ, of the function $f(\xi, \hat{\mathbf{a}}_\mathbf{r})$:

$$\frac{\partial f}{\partial \xi}(\xi, \hat{\mathbf{a}}_\mathbf{r}) = 0 \tag{3.65}$$

$$\Leftrightarrow \xi = \hat{\sigma}^2_{r_i} = \frac{\mathrm{tr}(\mathbf{R}\hat{\mathbf{a}}_\mathbf{r}\hat{\mathbf{a}}_\mathbf{r}^H)}{\mathrm{tr}(\hat{\mathbf{a}}_\mathbf{r}\hat{\mathbf{a}}_\mathbf{r}^H\hat{\mathbf{a}}_\mathbf{r}\hat{\mathbf{a}}_\mathbf{r}^H)} \tag{3.66}$$

Moreover, if the vector $\hat{\mathbf{a}}_\mathbf{r}$ is built as a unit vector, we have:

$$\hat{\sigma}^2_{r_i} = \mathrm{tr}(\mathbf{R}\hat{\mathbf{a}}_\mathbf{r}\hat{\mathbf{a}}_\mathbf{r}^H) \tag{3.67}$$

Figure 3.12 shows a simulated example involving three weak cosmic sources (SNR $= -5$ dB) and one strong interference (INR $= 0$ dB) (see Figure 3.12.(a)). The constraint function $f(\xi, \hat{\mathbf{a}}_\mathbf{r})$ is shown on Figure 3.12.(b). The interference power $\sigma^2_{r_i}$ is then estimated. The red circle on Figure 3.12.(b) points out the minimum of the function. Using this estimate, a new covariance matrix is built based on this value and the estimated interference subspace, and subtracted from the classical covariance matrix. Figure 3.12.c is the skymap obtained after processing. It is clear that the interference has been mitigated and that the three cosmic sources are much more visible.

The interference subspace subtraction technique can also be used in a multiple interference scenario. In this case, the idea is to iteratively estimate one interference steering vector at a time, and its power using its contrast function $f(\xi, \hat{\mathbf{a}}_{\mathbf{r}_n})$, $n = 1 \dots N_r$. Once the N_r interference steering vectors and powers have been estimated, the cleaned covariance matrix is obtained with:

$$\hat{\mathbf{R}}_{\text{clean}} = \mathbf{R} - \sum_{i=1}^{N_r} \hat{\sigma}^2_{r_i}\hat{\mathbf{a}}_\mathbf{r}\hat{\mathbf{a}}_\mathbf{r}^H \tag{3.68}$$

The interference subspace subtraction technique is not suitable for a pre-correlation real time application, and can only be applied if individual interference steering vectors can be estimated. In a single interference scenario, this technique presents a lower computation cost than the projection techniques.

3.5 Conclusions on spatial filtering

Depending on the antenna array radio telescope use (phased array for single pixel tracking or interferometer for imaging), many spatial filtering techniques can be applied. Different criteria have to be taken in account:

- the available computational power,
- the cosmic source of interest and interference power,
- the expected performances (in terms of interference attenuation and signal of interest recovery),
- the interference subspace estimate quality

The main point of spatial filtering is to recover the signal of interest as much as possible. Beamforming techniques tend to attenuate particular directions of arrival (interference directions of arrival) by keeping a constant gain in the

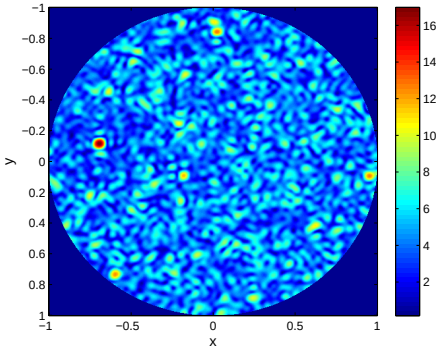

(a)

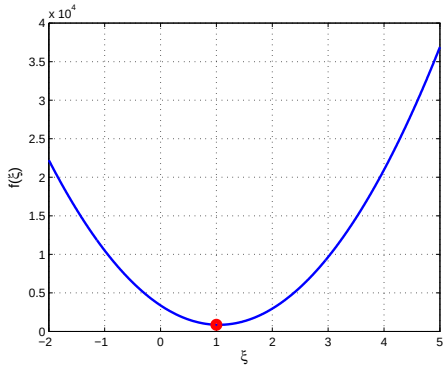

(b)

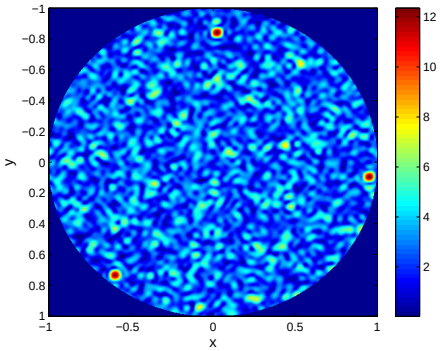

(c)

Figure 3.12: Interference subspace subtraction. Skymaps given in dB. (a) Simulated skymap with three weak cosmic sources (SNR $= -5$ dB) and one strong interference (INR $= 0$ dB). (b) Interference subspace subtraction constraint function depending on ξ. The red circle indicates its global minimum (interference power estimate). (c) Skymap made of the estimated interference covariance matrix subtracted from the classical covariance matrix.

direction of interest. Projection techniques are based on subspace nulling. It has been seen in this chapter that the orthogonal projector might distort the signal of interest subspace, while the oblique projector allows a better recovery of signals of interest.

The Table 3.2 summarizes the different spatial filters presented in this chapter (*MSC*, *Max SNR*, *LCMV*, *Orthogonal* and *Oblique projection*). $\mathbf{x}(t)$ corresponds in this table to the antenna array output vector, whereas $x_{\text{clean}}(t)$ is the filtered and beamformed output. The spatial signature of the cosmic source of interest is $\mathbf{a}_c$. For other definitions, please refer to the corresponding sections.

The Figure 3.13 compares the different techniques presented in this chapter. These techniques are here compared according to their rejection in the direction of the interference and their gain in the direction of the source of interest. The performances are given according to the interference to noise ratio (figures 3.13.(a) and 3.13.(b)), the signal lengths over which the different covariance matrices have been estimated (figures 3.13.(c) and 3.13.(d)) and the dot product between the interference and cosmic source of interest subspaces (figures 3.13.(e) and 3.13.(f)). For each scenario, the results have been averaged over 256 trials. The antenna array is a uniform linear 10-antennas array with $\frac{\lambda}{2}$ spacing. Both simulated interference and signal of interest are white Gaussian noises. The *Delay and Sum beamformer* is not corrected by any apodization window. Concerning the *Multiple Sidelobe Canceller* beamformer, the primary channel is an arbitrary single antenna of the array, and the remaining sub-array is then used as the auxiliary sub-array. The *LCMV beamformer* used in these simulations is the single constraint one (only one constraint concerning the direction of interest). Both interference and cosmic source of interest spatial signatures are here perfectly known.

Unlike the *Delay and Sum beamformer*, the other three beamformers presented in this chapter (*Multiple Sidelobe Canceller*, *Maximum SNR beamformer* and *LCMV beamformer*) require extra knowledge for their calculation (a priori knowledge about the signal of interest or the interference and system noise contributions). Any lack of information or estimation error would lead to much lower performances than expected. The simulations presented here do not take these uncertainties into account.

Beamforming techniques based on a covariance matrix are highly sensitive to the number of samples over which the matrix has been estimated. The *Delay and Sum beamformer* does not show any variation regarding the simulation parameters. This result was expected since no information about the corruptive environment is taken into account during its construction. The *Multiple Sidelobe Canceller* usually performs poorly. Even if its performances asymptotically tend to those of the *Maximum SNR beamformer* and *LCMV beamformer*, this beamformer is not suitable for real time applications. The *Maximum SNR beamformer* performances are as good as those of the *LCMV beamformer*.

Concerning the projection techniques, rejection in the direction of the interference is in each scenario much better than any beamforming technique, except for the *Oblique projector* when the cosmic source subspace tends to be mingled with the interference subspace. However, the recovery of the cosmic source is better with the *Oblique projector* than with the *Orthogonal projector* since the gain in its direction is 0 dB in any scenario. The gain in the direction of interest is affected by the dot product between the signal subspaces when using the *Orthogonal projector*.

The interference subspace estimation is crucial for spatial filtering techniques. The weakness of cosmic sources imposes long time data integration in order for their signals to emerge from the noise level. Any interference filtered out with a poor interference subspace estimation, regardless of the filtering technique, will still corrupt the data and make it unusable for further astronomical processing. The next chapter addresses this problem.

	Definition	Output	Vector
MSC	$\mathbf{r}_{\mathbf{x}_{\text{aux}}\mathbf{x}_{\text{prim}}} = \mathbb{E}\{\mathbf{x}_{\text{aux}}(t)x^*_{\text{prim}}(t)\}$ $\mathbf{R}_{\text{aux}} = \mathbb{E}\{\mathbf{x}_{\text{aux}}(t)\mathbf{x}^H_{\text{aux}}(t)\}$	$x_{\text{clean}}(t) = x_{\text{prim}}(t) - \mathbf{w}^H_{\text{MSC}}\mathbf{x}_{\text{aux}}(t)$	$\mathbf{w}_{\text{MSC}} = \mathbf{R}^{-1}_{\text{aux}}\mathbf{r}_{\mathbf{x}_{\text{aux}}\mathbf{x}_{\text{prim}}}$
Max SNR	$\mathbf{R}_c = \sigma^2_c\mathbf{a}_c\mathbf{a}^H_c$ $\mathbf{R}_{r+n} = \mathbf{A_r}\cdot\mathbf{R_r}\cdot\mathbf{A_r}^H + \mathbf{R_n}$	$x_{\text{clean}}(t) = \mathbf{w}^H_{\text{maxSNR}}\mathbf{x}(t)$	$\mathbf{R}^{-1}_{r+n}\mathbf{R}_c\mathbf{w}_{\text{maxSNR}} = \lambda_{\text{maxSNR}}\mathbf{w}_{\text{maxSNR}}$
LCMV	$\mathbf{R} = \mathbb{E}\{\mathbf{x}(t)\mathbf{x}^H(t)\}$	$x_{\text{clean}}(t) = \mathbf{w}^H_{\text{LCMV}}\mathbf{x}(t)$	$\mathbf{w}_{\text{LCMV}} = g\frac{1}{\mathbf{a}^H_c\mathbf{R}^{-1}\mathbf{a}_c}\mathbf{R}^{-1}\mathbf{a}_c$
Orthogonal projection	$\mathbf{P}^\perp = \mathbf{I} - \mathbf{a}_r(\mathbf{a}^H_r\mathbf{a}_r)^{-1}\mathbf{a}^H_r$	$x_{\text{clean}}(t) = \mathbf{w}^H_{\mathbf{P}^\perp}\mathbf{x}(t)$	$\mathbf{w}_{\mathbf{P}^\perp} = \mathbf{P}^\perp\mathbf{a}_c$
Oblique projection	$\mathbf{E}_{\mathbf{a}_c\mathbf{a}_r} = \mathbf{a}_c(\mathbf{a}^H_c\mathbf{P}^\perp_{\mathbf{A_r}}\mathbf{a}_c)^{-1}\mathbf{a}^H_c\mathbf{P}^\perp_{\mathbf{A_r}}$	$x_{\text{clean}}(t) = \mathbf{w}^H_{\mathbf{E}_{\mathbf{a}_c\mathbf{a}_r}}\mathbf{x}(t)$	$\mathbf{w}_{\mathbf{E}_{\mathbf{a}_c\mathbf{a}_r}} = \mathbf{E}^H\mathbf{a}_c$

Table 3.2: Summary of the different spatial filtering techniques presented in this chapter.

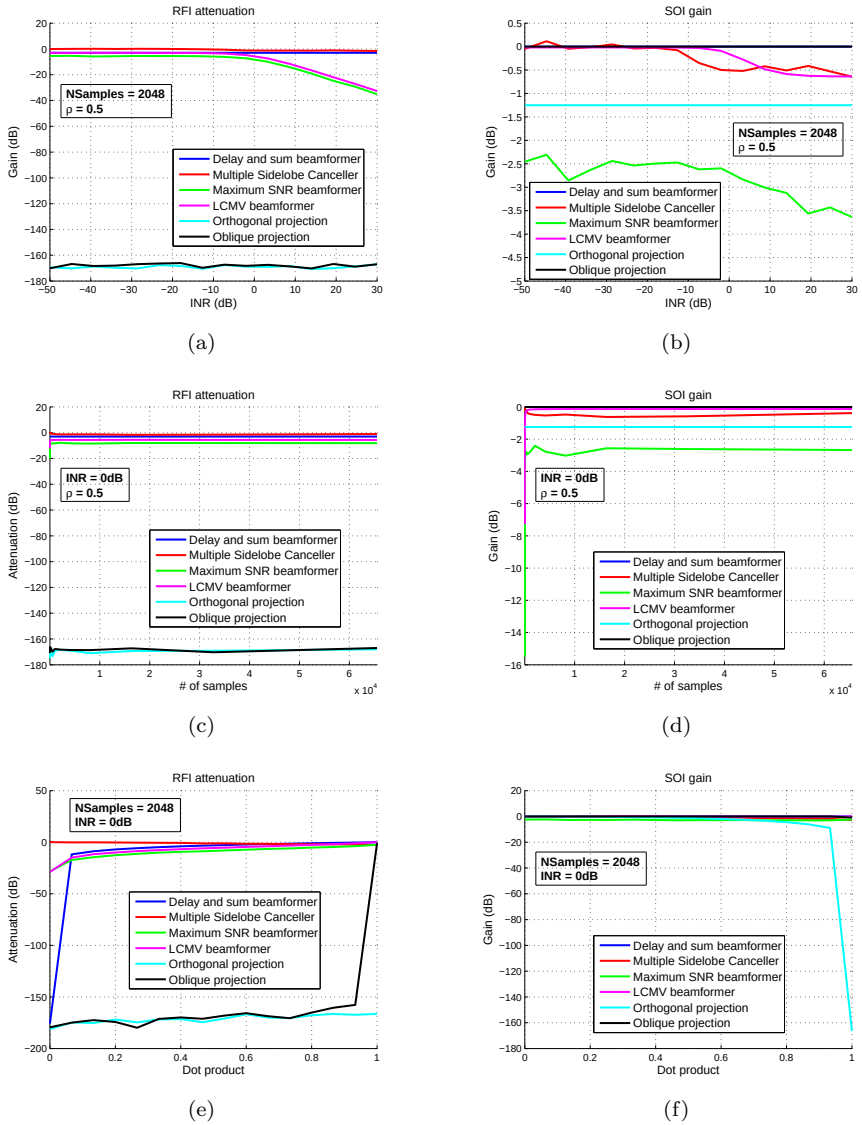

Figure 3.13: Spatial filtering techniques comparison. The spatial signatures $\mathbf{a}_c$ and $\mathbf{a}_r$ are here perfectly known. The simulated antenna array is a uniform linear 10-antenna array with $\frac{\lambda}{2}$ spacing. Each result was averaged over 256 trials. INR $= 10\log_{10}(\sigma_r^2/\sigma_n^2)$. SNR $= 10\log_{10}(\sigma_c^2/\sigma_n^2)$. (a) and (b) Respectively interference attenuation and direction of interest gain with varying Interference to Noise Ratio. Signals lengths : 2048 samples, dot product between $\mathbf{a}_c$ and $\mathbf{a}_r$: $\rho = 0.5$. (c) and (d) Respectively interference attenuation and direction of interest gain with varying signal lengths. INR = 0 dB, SNR = 0 dB, dot product between $\mathbf{a}_c$ and $\mathbf{a}_r$: $\rho = 0.5$. (e) and (f) Respectively interference attenuation and direction of interest gain with varying dot product between $\mathbf{a}_c$ and $\mathbf{a}_r$. Signal lengths : 2048 samples, INR = 0 dB, SNR = 0 dB.

Chapter 4

Interference subspace estimation

Most of the interference mitigation techniques, as seen in the previous chapter, require knowledge of the interference subspace. Their performances are highly correlated with the interference subspace estimation accuracy. Inaccurate estimations lead to astronomical data deterioration.

Each interference being defined by a steering vector, the set of steering vectors of all the interference signals $\mathbf{A_r}$ is a basis of the interference subspace. The whole data vector space can then be considered as a direct sum between an interference subspace, a cosmic source subspace and a noise subspace.

The previous chapter assumed that all spatial signatures of interference and cosmic sources were perfectly known. This chapter addresses their estimation.

A basic approach to estimate an interference steering vector would be a geometrical approach. The majority of jammers have a fixed location, or a predictable trajectory. The knowledge of the antenna array radio telescope location, as well as the jammer location and frequency, gives an accurate steering vector model of the interference considered. However, using this approach requires a perfectly calibrated antenna array. Any calibration error would also alter the spatial filtering performances.

Knowing each one of the RFI steering vectors is not required though. There is no unicity in a subspace basis, and another set of vectors contained in the initial data vector space, an orthogonal set for instance, can also span the same subspace as the one generated by $\mathbf{A_r}$.

Depending on the kind of data available (time series, covariance matrices, cyclic covariance matrices, etc), different techniques of interference subspace estimation can be chosen. In this chapter we present different techniques, each one being based on a particular type of covariance matrix, or a set of them.

4.1 Covariance matrices

It was seen in chapter 2 that different aspects of an antenna array radio telescope data model can lead to different covariance matrices. Even if only the classical covariance matrix is estimated at a radio telescope correlation stage, this chapter presents the advantages offered by other types of matrices.

4.1.1 Classical covariance matrix

We consider here the classical antenna array covariance matrix model defined in Equation 2.14. Without the multipath effect, and neglecting noise coupling, the matrices $\mathbf{R_c}$, $\mathbf{R_r}$ and $\mathbf{R_n}$, respectively the RFI, cosmic source and system noise covariance matrices, are diagonal. Interference signal powers are usually stronger than cosmic sources' powers. Typical Interference to Noise ratios are located between -70 dB up to $+50$ dB, whereas cosmic source powers are around 20 dB below the system noise level. Therefore, by neglecting the cosmic source contribution, this second-order data model can be rewritten as:

$$\mathbf{R} = \mathbf{R}_{RFI} + \mathbf{R_n} \tag{4.1}$$

with the interference-only covariance matrix defined by:

$$\mathbf{R}_{RFI} = \mathbf{A_r}\mathbf{R_r}{\mathbf{A_r}}^H \tag{4.2}$$

and has, by definition, a rank equal to N_r, the number of interference signals impinging the antenna array. Due to subband filtering, it is assumed that $N_r \leq M$. Applying an eigenvalue decomposition to $\mathbf{R}_{RFI}$ leads to:

$$\mathbf{R}_{RFI} = \mathbf{U}\mathbf{S}\mathbf{U}^H \tag{4.3}$$

with $\mathbf{S}$ a diagonal matrix containing the eigenvalues of $\mathbf{R}_{RFI}$ in its main diagonal and $\mathbf{U}$ a unitary matrix containing the column eigenvectors of $\mathbf{R}_{RFI}$ such that $\mathbf{U}\mathbf{U}^H = \mathbf{U}^H\mathbf{U} = \mathbf{I}$.

The rank of $\mathbf{R}_{RFI}$ being N_r, N_r eigenvalues are nonzero and $M - N_r$ eigenvalues equal zero. Assuming these eigenvalues are sorted in decreasing order, Equation 4.3 has the following structure:

$$\begin{aligned}\mathbf{R}_{RFI} &= \mathbf{U}\mathbf{S}\mathbf{U}^H \\ &= \begin{pmatrix}\mathbf{U_r} & \mathbf{U_n}\end{pmatrix}\begin{pmatrix}\mathbf{S_r} & \mathbf{0} \\ \mathbf{0} & \mathbf{0}\end{pmatrix}\begin{pmatrix}{\mathbf{U_r}}^H \\ {\mathbf{U_n}}^H\end{pmatrix}\end{aligned} \tag{4.4}$$

The diagonal submatrix $\mathbf{S_r}$ has a size $N_r \times N_r$ and contains the nonzero eigenvalues of $\mathbf{R}_{RFI}$ in its main diagonal. The column eigenvectors corresponding to these eigenvalues are stored in the $M \times N_r$ submatrix $\mathbf{U_r}$. Since $\mathbf{R}_{RFI}$ is hermitian, this vector set is an orthogonal basis of the interference subspace. Without further assumption, i.e. without orthogonality between the interference steering vectors and assuming $N_r > 1$, there is no direct link between these vectors and the different interference steering vectors. The $M \times (M - N_r)$ submatrix $\mathbf{U_n}$ is a basis of the kernel subspace of $\mathbf{R}_{RFI}$.

Consider now the covariance data model expressed in Equation 4.1. Assuming the antenna array is calibrated, $\mathbf{R_n}$ is a diagonal matrix containing equal elements in its main diagonal, i.e. $\mathbf{R_n} = \sigma_n^2\mathbf{I}$, with σ_n^2 the total noise power received on a single antenna [88, 65].

Any eigenvector of $\mathbf{R}_{RFI}$ is also an eigenvector of $\mathbf{R}$: Suppose λ_i is the i^{th} nonzero eigenvalue of $\mathbf{R}_{RFI}$, and $\mathbf{u}_i$ its corresponding eigenvector. Then we have:

$$\begin{aligned}\mathbf{R}\mathbf{u}_i &= (\mathbf{R}_{RFI} + \mathbf{R_n})\mathbf{u}_i \\ &= \mathbf{R}_{RFI}\mathbf{u}_i + \mathbf{R_n}\mathbf{u}_i \\ &= \lambda_i\mathbf{u}_i + \sigma_n^2\mathbf{u}_i \\ &= (\lambda_i + \sigma_n^2)\mathbf{u}_i \end{aligned} \tag{4.5}$$

The eigenvalue decomposition of $\mathbf{R}$ can then be written as:

$$\begin{aligned}\mathbf{R} &= \mathbf{U}\mathbf{S}_{noisy}\mathbf{U}^H \\ &= \begin{pmatrix}\mathbf{U_r} & \mathbf{U_n}\end{pmatrix}\begin{pmatrix}\mathbf{S_r} + \sigma_n^2\mathbf{I}_{N_r\times N_r} & \mathbf{0} \\ \mathbf{0} & \sigma_n^2\mathbf{I}_{(M-N_r)\times(M-N_r)}\end{pmatrix}\begin{pmatrix}\mathbf{U_r}^H \\ \mathbf{U_n}^H\end{pmatrix}\end{aligned} \tag{4.6}$$

with $\mathbf{I}_{N_r\times N_r}$ and $\mathbf{I}_{(M-N_r)\times(M-N_r)}$ respectively the $N_r \times N_r$ and the $(M - N_r) \times (M - N_r)$ identity matrices. An interference subspace basis can still be estimated. This basis will be made of the eigenvectors corresponding to the N_r non-constant eigenvalues of $\mathbf{R}$.

However, without a noise whitening process, the noise covariance matrix $\mathbf{R_n}$ can practically no longer be considered as diagonal, because of mutual coupling or a finite sample effect for instance, the noise subspace is distorted and non spatially white. Then, the eigenvalue decomposition cannot highlight an interference subspace basis anymore. In the same way, if the noise power is not constant over the antennas, an eigenvalue decomposition of the covariance matrix might also not highlight an interference subspace since there will not be constant eigenvalues.

Figure 4.1 depicts for instance the influence of the finite sample effect on the covariance matrix eigenvalues estimation [20]. In this simulation, 4 interference signals are assumed to impinge an antenna array made of $M = 20$ elements. The blue asterisks are the eigenvalues of a theoretical covariance matrix. Estimating this covariance matrix over 128 samples (red asterisks), 1024 samples (green asterisks) and 65536 samples (magenta asterisks), the matrices $\mathbf{R_r}$ and $\mathbf{R_n}$ are no longer diagonal and the retrieved interference and noise subspaces are only distorted estimates of the real ones.

Moreover, the classic eigenvalue decomposition technique is based on the assumption that cosmic sources have negligible power. If not, an eigenvalue decomposition of a covariance matrix estimate will only lead to a signal subspace basis estimate:

$$\mathbf{R} = \begin{pmatrix}\mathbf{A_r} & \mathbf{A_c}\end{pmatrix}\begin{pmatrix}\mathbf{R_r} & \mathbf{0} \\ \mathbf{0} & \mathbf{R_c}\end{pmatrix}\begin{pmatrix}\mathbf{A_r}^H \\ \mathbf{A_c}^H\end{pmatrix} + \mathbf{R_n} \tag{4.7}$$

The RFI and cosmic sources subspaces would no longer be distinguishable after applying an eigenvalue decomposition to $\mathbf{R}$ since those subspaces are not orthogonal. Therefore, the signal subspace would contain the contributions from both interference and cosmic sources. Retrieving an interference subspace basis estimate would be impossible. Moreover, a spatial filtering based on a signal subspace estimated through the classic eigenvalue decomposition would in this case suppress the interference and the cosmic sources.

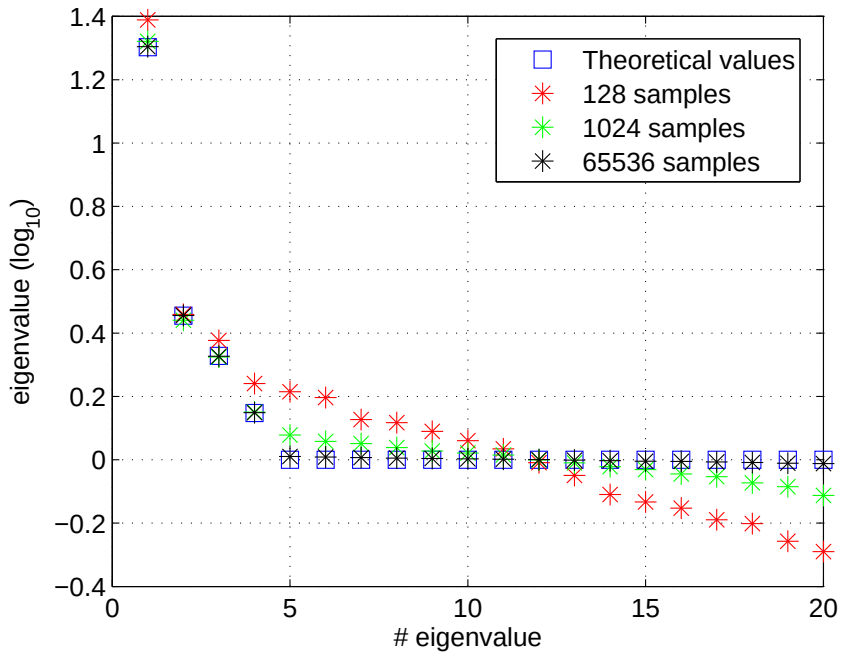

Figure 4.1: Classical covariance matrix eigenvalues estimates. Simulated data model involving 4 white Gaussian interference signals and a white Gaussian additive noise impinging a 20-element antenna array. Blue : theoretical eigenvalues. Red : eigenvalues estimated over 128 samples. Green : eigenvalues estimated over 1024 samples. Magenta : eigenvalues estimated over 65536 samples.

The INR can also lead to an inaccurate interference spatial signature estimation. The figure 4.2 shows an example of simulated data before and after projection with an interference subspace estimated with a classical covariance matrix SVD. The simulated radio telescope is a randomly distributed 48-antenna array. The data contain one single interference, modeled as a white Gaussian noise, and calibrated system noise modeled as white Gaussian noise with equal power on each receiver. The covariance matrix was estimated over 2048 samples. All skymaps are given in dB.

The figure 4.2.(a) shows a skymap corrupted with a strong interference (INR = +10 dB). The interference can easily be localized, as it corresponds to the strongest area on the map (highlighted by a magenta circle). After estimating the interference mono-dimensional subspace, an orthogonal projector is built and applied to the data. The resulting skymap can be seen on figure 4.2.(c). The figure 4.2.(b) shows the skymap corrupted with a much weaker interference (INR = −10 dB), located in the same area as in the figure 4.2.(a). The interference power is now lower than the noise power. Estimating the interference subspace using the strongest singular value of the classical covariance matrix leads to a wrong estimate. The figure 4.2.(d) shows the recovered data after applying an orthogonal projection with the interference subspace estimate. The projected data clearly do not correspond to the interference.

4.1.2 Cyclic covariance matrices

When cosmic sources cannot be neglected, the previous method does not differentiate between cosmic source and interference subspaces. Getting rid of the cosmic source and the system noise contributions improves the interference subspace estimation. The techniques described here are based on statistical properties that only interference signals present. As seen in section 2.4.2, most telecommunication signals are cyclostationary, unlike the system noise and cosmic sources (except for some pulsing radio sources). Knowing the *cyclic* or *conjugate cyclic* frequencies, by a priori knowledge or by estimation, leads to a *cyclic covariance matrix* calculation. Consider a cyclostationary interference $r_{\alpha_0}(t)$ at cyclic frequency α_0, $\alpha_0 \neq 0$, impinging an antenna array:

$$\mathbf{x}(t) = \mathbf{a_r} r_{\alpha_0}(t) + \mathbf{A_c} \cdot \mathbf{c}(t) + \mathbf{n}(t) \tag{4.8}$$

The α_0-cyclic covariance matrix of this data model is defined by:

$$\mathbf{R}^{\alpha_0} = {\sigma_r^{\alpha_0}}^2 \mathbf{a_r}{\mathbf{a_r}}^H + \mathbf{A_c}{\mathbf{R_c}}^{\alpha_0}{\mathbf{A_c}}^H + {\sigma_n^{\alpha_0}}^2 \mathbf{I} \tag{4.9}$$

$$= {\sigma_r^{\alpha_0}}^2 \mathbf{a_r}{\mathbf{a_r}}^H + \underbrace{\mathbf{R}_{cosmic}^{\alpha_0}}_{\to 0} + \underbrace{{\mathbf{R_n}}^{\alpha_0}}_{\to 0} \tag{4.10}$$

The cosmic sources and the system noise being stationary by nature, their cyclic contributions for a cyclic frequency $\alpha \neq 0$ are zero. Applying a singular value decomposition to $\mathbf{R}^{\alpha_0}$ leads to:

$$\mathbf{R}^{\alpha_0} \sim {\sigma_r^{\alpha_0}}^2 \mathbf{a_r}{\mathbf{a_r}}^H \tag{4.11}$$

$$= \mathbf{U}\mathbf{S}\mathbf{V}^H \tag{4.12}$$

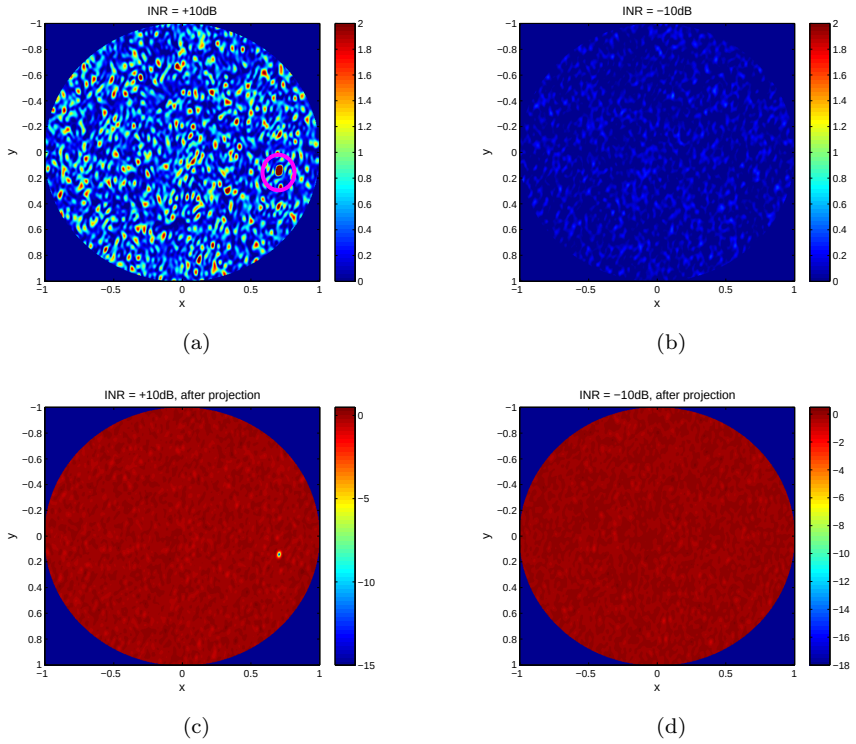

Figure 4.2: Impact of the INR with the classical covariance matrix SVD. Simulated randomly distributed 48-antenna array radio telescope, 1 RFI, covariance matrices estimated over 2048 samples. Skymaps are given in dB. (a) INR = +10 dB. (b) INR = −10 dB. (c) INR = +10 dB after orthogonal projection with interference subspace estimated with the classical covariance matrix SVD. (d) INR = −10 dB after orthogonal projection with interference subspace estimated with the classical covariance matrix SVD.

By construction, the matrix S is a diagonal matrix containing one nonzero singular value and $M-1$ zero singular values of $\mathbf{R}^{\alpha_0}$. By definition, the nonzero singular value is related to the α_0-cyclostationary interference, and its corresponding singular vector is an estimate of the interference steering vector:

$$\mathbf{u_1} = \mathbf{v_1} = \hat{\mathbf{a}}_\mathbf{r} \tag{4.13}$$

with $\mathbf{u_1}$ the first column vector of the matrix $\mathbf{U}$ and $\mathbf{v_1}$ the first column vector of the matrix $\mathbf{V}$ if the singular values of $\mathbf{R}^{\alpha_0}$ in $\mathbf{S}$ are sorted in decreasing order.

If more than one interference impinge the antenna array, they are unlikely to share the same cyclic frequency. Therefore, the cyclic covariance calculated regarding one particular cyclic frequency α_0 is more likely a rank-1 matrix. The advantage of this technique is that interference steering vectors are estimated one at a time, and it allows the filtering of one particular interference or the nulling of one particular 1-dimensional subspace of the data vector space.

Figure 4.3.(a) shows a simulated skymap where two pure carrier signals are impinging an antenna array at the horizon. Their frequencies are respectively $f_1 = 0.1$ and $f_2 = 0.25$. Figure 4.3.(b) is the conjugate cyclic power spectrum acquired on a single antenna. Three peaks can clearly be seen at the conjugate cyclic frequencies $\alpha_1 = 0.2$ ($\alpha_1 = 2 \times f_1$) and $\alpha_2 = 0.5$ ($\alpha_2 = 2 \times f_2$). The third peak is an intermodulation product effect at cyclic frequency $\alpha_3 = 0.35$ ($f_1 + f_2$). Applying a singular value decomposition on both conjugate cyclic covariance matrices at α_1 and α_2 allows us to estimate separately the steering vectors (and therefore the directions of arrival) for each interference independently (figure 4.3.(c) and 4.3.(d)).

If more than one cyclostationary interference share the same cyclic frequency, then the cyclic covariance matrix calculated at their cyclic frequency will have a rank greater than one. This rank, given by the amount of nonzero singular values, indicates the number of cyclostationary interferences impinging the array and sharing the same cyclic frequency. The singular vectors corresponding to the non zero singular values of the matrix form then an orthogonal basis spanning the same subspace as the one generated by the basis made of all the individual α_0-cyclostationary RFI.

The cyclic singular value decomposition technique is an efficient way of estimating an interference subspace by attenuating the cosmic source and the system noise contributions. However, this technique requires knowledge of the cyclostationary interference cyclic frequencies. If not, it would require estimating them by calculating a cyclic spectrum based on the antenna array output data. The technique is also computationally expensive : a cyclic covariance matrix has to be calculated for each interference at different cyclic frequencies. However, this issue can be solved by efficiently sharing the central correlator resources.

4.1.3 Time-lagged covariance matrices

Cosmic source and system noise signals are usually assimilated as stochastic processes, unlike interference signals [105]. Most of them are constructed following modulation schemes, and become therefore deterministic processes. A major difference between stochastic and deterministic processes is the autocorrelation

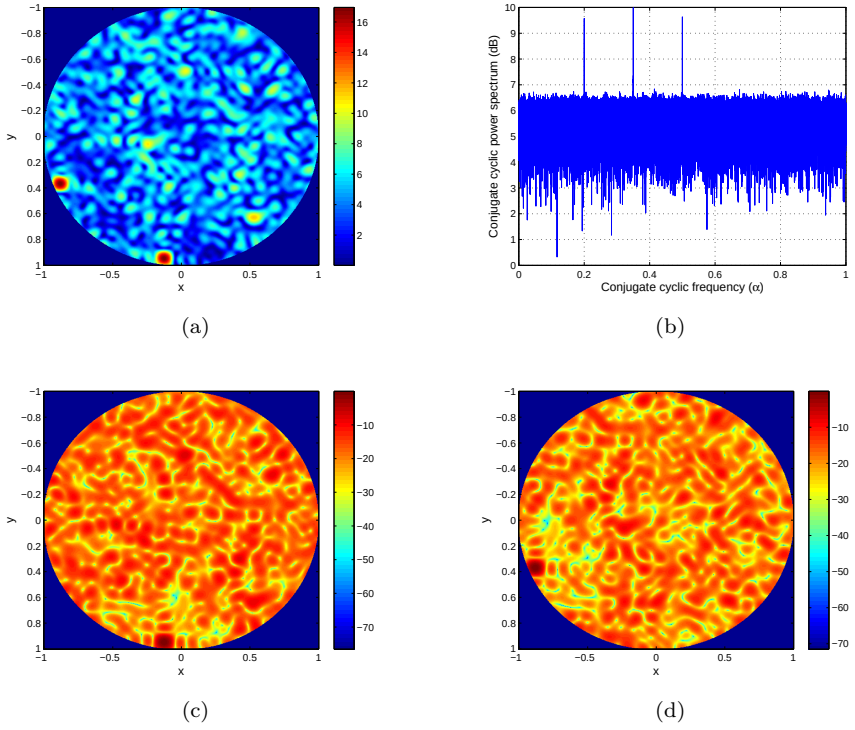

Figure 4.3: Cyclic singular value decomposition interference subspace estimation. All figures given in dB. (a) Simulated skymap with two cyclostationary interferences (48-antenna array, $INR_1 = 0dB$, $INR_2 = 0dB$) (b) Conjugate cyclic spectrum of acquired data. Three peaks can be seen at $\alpha_1 = 0.2$, $\alpha_1 = 0.5$ and $\alpha_1 = 0.35$. The cyclic power at α_3 is an intermodulation product effect. (c) Interference subspace estimate using a conjugate cyclic covariance matrix calculated at α_1. (d) Interference subspace estimate using a conjugate cyclic covariance matrix calculated at α_2.

function. The autocorrelation of a white signal is null for any time-lag $\tau \neq 0$, whereas the autocorrelation of a deterministic process allows retrieval of particular signal features, such as hidden periodicities or noisiness quantification. For example, figure 4.4.(c) compares the autocorrelation of a simulated cosmic source signal (modeled as a white Gaussian noise) in red and a simulated Binary Phase Shift Keying modulated signal. Information about the interference is still available for a time-kag $\tau \neq 0$, while the cosmic source autocorrelation is zero. This effect is also clearly seen on skymaps 4.4.(a) and 4.4.(b), computed using a zero-sample time-lag and a one-sample time-lag respectively.

Calculating a covariance matrix at the output of an antenna array for any time-lag $\tau_0 \neq 0$ asymptotically removes the contribution of cosmic sources and system noise:

$$\begin{aligned} \mathbf{R}(t,\tau_0) &= \mathbf{A_c} \underbrace{\mathbf{R_c}(t,\tau_0)}_{\to \mathbf{0}} \mathbf{A_c}^H + \mathbf{A_r}\mathbf{R_r}(t,\tau_0)\mathbf{A_r}^H + \underbrace{\mathbf{R_n}(t,\tau_0)}_{\to \mathbf{0}} \\ &\sim \mathbf{A_r}\mathbf{R_r}(t,\tau_0)\mathbf{A_r}^H \end{aligned} \tag{4.14}$$

If the multipath effect is neglected, the matrix $\mathbf{R_r}(t,\tau_0)$ is diagonal and by applying a singular value decomposition to the covariance matrix $\mathbf{R}(t,\tau_0)$, in the same way as for the cyclic singular valued decomposition, an RFI subspace basis could be estimated.

However, determining the dimension of the interference subspace (i.e. the amount of interference signals impinging the radio telescope) is not trivial with a time-lag approach. Indeed, the autocovariance function $\Gamma_r(t,\tau)$ of an interference signal $r(t)$ is not necessarily nonzero for any time-lag τ. Therefore, the use of only one covariance matrix, calculated for a time-lag $\tau_0 \neq 0$, might not be enough to estimate the whole interference subspace, depending on the nature of the interference signals.

4.1.4 Single matrix performance analysis

To compare the performance of the different signature vector estimation techniques, we ran a simulation involving a pure carrier RFI added to white Gaussian noise (random normalized carrier frequency f_0). An array composed of $M = 48$ antennas was used. The array noise was calibrated in a first scenario, and uncalibrated with 20% noise power fluctuations over antennas in a second scenario. The estimation techniques are given with regard to the INR when no other (cosmic) source impinges the radio telescope, and with regard to the Interference to Signal Ratio (ISR) when a cosmic source impinges the antenna array at the same time as an RFI (SNR = 0 dB). During each run, we generated a new data set (48 antennas $\times$ 2048 samples), estimated the signature vector of the impinging RFI and calculated the dot product between this estimate and the actual steering vector. In other words, the dot product defines here a measure of how the estimation matches the true signature vector. The INR and the ISR of the data vary from -25 dB to $+10$ dB. All our results were averaged over 100 runs for a fixed INR to provide statistics on signature vector estimation technique performances.

We calculate for each run a classical covariance matrix $\mathbf{R}$, a conjugate cyclic covariance matrix $\mathbf{R}^{\alpha_0}$, with $\alpha_0 = 2.f_0$, and a time-lagged covariance matrix

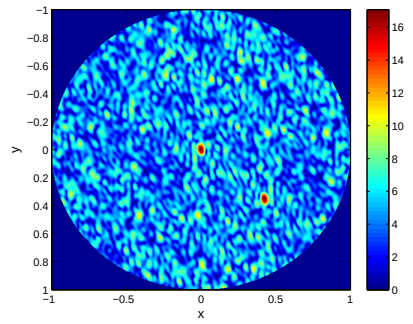

(a)

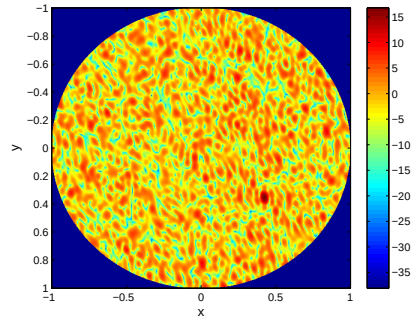

(b)

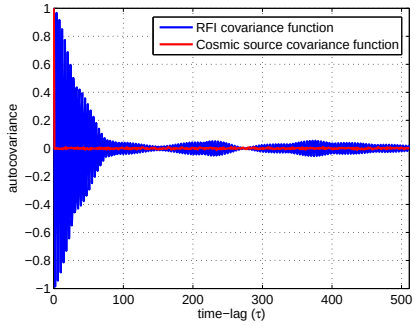

(c)

Figure 4.4: Time-lag approach. Skymaps given in dB. (a) Simulated skymap containing one cosmic source at the zenith (center of the map) and a Binary Phase Shift Keying modulated interference located closer to the horizon (48-antenna array, $SNR = 0dB$, $INR = 0dB$). (b) Skymap made out of a one sample time-lagged covariance matrix. Although the interference power is weaker on skymap (b) than (a), the interference remains while the cosmic source contribution disappears. (c) Comparison between the interference and the cosmic source covariance functions.

$R(\tau_0)$ with $\tau_0 = 1$ sample. The interference spatial signature estimation technique is based on the SVD of each of these matrices.

The figure 4.5 shows the performance results. As expected, the cyclic and the time-lag approaches are not sensitive to the antenna array uncalibration (same results on figures 4.5.(a) and 4.5.(b)). The performance of the classical covariance matrix diagonalization is lower with an uncalibrated array. However, with a perfect calibration, its performance is similar to the two other approaches as long as only one signal impinges the antenna array.

When more than one signal impinge the radio telescope, the classical covariance approach requires high INR and ISR to provide an accurate interference spatial signature estimation. Concerning the cyclic and the time-lag approaches, their performances are absolutely not perturbed by the presence of another interference. The dot product between the estimate and the actual interference spatial signatures reaches $\rho = 0.9$ with INR ≈ -4 dB with one single signal impinging the array, while it reaches the same value with ISR + SNR $\approx -13 + 10 = -3$ dB. The INR is therefore a dominant parameter for these techniques.

The next section addresses the concept of joint matrices approaches. The main idea behind these approaches is to consider more information than what is provided by a single covariance matrix.

4.2 Multiple matrices approaches

Covariance matrices provide theoretically all the information required to estimate an interference subspace. However, their estimate can, in practice, lead to inaccurate estimations. Based on multiple covariance matrices, the techniques presented in this section provide better interference subspace estimates. Even if the computational cost inevitably increases, the contributions of these techniques to spatial RFI mitigation has to be seriously considered.

4.2.1 Mean covariance matrix diagonalization

The principle of this technique is to calculate a mean matrix over all the cyclic and conjugated cyclic covariance matrices. As all these correlation matrices are biased by the added system noise and by the signal finite length over which they are estimated, computing a mean matrix will improve correlation matrix estimation.

Since all these matrices are defined on the same vector space (observation space), diagonalization of the mean matrix should provide a better estimate of the RFI spatial signature vector. Two options can be considered : applying an SVD of a mean cyclic correlation matrix or an EVD of a mean matrix calculated over cyclic correlation matrices after applying the transformation presented in equation 4.19 on each of them. It is however important to normalize matrices before any average calculation step, since cyclic power is not uniformly distributed over all the cyclic frequencies of a cyclostationary signal. We therefore divide each cyclic correlation matrix (or transformed cyclic correlation matrix) by its squared Frobenius Norm.

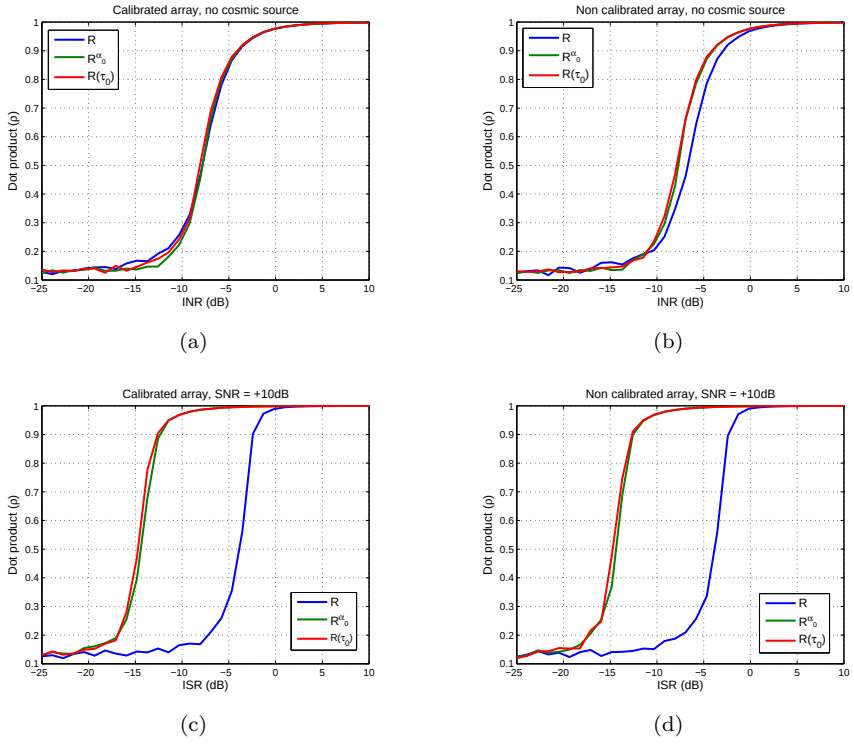

Figure 4.5: Performance comparison of single covariance matrix spatial signature vector estimation techniques (dot product between estimated and generated signature vectors for different techniques and different INR, its value is 1 for an exact estimation). (a) 48-antenna calibrated array, INR varying, no cosmic source. (b) 48-antenna uncalibrated array (20% noise power fluctuation over antennas), INR varying, no cosmic source. (c) 48-antenna calibrated array, SNR = +10 dB, ISR varying. (d) 48-antenna uncalibrated array (20% noise power fluctuation over antennas), SNR = +10 dB, ISR varying.

4.2.2 Joint SVD of time-lagged covariance matrices

To avoid the loss of information using a single time-lagged covariance matrix, one alternative is to use multiple matrices calculated with different time lags. The singular value decomposition can be applied to a non-squared matrix. By stacking these matrices in a single extended covariance matrix, the decomposition might be more accurate since it would take into account much more information than a single covariance matrix:

Consider $\tilde{\mathbf{R}}(t,\tilde{\tau}) = \begin{bmatrix}\mathbf{R}(t,\tau_0) & \mathbf{R}(t,\tau_1) & \mathbf{R}(t,\tau_2)\end{bmatrix}$, with $\tau_0 \neq \tau_1 \neq \tau_2 \neq 0$. The left singular vectors of $\tilde{\mathbf{R}}(t,\tilde{\tau})$ are the eigen vectors of the matrix $\tilde{\mathbf{R}}(t,\tilde{\tau})\tilde{\mathbf{R}}(t,\tilde{\tau})^H$, expressed by:

$$\tilde{\mathbf{R}}(t,\tilde{\tau})\tilde{\mathbf{R}}(t,\tilde{\tau})^H = \left[\mathbf{R}(t,\tau_0)\mathbf{R}(t,\tau_0)^H + \mathbf{R}(t,\tau_1)\mathbf{R}(t,\tau_1)^H + \mathbf{R}(t,\tau_2)\mathbf{R}(t,\tau_2)^H\right] \tag{4.15}$$

These eigen vectors can therefore be seen as eigen vectors common to $\mathbf{R}(t,\tau_0)$, $\mathbf{R}(t,\tau_1)$, $\mathbf{R}(t,\tau_2)$. The interference subspace basis estimate given by this approach will then be more accurate.

Figure 4.6 shows simulations with synthetic data ($M = 48$ antennas, three white Gaussian cosmic sources and three BPSK RFI). The INR is $-6dB$. Consequently, the RFI are barely visible as can be seen on figure 4.6.(a). The expected RFI subspace is represented on figure 4.6.b). The RFI subspace is estimated with the proposed approach by using respectively $N = 1$ and $N = 9$ different time-lags (a single sample time-lag and nine covariance matrices calculated from $\tau = 1.T_s$ to $\tau = 9.T_s$, with T_s the sampling period). Figure 4.6.c) and d) show the RFI subspace estimation (SE) error relative to the expected RFI subspace (i.e. difference between estimated $\widehat{\mathbf{A}_\mathbf{r}}.\widehat{\mathbf{A}_\mathbf{r}}^H$ and the true $\mathbf{A}_\mathbf{r}.\mathbf{A}_\mathbf{r}{}^H$). In both simulations, the RFI subspace can be retrieved but the stacked approach provides smaller SE errors in the skymap.

As a comparison between the cyclostationary and the time lag approaches, figure 4.7 again shows simulations with synthetic data similar to figure 4.6. To obtain sufficient cyclostationary information, the INR was set to 0 dB. The RFI positions have also changed (see Figure 4.7.a). The ability of the algorithm to extract one specific RFI subspace is shown on figure 4.7.b). A cyclic frequency corresponding to the selected RFI is chosen (in our case, 2 times the carrier frequency). The corresponding conjugated cyclic covariance matrix is calculated. Then, the SVD provides a spatial signature estimation of only the selected RFI. To define the whole RFI subspace, the previous procedure is applied 3 times for 3 different cyclic frequencies. Figure 4.7.d) shows the RFI SE error relative to the expected RFI subspace. For comparison, the time lag approach with $N = 1$ sample time lag is given on figure 4.7.c). With this INR, the cyclic approach produces a larger SE error than the time-lag approach, but the counterpart is the capability to extract each individual RFI.

4.2.3 Joint diagonalization

The purpose of this section is to use all the statistical information included in the different time-lagged correlation matrices by jointly diagonalizing them in order to improve the interference subspace estimation accuracy. Different algorithms allowing a joint-diagonalization of a set of matrices can be found

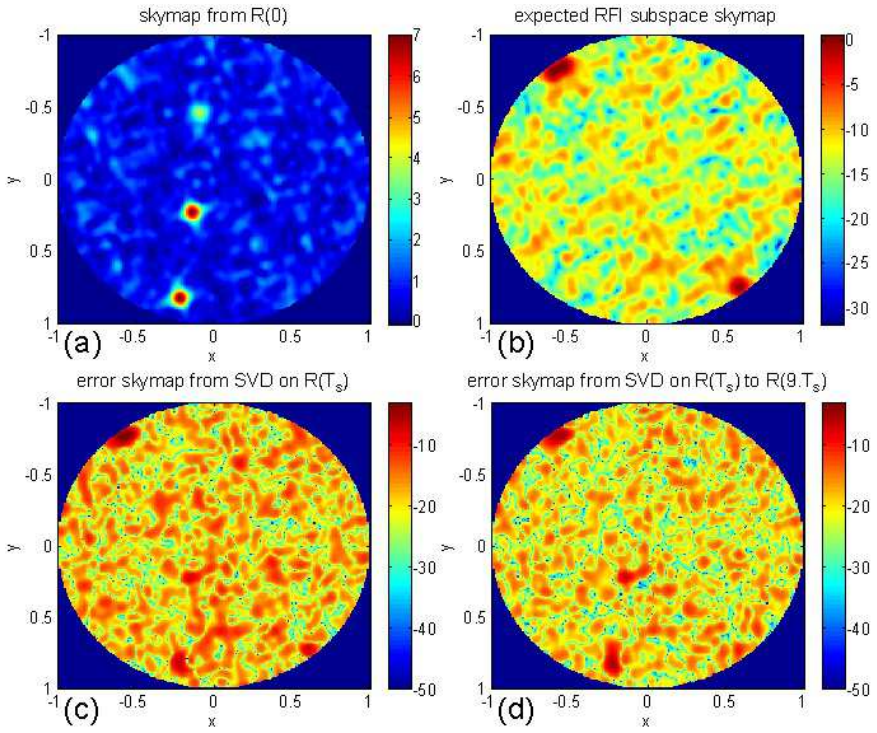

Figure 4.6: Extended time-lag approach. (a) Simulated skymap with 3 white Gaussian cosmic sources and 3 BPSK RFI (INR $= -6dB$). (b) Expected RFI subspace built with the three real RFI steering vectors. (c) Error skymap between the expected RFI subspace and the RFI subspace retrieved with the time lag approach (one sample time lag). (d) Skymap error between the expected RFI subspace and the RFI subspace retrieved using the extended time lag approach (one extended covariance matrix made of nine time lagged covariance matrices, from $\tau = 1.T_s$ sample to $\tau = 9.T_s$ samples, with T_s the sampling period)

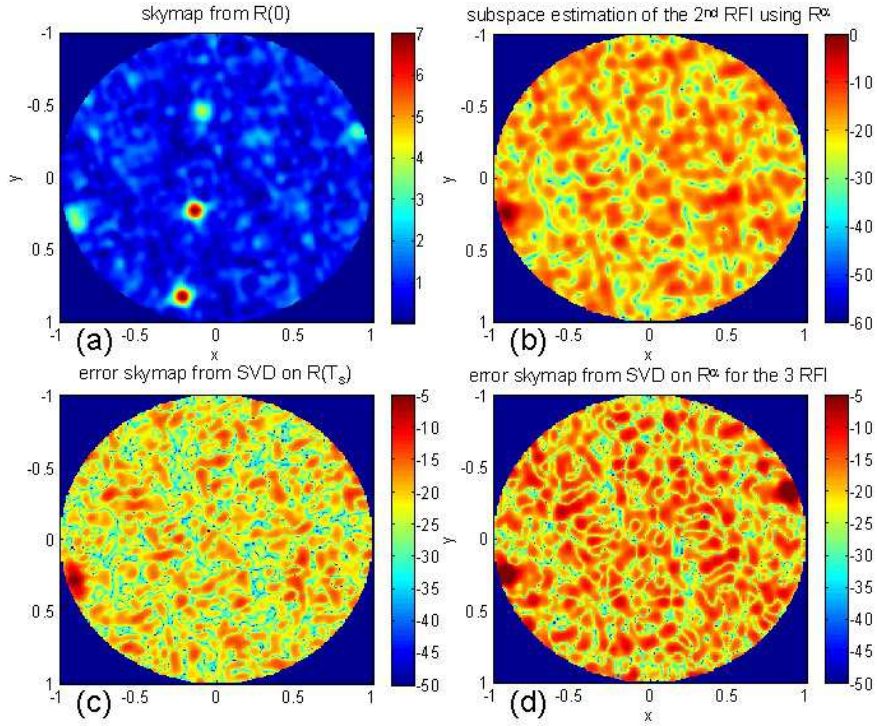

Figure 4.7: Comparison between the cyclostationary and the time lag approaches. (a) Simulated skymap with 3 white Gaussian cosmic sources and 3 BPSK RFI (INR = $0dB$). (b) Single interference subspace estimated using one cyclic covariance matrix calculated at its cyclic frequency. (c) Error skymap between the expected RFI subspace and the one retrieved using a single sample time lagged covariance matrix. (d) Error skymap between the expected RFI subspace and the one retrieved using 3 cyclic covariance matrices calculated for three different cyclic frequencies corresponding to the three cyclostationary interferences.

in the literature [57, 107, 39, 94]. Two joint diagonalization approaches are presented here : the *off function approach* and the *Alternating Least Squares approach*.

off function approach

The basic idea of joint diagonalization is to find a common transformation matrix that allows the diagonalization of a set of matrices. Most cyclostationary interferences present more than one cyclic frequency. In order to provide a better estimate of the RFI signature vector, we suggest applying a joint diagonalization to cyclic matrices calculated at different cyclic frequencies, since all these matrices contain the same spatial information. Finding a joint diagonalizer for these matrices should therefore decrease the error made by a single matrix diagonalization due to the finite length correlation estimation.

In [14], Belouchrani et al. introduce the following *off* function for an $n \times n$ matrix $\mathbf{M}$ with entries M_{ij}:

$$off(\mathbf{M}) = \sum_{1 \leq i \neq j \leq n} |M_{ij}|^2 \tag{4.16}$$

By using this function, diagonalizing a matrix consists in finding a matrix $\mathbf{P}$, with size $n \times n$, such that:

$$off(\mathbf{P}^H \mathbf{M} \mathbf{P}) = 0 \tag{4.17}$$

The aim of joint diagonalization of a set of N matrices $\mathcal{M} = \{\mathbf{M_1}, \mathbf{M_2} ... \mathbf{M_k}\}$ is thus to find a matrix $\mathbf{P}$ that minimizes the following cost function:

$$c(\mathcal{M}, \mathbf{P}) = \sum_{k=1}^{N} off(\mathbf{P}^H \mathbf{M}_k \mathbf{P}) \tag{4.18}$$

As explained in [14], the optimization algorithm is based on the computation of Givens rotations. The joint-diagonalizer is then defined as a product of these rotation matrices [45].

Let $\mathcal{M}$ be a set of cyclic correlation matrices $\mathbf{R}^\alpha$ calculated over several cyclic and conjugated cyclic frequencies. The cyclic covariance matrices are usually decomposed following their singular values and vectors. The following property links the singular value decomposition to the eigen value decomposition.

$$\begin{aligned} \mathbf{R}^\alpha . \mathbf{R}^{\alpha H} &= (\mathbf{U}.\mathbf{S}.\mathbf{V}^H).(\mathbf{U}.\mathbf{S}.\mathbf{V}^H)^H \\ &= \mathbf{U}.\mathbf{S}.\mathbf{V}^H.\mathbf{V}.\mathbf{S}^H.\mathbf{U}^H \\ &= \mathbf{U}.\mathbf{S}.\mathbf{S}^H.\mathbf{U}^H \\ &= \mathbf{P}.\mathbf{D}.\mathbf{P}^H \end{aligned} \tag{4.19}$$

with $\mathbf{R}^\alpha = (\mathbf{U}.\mathbf{S}.\mathbf{V}^H)$ (SVD of $\mathbf{R}^\alpha$), $\mathbf{P} = \mathbf{U}$ and $\mathbf{D} = \mathbf{S}.\mathbf{S}^H$. By applying this property to all the matrices stored in $\mathcal{M}$, the RFI spatial signature vector can be estimated by finding a joint diagonalizer of $\mathcal{M}$.

The main advantage of this method is the use of multiple covariance matrices, thereby improving the estimation of the RFI signature vector. Although this advantage is important for the estimation accuracy, the implementation cost of

this method might increase with the chosen optimization algorithm. The next section will present a simpler multiple matrix technique.

Alternating Least Squares approach

Thanks to a collaboration with the Université de Sud Toulon-Var, the approach proposed here is based on the use of an iterative Alternating Least Squares (ALS) algorithm, presented, for example, in [28]. The idea can be expressed by defining a set of correlation matrices for N time lagged covariance matrices, using equation 4.14:

$$\begin{cases} \mathbf{R}(\tau_1) & \cong \mathbf{A_r}\mathbf{R_r}(\tau_1){\mathbf{A_r}}^H \\ & \vdots \\ \mathbf{R}(\tau_N) & \cong \mathbf{A_r}\mathbf{R_r}(\tau_N){\mathbf{A_r}}^H \end{cases} \tag{4.20}$$

Given this set, it is a well-known joint diagonalization problem. The goal is to recursively estimate $\mathbf{A_r}$ and $\mathbf{R_r}(\tau_i)$. Following [92], we now briefly describe the algorithm.

Update of $\mathbf{R_r}(\tau_i)$

The idea is to stack all the columns of the matrices defined in (4.20). Adapted to our problem, it leads to:

$$\begin{aligned} \mathbf{r}(\tau_i) &= [\mathrm{vec}(\mathbf{R}(\tau_1)), \ldots, \mathrm{vec}(\mathbf{R}(\tau_N))] \\ \mathbf{dR_r}(\tau_i) &= [\mathrm{diag}(\mathbf{R_r}(\tau_1)), \ldots, \mathrm{diag}(\mathbf{R_r}(\tau_N))] \\ \mathbf{r}(\tau_i) &= (\mathbf{A_r}^* \circ \mathbf{A_r})\, \mathbf{dR_r}(\tau_i) \end{aligned} \tag{4.21}$$

We can deduce the set $\mathbf{R_r}(\tau_i)$ from (4.21):

$$\mathbf{R_r}(\tau_i) = \mathrm{undiag}\left((\mathbf{A_r}^* \circ \mathbf{A_r})^\dagger \mathbf{r}(\tau_i)\right) \tag{4.22}$$

Update of $\mathbf{A_r}$

When all the $\mathbf{R_r}(\tau_i)$ have been estimated, the next step is to estimate $\mathbf{A_r}$. By concatenating horizontally all the matrices of the set, we notice that $\mathbf{A_r}$ is postmultiplied by the concatenation of two matrices. It can be written as:

$$\begin{aligned} \mathbf{R}(\tau_i) &= \mathbf{A_r}[\mathbf{R_r}(\tau_1){\mathbf{A_r}}^H, \ldots, \mathbf{R_r}(\tau_N){\mathbf{A_r}}^H] \\ \mathbf{R}(\tau_i) &= [\mathbf{R}(\tau_1), \ldots, \mathbf{R}(\tau_N)] \end{aligned} \tag{4.23}$$

Finally, we easily find $\mathbf{A_r}$:

$$\mathbf{A_r} = \mathbf{R}(\tau_i)[\mathbf{R_r}(\tau_1){\mathbf{A_r}}^H, \ldots, \mathbf{R_r}(\tau_N){\mathbf{A_r}}^H]^\dagger \tag{4.24}$$

These steps are repeated recursively until convergence is reached.

Figure 4.8 shows simulations with synthetic data similar to the previous section, but $N = 9$ time-lags are stacked this time. The capacity of the algorithm to extract one specific RFI subspace is shown in Figure 4.8.a. Figure 4.8.b shows the RFI SE error relative to the expected whole RFI subspace. For comparison, the RFI SE error for a time-lag approach with the same set of $N = 9$ matrices is given in Figure 4.8.c. The ALS approach provides both a smaller error and an indivual RFI extraction capability compared to the time-lag approach.

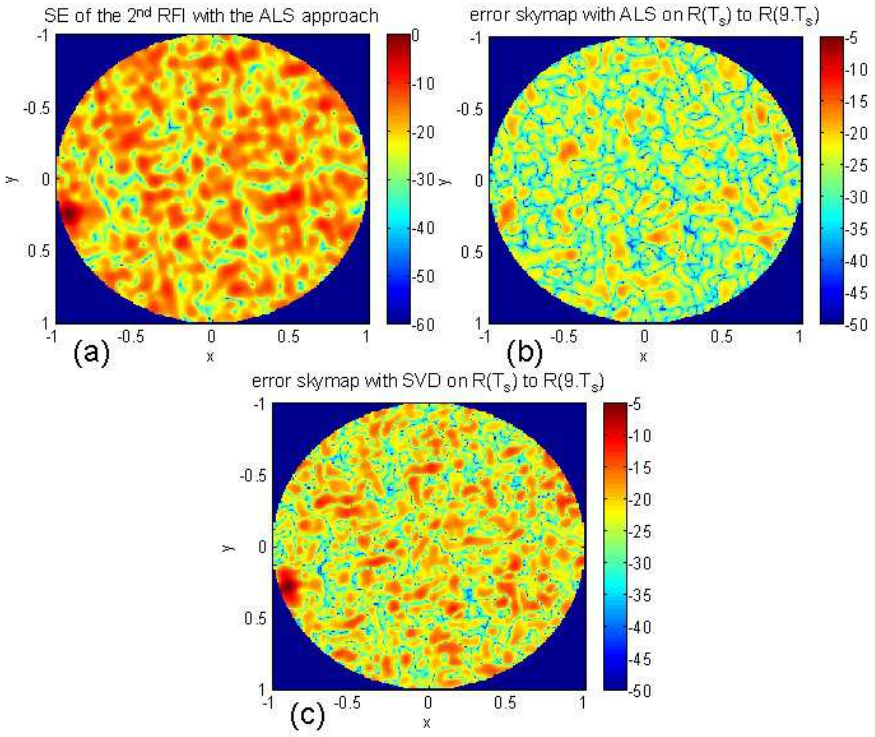

Figure 4.8: ALS Approach on a set of $N = 9$ time-lagged covariance matrices. Skymaps given in dB. (a) Estimated subspace sky map of 1 RFI obtained by selecting the right conjugated cyclic frequency corresponding to this RFI (here, 2 times its carrier frequency). (b) Sky map of RFI SE error obtained with the ALS approach. (c) For comparison, sky map of RFI SE error obtained from the SVD of the same set of matrices.

4.2.4 Multiple matrices performance analysis

The proposed methods were compared through Monte-Carlo based simulations. The data model used in these simulations involves one BPSK interference, with uniformly distributed over $[0.1 \dots 1]$ random normalized carrier frequency f_0 and uniformly distributed over $[\frac{1}{50} \dots \frac{1}{10}]$ baud rate (BR_0). The performances were evaluated according to the INR in a single signal scenario (RFI only) and the ISR in a 2-signal scenario (white Gaussian noise simulating a cosmic source).

Moreover, the antenna array calibration was also considered by simulating a perfectly calibrated array and an uncalibrated array with 20% noise fluctuation over the antennas.

The simulated radio telescope is a randomly distributed 48-antenna array. The performances, averaged over 100 trials, were evaluated according to the dot product ρ between the estimated and the actual interference spatial signature vectors ($\rho = 1$ corresponds to a perfect estimation).

6 different covariance matrices are estimated at each trial over 2048 samples:

- R^{α_0}, conjugate cyclic matrix with $\alpha_0 = 2.f_0$,
- R^{α_1}, conjugate cyclic matrix with $\alpha_1 = 2.f_0 + \mathrm{BR}_0$,
- R^{α_2}, conjugate cyclic matrix with $\alpha_2 = 2.f_0 - \mathrm{BR}_0$,
- $R(\tau_0)$, time-lagged covariance matrix with $\tau_0 = 1$ sample time-lag,
- $R(\tau_1)$, time-lagged covariance matrix with $\tau_1 = 2$ samples time-lag,
- $R(\tau_2)$, time-lagged covariance matrix with $\tau_2 = 3$ samples time-lag

The different estimation techniques (ET) evaluated are:

- ET1 : Diagonalization of R^{α_0},
- ET2 : Diagonalization of $R(\tau_0)$,
- ET3 : Joint SVD of $R(\tau_0)$, $R(\tau_1)$ and $R(\tau_2)$,
- ET4 : Joint SVD of R^{α_0}, R^{α_1} and R^{α_2},
- ET5 : Mean matrix diagonalization of $R(\tau_0)$, $R(\tau_1)$ and $R(\tau_2)$,
- ET6 : Mean matrix diagonalization of R^{α_0}, R^{α_1} and R^{α_2},
- ET7 : ALS-based joint-diagonalization of $R(\tau_0)$, $R(\tau_1)$ and $R(\tau_2)$,
- ET8 : ALS-based joint-diagonalization of R^{α_0}, R^{α_1} and R^{α_2}

The performance analysis results are given in figure 4.9. The calibration and the number of sources impinging the antenna array radio telescope do not affect the performances of the different techniques. This result was expected, since the covariance matrices chosen for applying the different approaches eliminate other (white or non-cyclostationary or cyclostationary with different cyclic frequencies) source contributions, as well as the system noise contribution.

The ET 6 and 8, based on conjugate cyclic matrices, have the poorest performances, while ET 7 and 3 give the best. Multiple time-lagged covariance

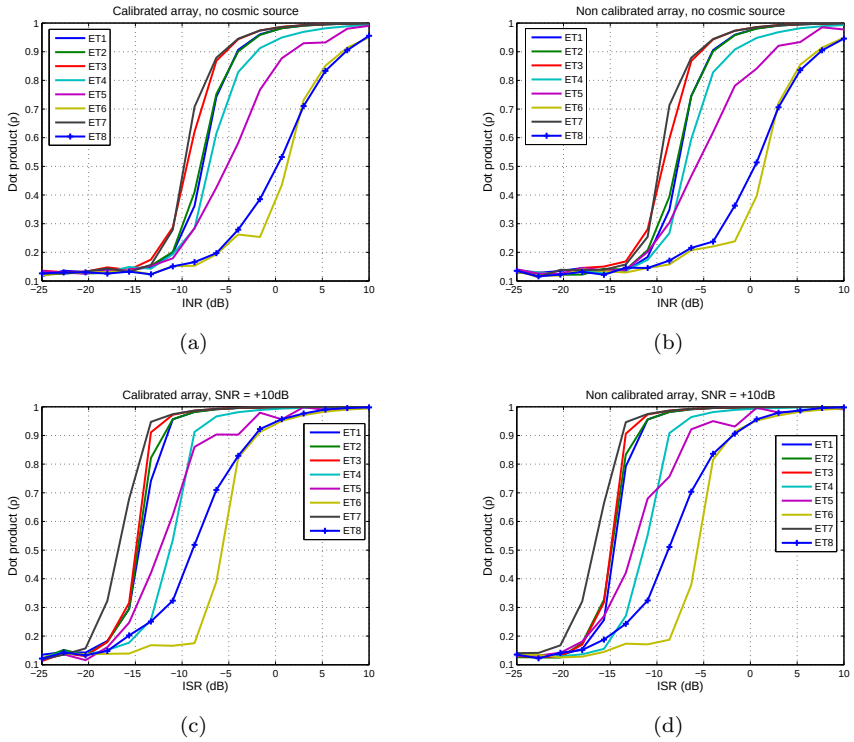

Figure 4.9: Performance comparison of multiple covariance matrices spatial signature vector estimation techniques (dot product between estimated and generated signature vectors for different techniques and different INR, its value is 1 for an exact estimation). (a) 48-antenna calibrated array, INR varying, no cosmic source. (b) 48-antenna uncalibrated array (20% noise power fluctuation over antennas), INR varying, no cosmic source. (c) 48-antenna calibrated array, SNR = +10 dB, ISR varying. (d) 48-antenna uncalibrated array (20% noise power fluctuation over antennas), SNR = +10 dB, ISR varying.

matrices remain therefore the best choice for applying a spatial interference mitigation algorithm on an uncalibrated antenna array radio telescope with an unknown number of sources when the (non-white) interference spatial signatures have to be estimated.

The different interference subspace estimation techniques presented previously are based on the diagonalization, or joint-diagonalization, of a particular type of covariance matrices. These techniques allow the estimation of an RFI subspace orthogonal basis, or an RFI steering vector when only one interference impinges the antenna array. Another set of techniques, known as *high resolution methods*, can also be used in order to recover the individual interference steering vectors. These methods are based on the optimization of a contrast function allowing the estimation of the interference direction of arrival, and, by extension, of their steering vectors. Even if they are unsuitable for use on phased antenna array radio telescopes, mostly because of the highly accurate calibration requirement, we decided to incorporate in this chapter two popular high resolution methods : *MUSIC* and *MVDR*.

4.3 Optimization-based techniques

Different interference subspace estimation techniques have been developed in recent years. They are usually based on estimation of the Signal-Of-Interest's direction of arrival. Once this direction has been estimated, a perfectly calibrated antenna array would lead to the desired interference steering vector estimation since the relationship between direction of arrival and steering vector is then bijective. We present here two algorithms, *MUSIC* and *MVDR*, that are based on a contrast function. This contrast function, associated with an optimization algorithm, enables estimation of the interference direction of arrival estimation.

4.3.1 MUltiple SIgnal Classification (MUSIC)

The considered antenna array is here assumed to be perfectly calibrated and the cosmic sources are neglected. As already seen, the interference subspace dimension can be estimated by studying the array covariance matrix eigenvalues, i.e. by estimating the rank of the antenna array covariance matrix in a noiseless scenario, or the number of dominant (non constant) eigenvalues in a noisy scenario. The idea of the MUSIC algorithm [85, 55] is to compute a MUSIC spatial spectrum (or MUSIC skymap) that would highlight the individual N_r directions of arrival of the N_r impinging interference. By definition of the covariance matrix eigenvalue decomposition, the $M - N_r$ eigenvectors associated with the $M - N_r$ smallest (or constant) eiganvalues generate a noise subspace. And because of the orthogonality of the decomposition, any arbitrary vector lying in the signal subspace is orthogonal to this noise subspace.

Consider an arbitrary steering vector $\mathbf{a}(\theta, \phi)$ pointing in a direction defined by the polar components (θ, ϕ). The MUSIC skymap is then defined by:

$$P_{MUSIC}(\theta, \phi) = \frac{1}{\sum_{i=N_r+1}^{M} |\mathbf{a}^H(\theta, \phi)\mathbf{e_i}|^2} \tag{4.25}$$

$$= \frac{1}{\|\mathbf{a}^H(\theta, \phi)\mathbf{E_n}\|^2} \tag{4.26}$$

with:

- $\mathbf{e_i}$ the i^{th} antenna array covariance matrix eigenvector, considering the eigenvalues being sorted in a decresaing order.
- $\mathbf{E_n} = [\mathbf{e_{N_r+1}} \dots \mathbf{e_M}]$ a noise subspace basis as estimated with the covariance matrix eigenvalue decomposition.

The contrast function $P_{MUSIC}(\theta, \phi)$ reaches theoretically an undeterminate form as soon as the arbitrary steering vector $\mathbf{a}(\theta, \phi)$ is orthogonal to the noise subspace. However, the antenna array covariance matrix is estimated over a finite number of samples, and perfect orthogonality between a steering vector and a subset of its eigenvectors is not likely. This function will still reach a local maximum as soon as a steering vector points in a direction close to a signal (interference) direction of arrival. An optimization algorithm, like an ant colony optimization algorithm for example [59], would then make it possible

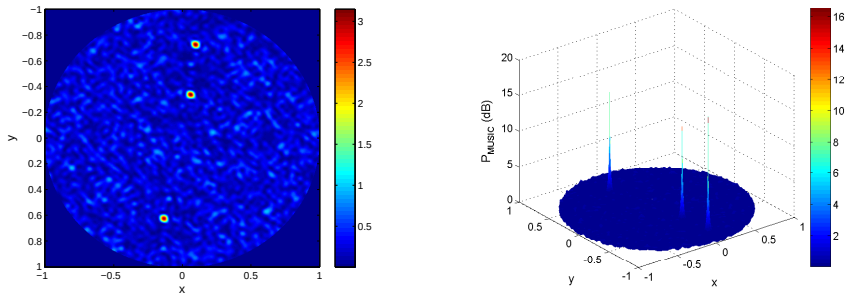

(a) (b)

Figure 4.10: MUltiple SIgnal Classification. Skymaps are given in dB. (a) Simulated skymap with three interferences impinging a 48-antenna array, INR = 0 dB. (b) MUSIC spatial skymap (contrast function) showing three peaks corresponding to the three interference signals directions of arrival.

to estimate the N_r interference signals' direction of arrival, and therefore their corresponding steering vector.

Figure 4.10 shows an example of the MUSIC algorithm on simulated data (48 antenna array, INR = 0 dB). Three interference signals can be seen on the initial raw skymap (see Figure 4.10.(a)). The MUSIC spatial skymap was then calculated over all the directions in the sky and can be seen on the Figure 4.10.(b) as a 3-dimensional surface. The three peaks on this figure correspond to steering vectors close to being orthogonal with the estimated noise subspace.

The performance of this algorithm is directly linked to the Interference-to-Noise Ratio [4], and therefore the ability to estimate the noise subspace according to the observation.

4.3.2 Minimum Variance Distortionless Response (MVDR)

Closely related to the LCMB beamformer seen in section 3.2.4, the idea behind the MVDR algorithm [25] is to minimize a beamformer output energy while keeping the beamforming vector in a constant position defined by the polar coordinates (θ, ϕ). This technique can therefore be seen as a constrained optimization problem.

We saw in the previous chapter that the classical beamforming output is written as:

$$x_{beam}(t) = \mathbf{w}^H.\mathbf{x}(t) \tag{4.27}$$

with:

- $\mathbf{x}(t)$ the $(M \times 1)$ antenna array output vector at time t.
- $\mathbf{w}$ an arbitrary $(M \times 1)$ beamforming vector.
- $x_{beam}(t)$ a weighted sum of the antenna array output at time t.

Minimizing the energy of $x_{beam}(t)$ is required in order to minimize the noise and interference contributions in the observed direction. This energy is written as:

$$\mathbb{E}\{|x_{beam}(t)|^2\} = \mathbf{w}^H \mathbf{R} \mathbf{w} \tag{4.28}$$

with $\mathbf{R} = \mathbb{E}\{\mathbf{x}(t)\mathbf{x}^H(t)\}$ the antenna array covariance matrix. It is also important to keep a fixed gain (usually a unitary gain) in the direction of interest. Let $\mathbf{a}(\theta, \phi)$ be the steering vector related to the direction of interest given by (θ, ϕ). The MVDR algorithm is then defined as:

$$\min_{\mathbf{w}} \mathbf{w}^H \mathbf{R} \mathbf{w} \quad \text{subject to} \quad \mathbf{w}^H \mathbf{a}(\theta, \phi) = 1 \tag{4.29}$$

This constrained optimization problem can be solved using the Lagrange multipliers method, in order to minimize the following expression:

$$\mathbb{L}(\mu, \mathbf{w}) = \mathbf{w}^H \mathbf{R} \mathbf{w} - \mu(\mathbf{w}^H \mathbf{a}(\theta, \phi) - 1) \tag{4.30}$$

The beamforming vector $\mathbf{w}$ minimizing this expression is given by:

$$\mathbf{w}_{\min} = \frac{\mathbf{R}^{-1}\mathbf{a}(\theta, \phi)}{\mathbf{a}^H(\theta, \phi)\mathbf{R}^{-1}\mathbf{a}(\theta, \phi)} \tag{4.31}$$

The MVDR contrast function is then defined as the power reached after beamforming toward the direction (θ, ϕ) by applying the vector $\mathbf{w}_{\min}$ at the antenna array output:

$$\begin{aligned} P_{\mathrm{MVDR}}(\theta, \phi) &= \mathbf{w}_{\min}^H \, \mathbf{R} \, \mathbf{w}_{\min} \\ &= \frac{1}{\mathbf{a}^H(\theta, \phi) \, \mathbf{R}^{-1} \, \mathbf{a}(\theta, \phi)} \end{aligned} \tag{4.32}$$

In the same way as the MUSIC algorithm, the function $P_{\mathrm{MVDR}}(\theta, \phi)$ will present local maxima as soon as the vector $\mathbf{a}^H(\theta, \phi)$ reaches the direction of arrival of an interference signal. Finding these maxima using an optimization algorithm will help estimate the interference steering vectors, and therefore an interference subspace basis.

Figure 4.11 shows again simulated data (the same parameters as in the simulation shown on Figure 4.10, but different interference locations). The MVDR constraint function is displayed on Figure 4.11.(b).

4.4 Conclusions on interference subspace estimation

The interference subspace estimation is a critical step in spatial filtering. A wrong estimation leads to data deterioration. A visual example of the impact of an inaccurate interference subspace estimation on the interference itself is shown in Figure 4.12.

The accuracy of the recovered interference subspace depends on the following parameters:

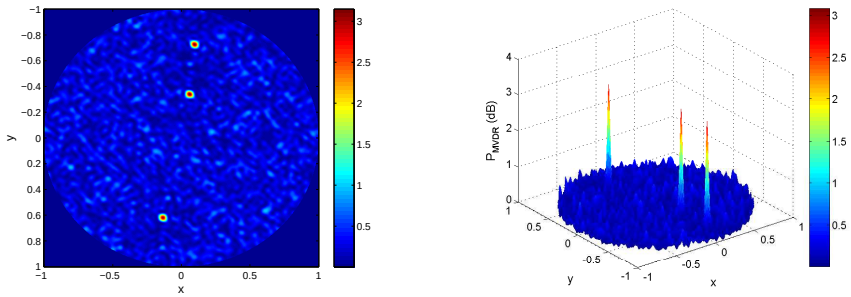

(a) (b)

Figure 4.11: Minimum Variance Distortionless Response. Skymaps are given in dB. (a) Simulated skymap with three interferences impinging a 48-antenna array (INR = 0 dB). (b) MVDR constraint function. Three peaks can be found and represent the directions of arrival of the three impinging interferences.

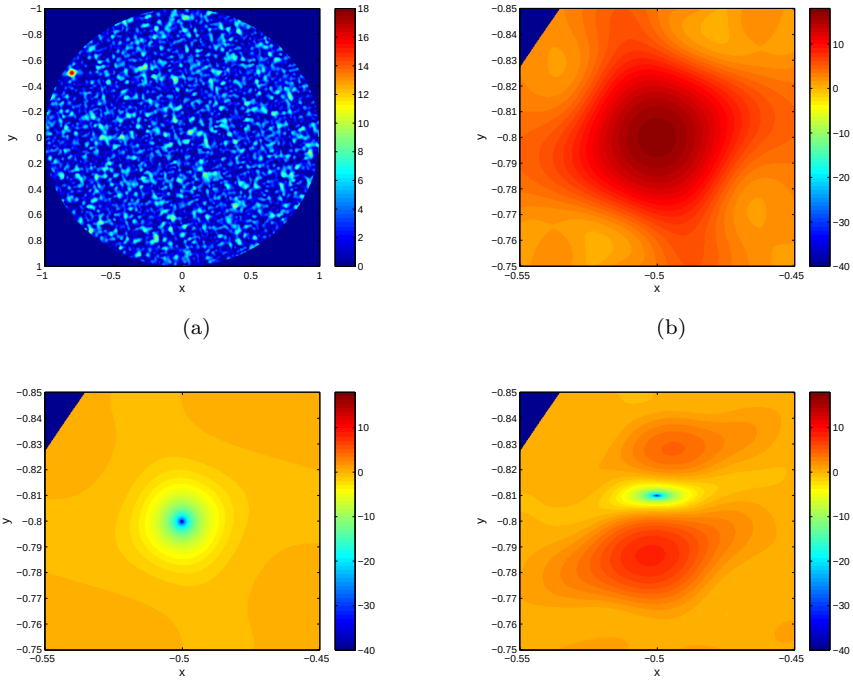

(a) (b)

(c) (d)

Figure 4.12: Impact of interference subspace estimation error on a skymap. Skymaps are given in dB. (a) Simulated skymap containing one interference. (b) Zoom on the interference location. (c) Zoom on the interference location after orthogonal projection based on the true interference steering vector. (d) Zoom on the interference location after orthogonal projection based on the (badly) estimated interference steering vector.

- the type of data available at the antenna array radio telescope output,
- the spatial filtering strategy that has been chosen,
- the computational complexity that remains available on the radio telescope system.

Antenna array radio telescopes usually provide single output in the case of beamforming, or array covariance matrices in the case of radio interferometry for sky imaging. The latter are calculated using fast digital correlators. The cyclostationary approach, consisting in correlating a signal with a frequency shifted version of itself, as well as the time-lag approach, consisting in correlating a signal with a time shifted version of itself, requires better resource sharing at the correlation stage (configuration of the observation parameters).

However, it has been seen in this chapter that approaches based on the attenuation of the cosmic source and system noise contributions, as well as multiple covariance matrices approaches, provide much better estimations than approaches based on a classical covariance matrix. In the event of estimation uncertainty, and when the number of interferences is much lower than the number of antennas (i.e. when the interference subspace dimension is much lower than the data vector space dimension), an alternative would be to reject a bigger subspace than the one estimated.

Suppose there is one interference impinging an antenna array. Projecting the interference subspace out of the data vector space (using an orthogonal or oblique projector), creates a hole in the skymap that has the size of the antenna array beam. It is however possible to enlarge this hole by projecting out the estimated interference subspace, as well as its close neighborhood on the skymap. The Figure 4.13 shows an example of multiple beam projection. The size of the projected area is parameterized by the neighborhood size and the number of rejected directions of arrival.

Another approach allowing the enlargement of the antenna array beam is known as covariance matrix tapering [46], consisting in an apodization of the covariance matrix.

When interferences remain fixed in the field of view of the antenna array, their steering vectors remain constant. Another approach allowing an improvement in interference subspace estimation accuracy is subspace tracking [29]. The basic idea of subspace tracking is to update the interference subspace estimation each time new information is available at the antenna array output instead of keeping on re-estimating this subspace over time. However, this approach performs poorly if the interference subspace evolves continuously with time, due to a jammer move or intermittent jammers for example.

Even if most of the techniques presented in this chapter are based on matrices decompositions, the computational complexity of these techniques is mainly due to the covariance matrices calculations. Since the dimension of the interference subspace is usually low compared to the data vector space dimension (the interference subspace dimension is related to the number of interferences impinging the antenna array radio telescope over a narrow frequency bandwidth), methods consisting in retrieving the dominant eigenvalues and eigenvectors of a matrix for a low computational cost, such as the power method [30], markedly improve the global computational cost of an interference mitigation algorithm.

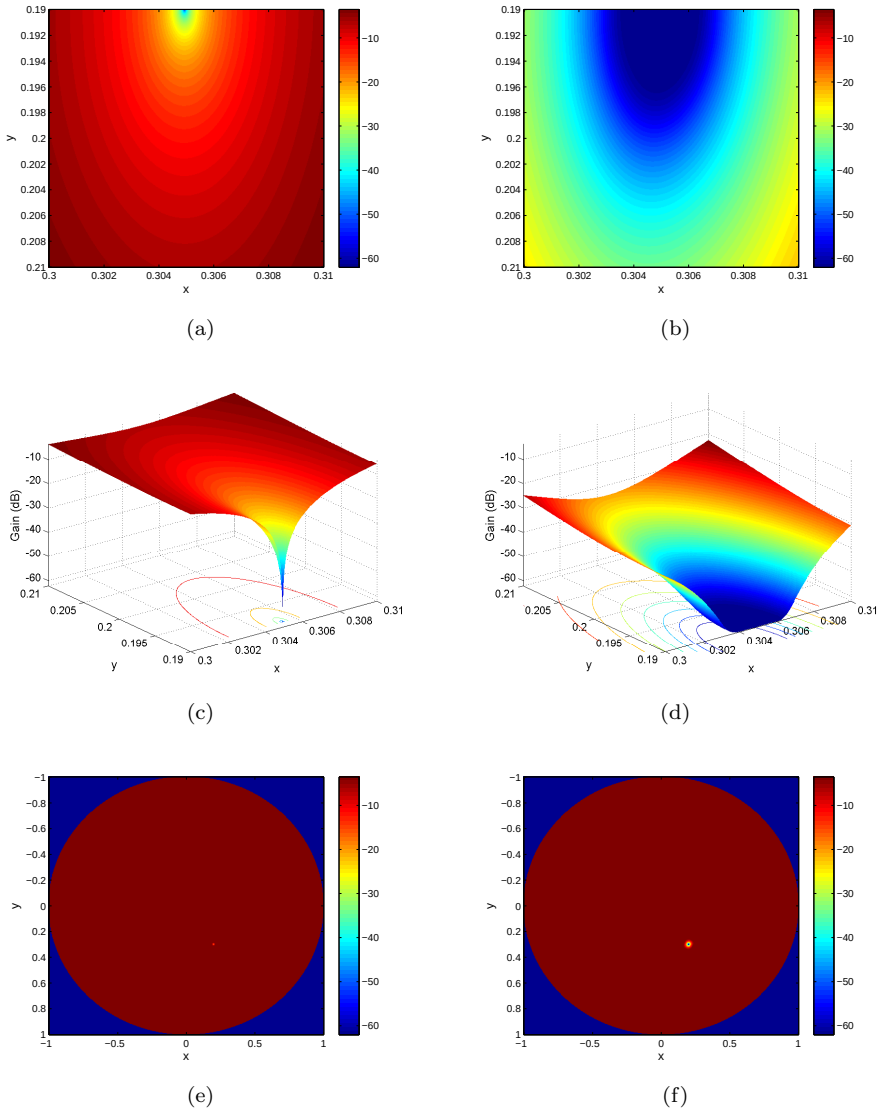

Figure 4.13: Multiple beam projection. Skymaps are given in dB. (a) Orthogonal projection based on a single steering vector. (b) Orthogonal projection based on the same steering vector as (a), by also rejecting 10 other directions of arrival located in a close neighborhood. (c) and (d) 3-dimensional representation of the map (a) and (b), respectively. (e) and (f) Global skymaps after the projection presented in (a) and (b), respectively.

Chapter 5

RFI mitigation implementation

5.1 Introduction

This chapter presents an RFI mitigation algorithm that is currently being implemented and tested on the radio telescope demonstrator EMBRACE. This demonstrator is already operational but not yet commissioned to work as a scientific instrument. Its back end is a LOFAR station back end.

The first part of the chapter presents the techniques discussed in this thesis applied to LOFAR data. Thanks to the Transient Buffer Board, which allows full bandwidth antenna waveforms to be recorded on the LOFAR backend, different approaches have been tested on LOFAR Low and High Band Antenna signals.

The second part of the chapter presents the whole EMBRACE system. In order to choose the stage at which the proposed algorithm can be implemented, it is necessary to know the signal path, as well as the type of data and the computational power available.

Finally, the algorithm based on an oblique projector is presented. Through simulations applied on real data, the performance of this algorithm is compared to the expected results.

5.2 LOFAR data processing

The Transient Buffer Board (TBB) is a device located on LOFAR station cabinets that allows the recording of full bandwidth antenna waveforms. Two observations are presented here : one Low Band Antenna observation, particularly a subband of it corrupted by a land mobile, and one High Band Antenna observation, particularly a subband of it corrupted by a strong pager system. The same processing was applied to both observations.

5.2.1 LOFAR LBA data

The Low Band Antenna observation (frequency bandwidth $= 0 - 100$ MHz) was made with a Dutch LOFAR station on February 11th, 2010. The observation was made with a 47-subantenna array. Figure 5.1 presents the observation.

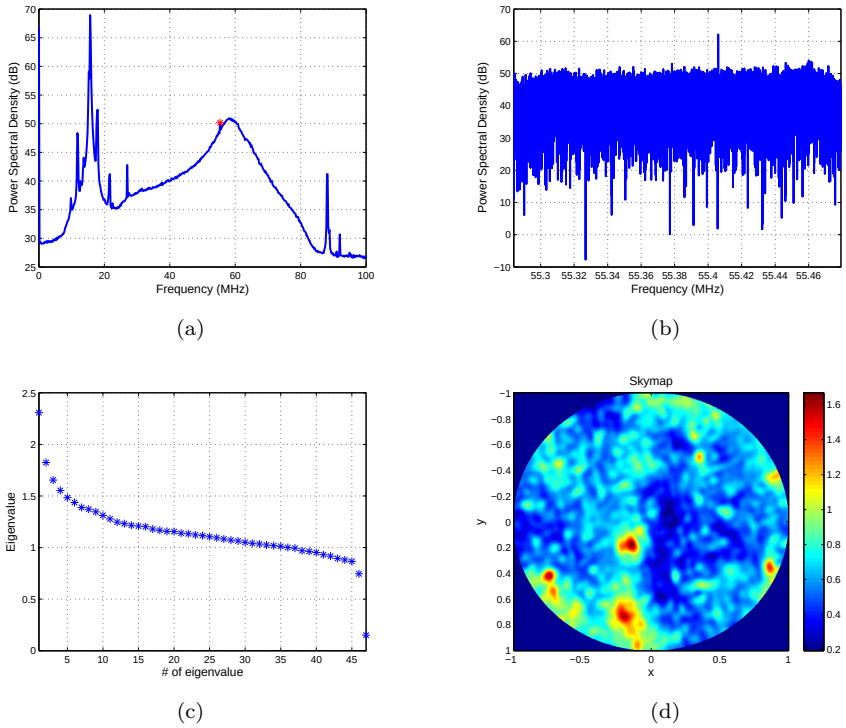

Figure 5.1: LOFAR Low Band Antenna corrupted observation at 55 MHz. 47 sub antennas array. (a) Power Spectral Density of the observation. The red star highlights the subband of interest. This subband is corrupted by a land mobile signal. (b) Power Spectral Density of the subband of interest. The narrow band peak at 55.41 MHz corresponds to the land mobile. (c) Singular values of the classical covariance matrix of the observation. The signal subspace seems to be 1- or 2-dimensional. (d) Skymap of the observation (in dB). The strong interference is located on the horizon. The other sources correspond to well known cosmic sources.

Figure 5.1.(a) is the whole Power Spectral Density of the observation. All the peaks on the spectrum correspond to interference. The subband selected to apply the processing is highlighted by a red star, at 55 MHz. This frequency bandwidth is dedicated to land mobile applications in the Netherlands. Figure 5.1.(b) is the Power Spectral Density of the subband of interest. One narrow peak can be seen on this spectrum. It corresponds to a land mobile signal. Figure 5.1.(c) shows the singular values of the classical covariance matrix of the observation. One singular value clearly dominates the others. It corresponds to the signal subspace, and more precisely the interference subspace. The skymap on Figure 5.1.(d) shows the interference on the horizon. Two other (well-known) cosmic sources can be seen in the sky.

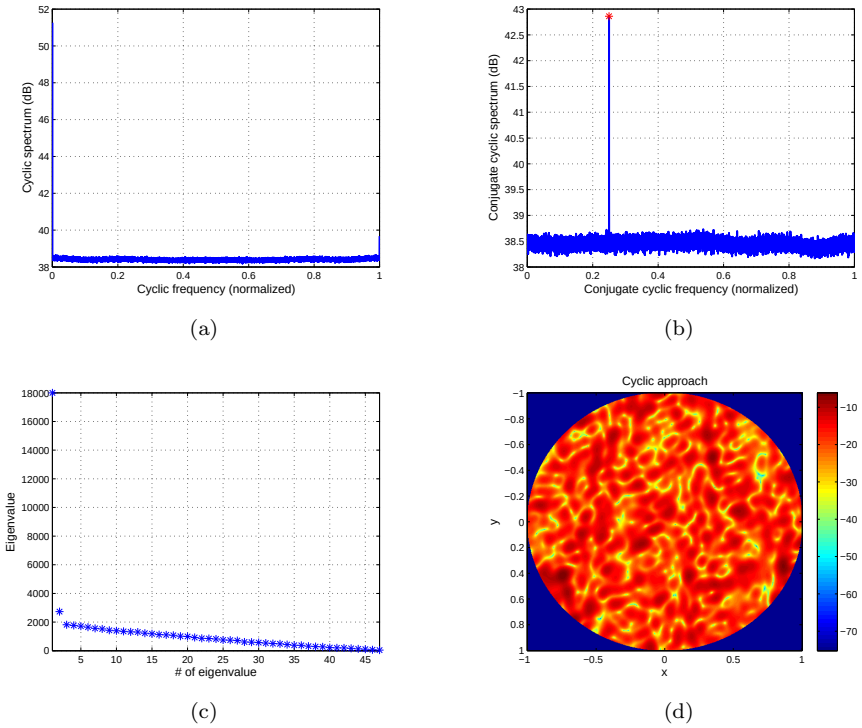

Figure 5.2: Cyclostationary approach. (a) Cyclic spectrum of the observation. No cyclic frequencies. (b) Conjugate cyclic spectrum of the observation. The peak on the spectrum corresponds to the interference conjugate cyclic frequency $\alpha_0 = 0.25$(highlighted by a red star). (c) Singular values of the conjugate cyclic matrix at α_0. (d) Skymap (in dB) made with the conjugate cyclic matrix at α_0.

Interference subspace estimation

Figure 5.2 presents the cyclostationary approach applied to the LBA observation. Figures 5.2.(a) and 5.2.(b) are respectively the cyclic and conjugate cyclic spectra of the observation. The interference has a conjugate cyclic frequency, highlighted by a red star on Figure 5.2.(b). Figure 5.2.(c) shows the singular values of the conjugate cyclic matrix. The signal subspace is 1-dimensional, since a single singular value dominates the others. The skymap 5.2.(d) is the skymap built with the conjugate cyclic matrix considered. The skymap seems saturated, and the interference location is hard to identify.

Figure5.3 is the time-lag approach applied to the observation. Figure 5.3.(a) is the auto-covariance function of the subband of interest. One peak on this function, highlighted by a red star, corresponds to a strong auto-correlation of the signal with itself at time-lag $\tau_0 = 5$ samples. Figure 5.3.(b) are the singular values of the time-lagged covariance matrix. Again, one singular value dominates the others. It corresponds to the interference subspace (or non-white signal subspace). Figure 5.3.(c) is the skymap built with the time-lagged covariance matrix. The interference location can be easily identified. The cosmic sources, in the sky, are no longer visible. This observation confirms the whiteness

assumption concerning cosmic sources.

The MUSIC approach has also been considered. Figure 5.4 shows the 4 MUSIC functions calculated by respectively considering a 1, 2, 3 and 4-dimensional signal subspace. Figure 5.4 presents 3 maxima.

The MVDR approach applied to the observation is shown on Figure 5.5. The sources locations are not easier to identify on this map than on the classical covariance matrix skymap 5.1.(d).

Spatial filtering

Figure 5.6 is the orthogonal approach applied to the observation. On Figure 5.6.(a), the orthogonal projector was built with the interference subspace estimated using the cyclostationary approach, whereas on Figure 5.6.(b), the projector was built with the interference subspace estimated with the time-lag approach. The results seem similar. A hole in the map is located at the interference location.

Figure 5.7 shows the results of the oblique projection approach applied to the observation. An oblique projector was built for each direction in the sky. Again, the oblique projector was built either with the interference subspace estimated with the cyclostationary approach (Figure 5.7.(a)) or with the time-lag approach (5.7.(b)). The cosmic sources are less widely spread than with the orthogonal projector. Because of the construction of the oblique projector, a global maximum of the skymap can be seen at the interference location.

The interference subspace subtraction was applied to the data. Figure 5.8.(a) shows the interference subspace subtraction function, based on the interference spatial signature estimated with the cyclostationary approach, with its global minimum highlighted by a red star. Figure 5.8.(b) is the skymap made by subtracting the interference subspace covariance matrix from the classical covariance matrix. The interference is no longer visible, and the cosmic sources are still located in the sky.

5.2.2 LOFAR HBA data

The observation considered in this section was made with a Dutch LOFAR High Band Antenna station (24 antenna tilesets, frequency bandwidth = $100 - 200$ MHz) on July 15th, 2010. Figure 5.9.(a) is the Power Spectral Density of the observation. All the peaks correspond to interference. The interference of interest to apply the different interference mitigation techniques is highlighted by a red star at 109.28 MHz. This frequency is dedicated to aviation radio navigation in the Netherlands. Figure 5.9 is the Power Spectral Density of the subband of interest. Figure 5.9.(c) are the singular values of the classical covariance matrix. The strong dominant singular value corresponds to the interference. Figure 5.9.(d) is the skymap of the observation (because of aliasing due to the observation frequency and antenna array size, the skymaps in this section are limited to a smaller field of view). The radio navigation system can be clearly located on the map.

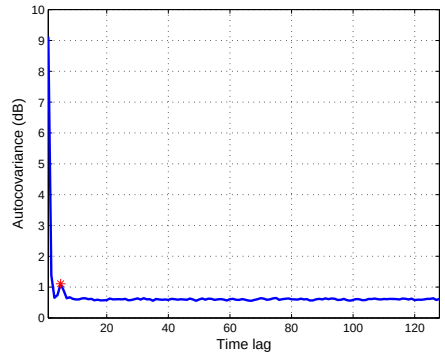

(a)

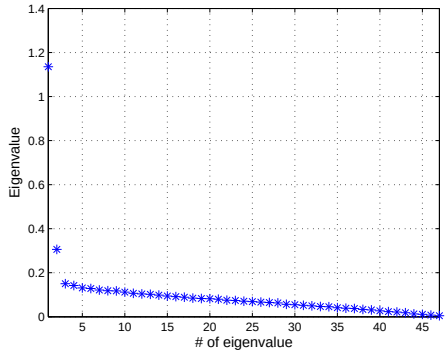

(b)

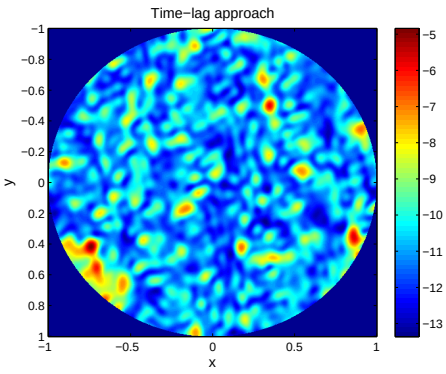

(c)

Figure 5.3: Time-lag approach. (a) Autocovariance function of the observation. The peak at time-lag $\tau_0 = 5$ samples (highlighted by a red star) is the subband of interest. (b) Singular values of the time-lagged covariance matrix at τ_0. (c) Skymap (in dB) made with the time-lagged covariance matrix at τ_0. The cosmic sources are no longer visible.

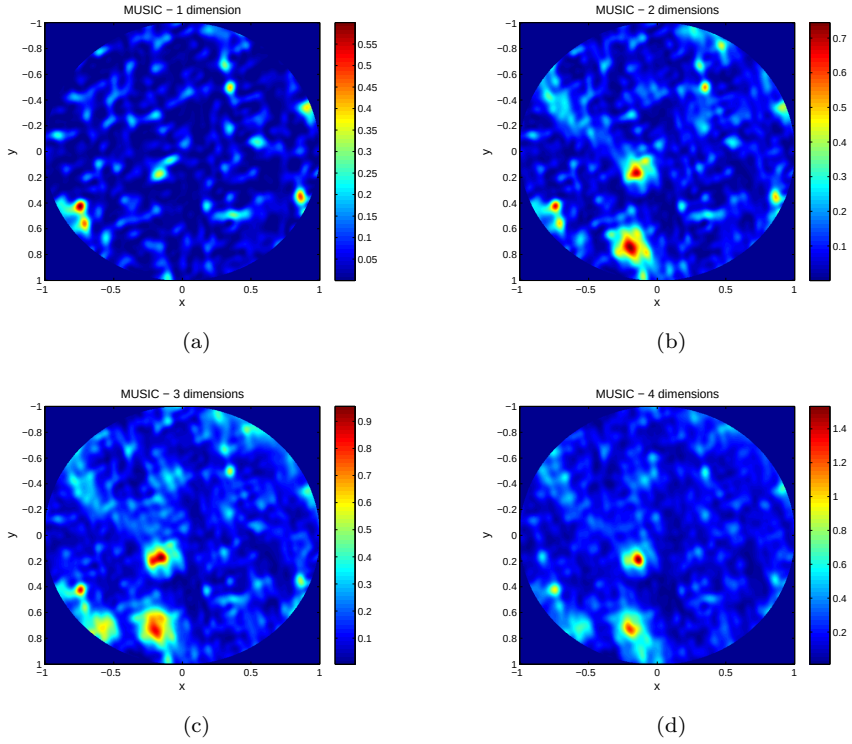

(a) (b) (c) (d)

Figure 5.4: MUSIC approach. (a) MUSIC function selecting a 1-dimensional signal subspace (in dB). (b) MUSIC function selecting a 2-dimensional signal subspace (in dB). (c) MUSIC function selecting a 3-dimensional signal subspace (in dB). (d) MUSIC function selecting a 4-dimensional signal subspace (in dB). The signal subspace seems to be 4-dimensional, even if the sources are not point sources.

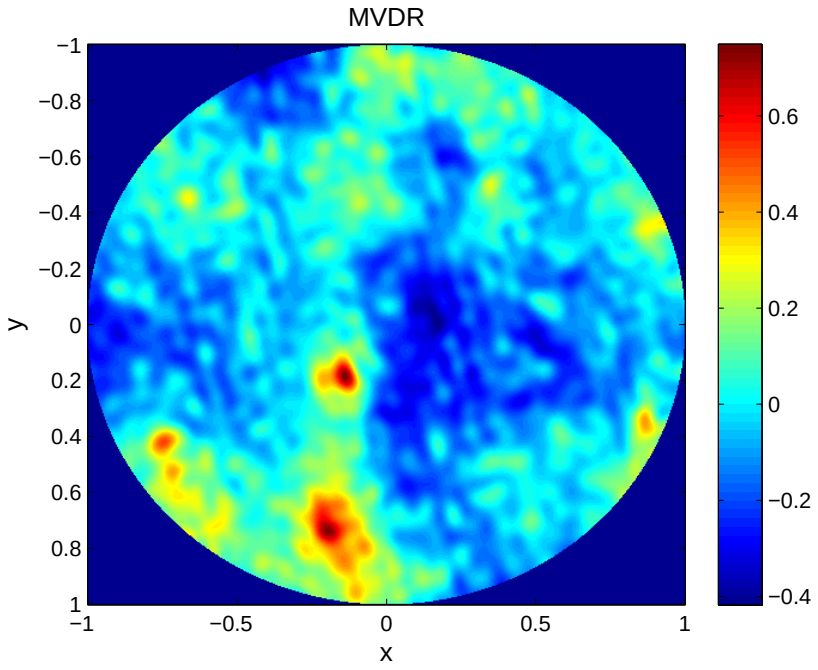

Figure 5.5: MVDR approach. The skymap (in dB). The sources' locations are hard to identify.

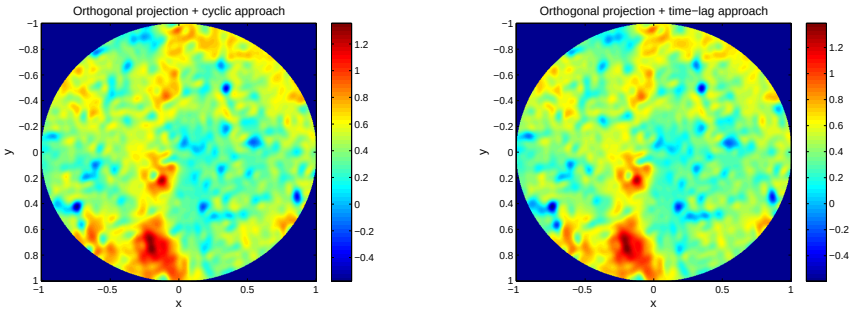

(a) (b)

Figure 5.6: Orthogonal projection (skymaps given in dB). (a) Interference subspace estimated with the cyclostationary approach. (b) Interference subspace estimated with the time-lag approach.

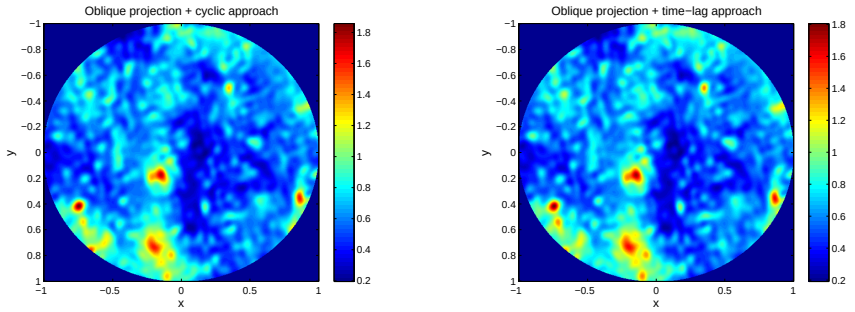

(a) (b)

Figure 5.7: Oblique projection (skymaps given in dB). (a) Interference subspace estimated with the cyclostationary approach. (b) Interference subspace estimated with the time-lag approach.

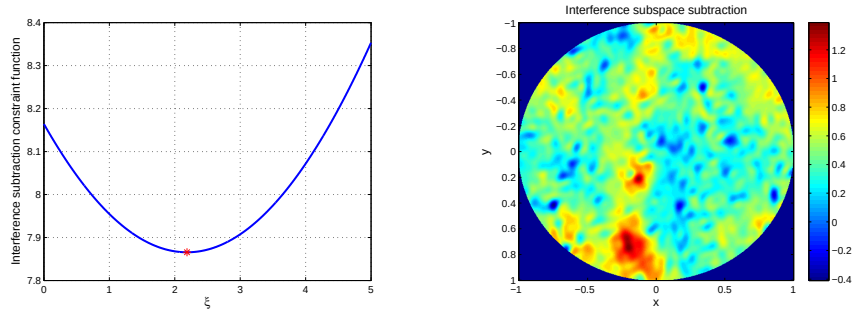

(a) (b)

Figure 5.8: Interference subspace subtraction approach. The interference spatial signature was estimated with the cyclostationary approach. (a) Interference subspace subtraction function. The point highlighted by a red star corresponds to the function global minimum. (b) Skymap (in dB) of the interference subspace subtracted from the classical covariance matrix.

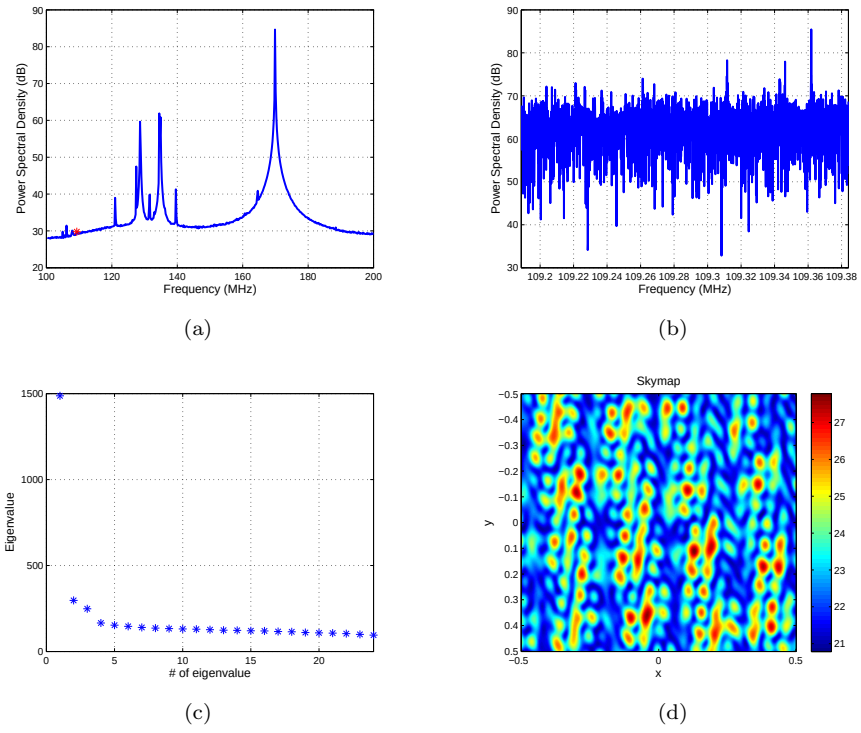

Figure 5.9: LOFAR High Band Antenna corrupted observation at 109.28 MHz. 24-antenna array. (a) Power Spectral Density of the observation. The red star highlights the subband of interest. This subband is corrupted by an aviation radio navigation system. (b) Power Spectral Density of the subband of interest. (c) Singular values of the classical covariance matrix of the observation. The signal subspace seems to be 1-dimensional. (d) Skymap of the observation (in dB). The radio navigation system corresponds to the strongest point on the map.

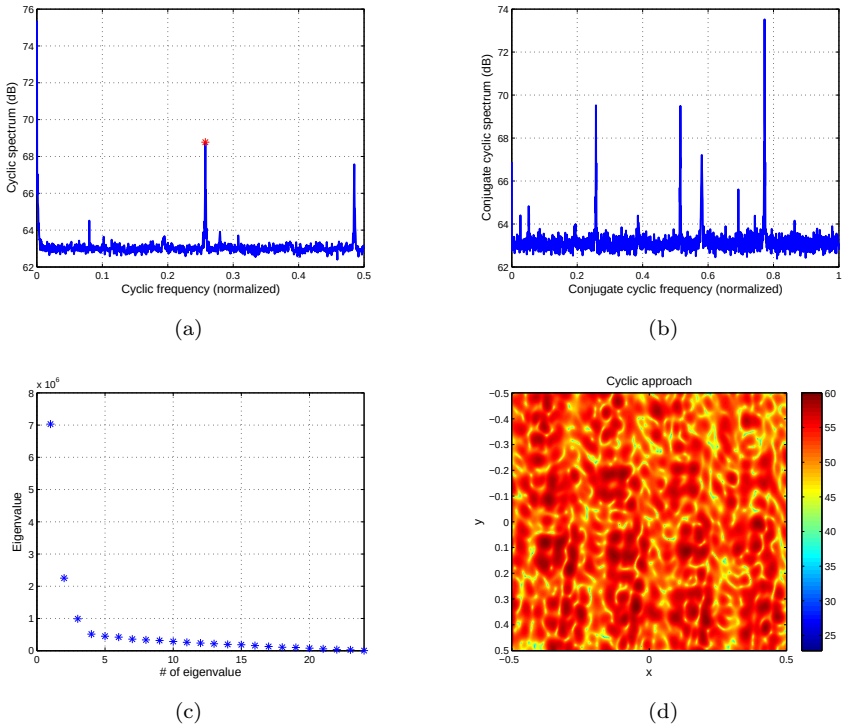

Figure 5.10: Cyclostationary approach. (a) Cyclic spectrum of the observation. The peaks on the spectrum correspond to the interference cyclic frequencies. The cyclic frequency $\alpha_0 = 0.2574$ (highlighted by a red star) was chosen for the rest of the study. (b) Conjugate cyclic spectrum of the observation. (c) Singular values of the cyclic matrix at α_0. (d) Skymap (in dB) made with the cyclic matrix at α_0.

Interference subspace estimation

Figures 5.10.(a) and 5.10.(b) are respectively the cyclic and conjugate cyclic spectra of the observation. Between 3 and 5 cyclic frequencies and between 5 and 11 conjugate cyclic frequencies can be identified on these spectra. The cyclic frequency of interest is highlighted by a red star on Figure 5.10.(a). Figure 5.10.(c) are the singular values of the cyclic matrix. The dominant singular value corresponds to the cyclic interference. Figure 5.10.(d) is the skymap built with the cyclic matrix. Some strong points on the map, repeated because of the array beam shape, could correspond to the interference location.

Figure 5.11.(a) is the autocovariance function of the observation. Its periodicity is due to the interference strength and modulation. The red star on this Figure highlights the time-lag chosen to perform the interference subspace estimation ($\tau_0 = 12$ samples). Figure 5.11.(b) shows the singular values of the time-lagged covariance matrix. Again, the dominant singular value corresponds to the pager signal. Figure 5.11.(c) is the skymap made with the time-lagged covariance matrix.

The MUSIC approach was also applied, in the same way as with the Low

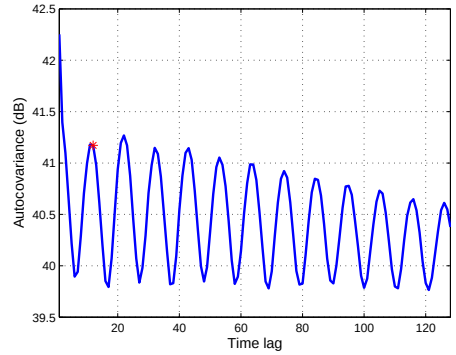

(a)

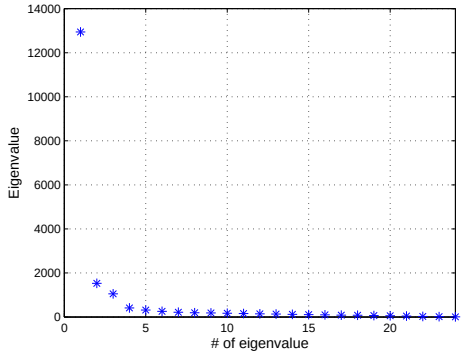

(b)

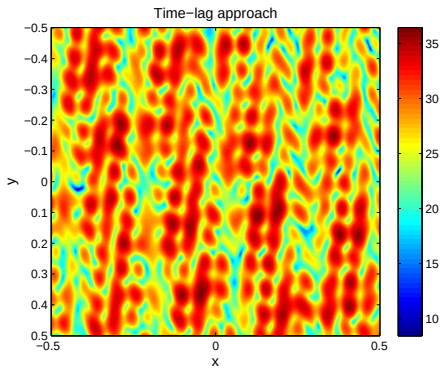

(c)

Figure 5.11: Time-lag approach. (a) Autocovariance function of the observation. The peak at time-lag $\tau_0 = 12$ samples (highlighted by a red star) is of interest. (b) Singular values of the time-lagged covariance matrix at τ_0. (c) Skymap (in dB) made with the time-lagged covariance matrix at τ_0.

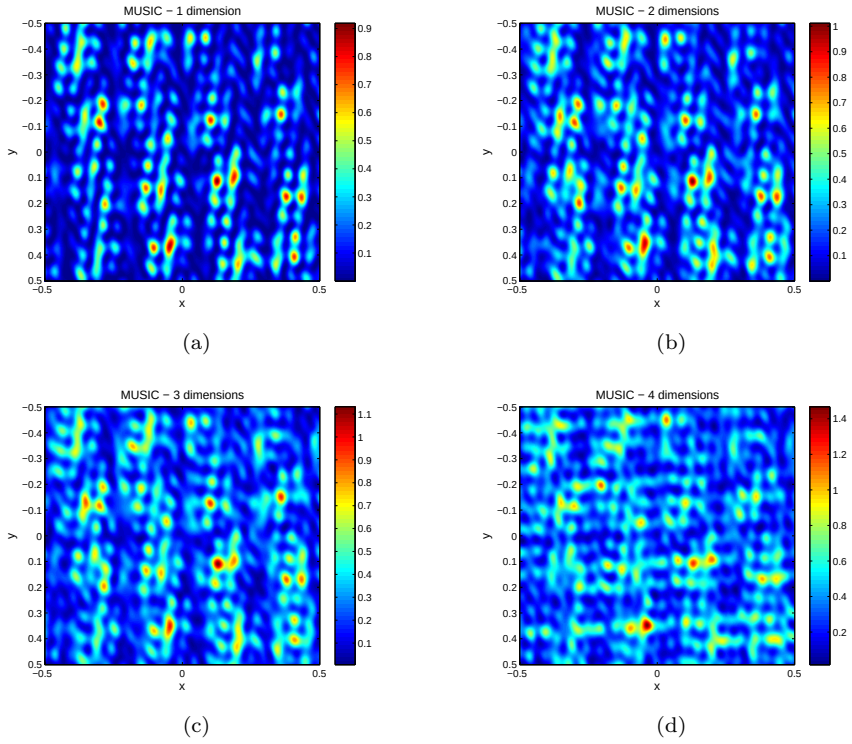

(a) (b)

(c) (d)

Figure 5.12: MUSIC approach. (a) MUSIC function selecting a 1-dimensional signal subspace (in dB). (b) MUSIC function selecting a 2-dimensional signal subspace (in dB). (c) MUSIC function selecting a 3-dimensional signal subspace (in dB). (d) MUSIC function selecting a 4-dimensional signal subspace (in dB).

Band Antennas observation, to the classical covariance matrix. The four MUSIC functions, shown on Figure 5.12 (respectively selecting a 1, 2, 3 and 4-dimensional signal subspace), do not show the same source locations. Based on the previous studies, the signal subspace of the observation seems to be 1-dimensional. This indicates that Figure 5.12.(a) is the one that shows the right interference location (highlighted by the strongest area on the map).

The MVDR approach, shown on Figure 5.13 appears to highlight the same source location as Figure 5.12.(a).

Spatial filtering

The orthogonal approach was applied on these data. Figure 5.14.(a) shows the result of the orthogonal projector with the interference subspace estimated with the cyclostationary approach, whereas Figure 5.14.(b) shows the result of the orthogonal projector applied by estimating the interference subspace with the time-lag approach. The two results are similar, and a hole in the map can be seen at the interference location.

Figure 5.15 presents the results of the oblique projector applied to the data by respectively estimating the interference subspace with the cyclostationary approach (Figure 5.15.(a)) and with the time-lag approach (Figure 5.15.(b)).

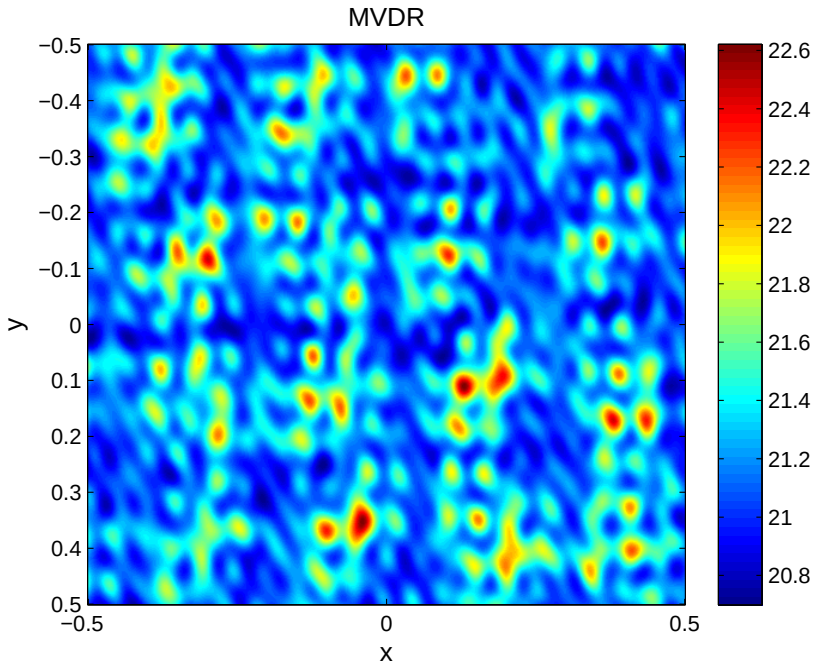

Figure 5.13: MVDR approach. The skymap (in dB). The locations of the sources are hard to identify.

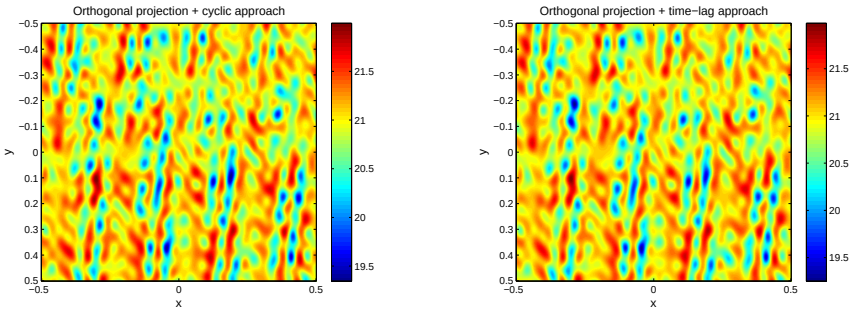

(a) (b)

Figure 5.14: Orthogonal projection (skymaps given in dB). (a) Interference subspace estimated with the cyclostationary approach. (b) Interference subspace estimated with the time-lag approach.

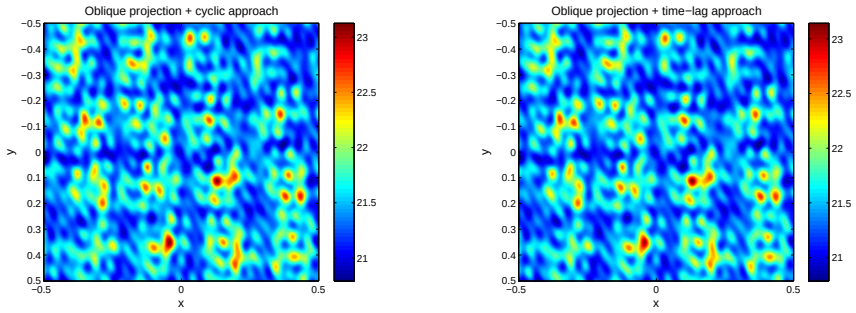

(a) (b)

Figure 5.15: Oblique projection (skymaps given in dB). (a) Interference subspace estimated with the cyclostationary approach. (b) Interference subspace estimated with the time-lag approach.

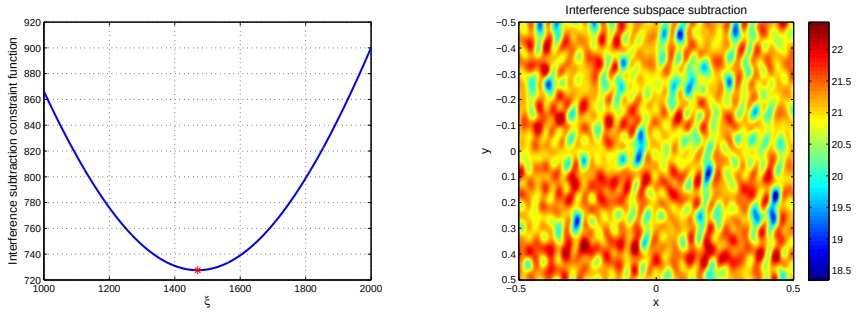

(a) (b)

Figure 5.16: Interference subspace subtraction approach. The interference spatial signature was estimated with the cyclostationary approach. (a) Interference subspace subtraction function. The point highlighted by a red star corresponds to the function global minimum. (b) Skymap (in dB) of the interference subspace subtracted from the classical covariance matrix.

Again, the results are similar with the two approaches.

The interference subspace subtraction technique is presented on Figure 5.16. Figure 5.16.(a) shows the interference subtraction function, with the interference spatial signature estimated with the cyclostationary approach. The red star on the function corresponds to its global minimum. Figure 5.16.(b) is the skymap recovered after subtracting the interference covariance matrix from the classical covariance matrix. This map seems noisy, with no interference contribution.

5.2.3 Conclusions on LOFAR data processing

The processing applied to the LOFAR data seems as efficient on LBA data as on HBA data, though the results are easier to conclude on with LBA data because of the wider field-of-view. However, concluding on the impact of these processing techniques with respect to cosmic sources is a tough task, with no information concerning the reality of the data.

Figure 5.17: French EMBRACE station inside its radome, located at the Nançay observatory. Courtesy of Dr. Stephen Torchinsky.

The results shown on Figures 5.7 and 5.8.(b) seem to match the results expected from the RFI mitigation algorithms.

5.3 EMBRACE

5.3.1 EMBRACE architecture

Overview

EMBRACE, the Electronic Multi-Beam Radio Astronomy Concept [61, 17, 16, 91], is a European mid frequency aperture array demonstrator for the international Square Kilometer Array radio telescope. This project is led by the Netherlands Institute for Radio Astronomy, ASTRON, and several European institutes contributed to the overall system (France, Italy, Germany).

The demonstrator is designed to work in a frequency bandwidth ranging from 500 MHz up to 1500 MHz. Two stations currently exist and are located in Nançay, France, and in Westerbork, The Netherlands. The French station is shown on Figure 5.17.

The French station comprises 9216 Vivaldi antenna elements (see Figure 5.18), half for each polarization, whereas the Dutch station comprises 20736 elements. Only half of them arecurrently exploited (single polarization). These antenna elements are phased together, so that the stations are able to simultaneously steer two independent directions in the sky.

The beamforming process is split into two sub-processes. An analog beamforming is first applied at the antennas output through beamformer chips [21], then a digital beamforming is applied at the back end stage.

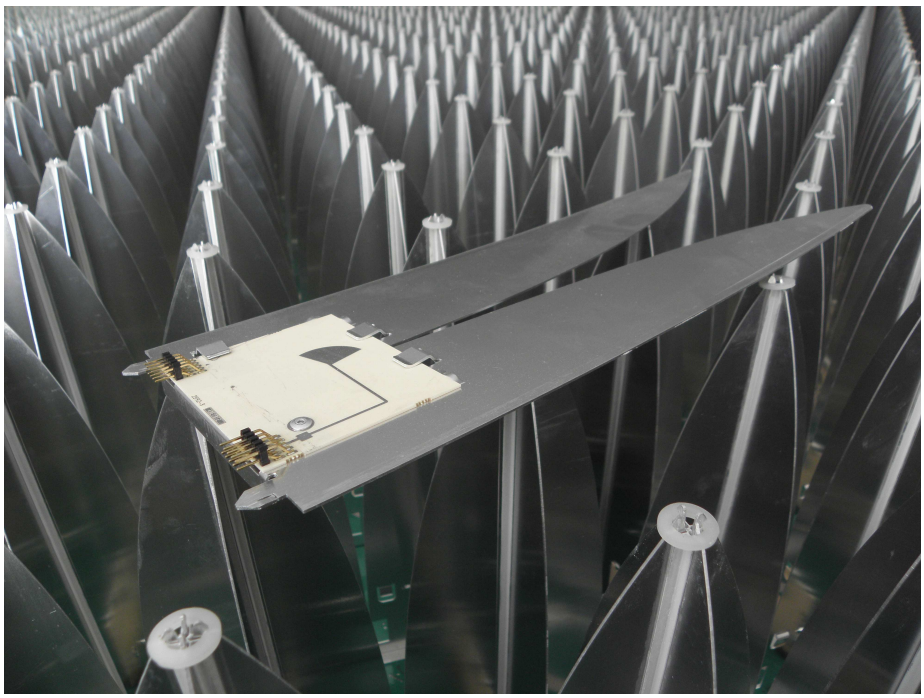

Figure 5.18: One Vivaldi antenna element of the phased antenna array EMBRACE. Courtesy of Dr. Stephen Torchinsky.

Front end

The EMBRACE front end is made of a regular grid antenna array isolated in a radome, together with radio frequency signal pre-processing boards. The signal coming out of the antennas is first amplified through Low Noise Amplifiers (LNA), high-pass filtered, and then enters a beamformer chip. Each beamformer chip receives 4 antenna signals, and provides two independent outputs corresponding to two independent directions in the sky chosen by the end-user. These beamformer chips are located on a hex board. Each hex board hosts 3 beamformer chips. One hex board is shown on Figure 5.19.(a).

The two independent outputs of each beamformer chip are then combined on a center board grouping together 6 hex boards. These signals are then sent to the back end through coaxial cables. These coaxial cables also provide the DC power to the front end, and Ethernet control signals to the beamformer chips.

Back end

The EMBRACE back end [78] is outside the radome, hosted in a shielded cabinet. The analog signals (the two independent beams provided by each tile) are first converted down to a low frequency before entering a Receiver Control Unit (RCU) [71]. The Figure 5.19.(b) shows the coaxial cables coming from the tiles and entering the back end cabinet. After filtering, the signal is digitized and split into 512 subbands using a polyphase filterbank. Each subband is processed

independently, and a complex weight is attributed to them in order to perform digital beamforming.

The EMBRACE back end provides two kind of data : beamlets and crosslets:

- Beamlets correspond to the raw data coming out of the radio telescope after both analog and digital beamforming have been performed. The two beamlets (for the two independent beams) are integrated over one second, and one sample per beam is released every second.
- The crosslets correspond to tileset correlation matrices integrated over one second. The signals correlated here have not gone through the digital beamforming stage, only the analog one.

The crosslets are provided either for a single subband with a frequency bandwidth $\Delta f = 195.3$ kHz, or over multiple subbands over a frequency bandwidth $\Delta f \approx 10$ MHz (512×195.3 kHz). In the latter case, one subband is processed each second. After 512s, the whole frequency bandwidth has been processed, and the process starts over at the beginning of the bandwidth of interest.

For example, Figure 5.20 shows the full power received from EMBRACE in the full frequency bandwidth mode during a GPS satellite drift scan. The bandwidth is centered at 1176.45 MHz, and is 99.993 MHz wide. The received power has been calculated using the squared Frobenius norm of the crosslets provided each second from the system back end. After 8 minutes and 32 seconds, the whole frequency bandwidth has been scanned and the system loops back to restart a new scan over the same bandwidth.

Figure 5.21 shows an observation in the single subband mode. The bandwidth considered here is centered at 1176.45 MHz and is 195.3 kHz wide. This observation is again a GPS satellite drift scan. The power drop is due to the satellite coming out of the RF beam formed by the antenna array. The samples provided by the system are integrated over one second, and then released. The received power has here also been calculated using the squared Frobenius norm of the crosslets provided each second by the system.

Figure 5.22 shows a summary of the EMBRACE architecture going from the antenna to the end-user data.

5.4 RFI mitigation algorithm

The aim of the project is to implement a real time RFI mitigation algorithm on the system, based on an oblique projector.

5.4.1 Strategy

Data model

We first consider the following single narrow band interference data model:

$$\mathbf{x}(t) = \mathbf{a_r}.r(t) + \mathbf{a_c}.c(t) + \mathbf{n}(t) \tag{5.1}$$

with:

- $\mathbf{x}(t)$ the instantaneous EMBRACE antenna tiles data output,

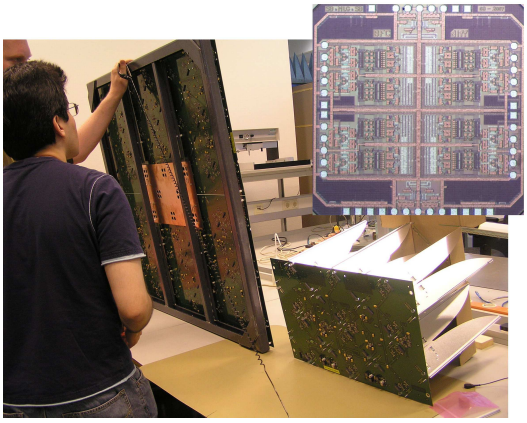

(a)

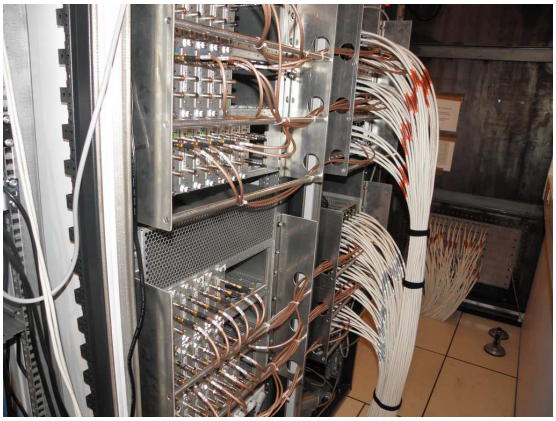

(b)

Figure 5.19: (a) An EMBRACE hex board. This board contains high pass filters, Low Noise Amplifiers and beamformer chips. The Vivaldi antenna elements are plugged on it. The board performs the first processing of the signal path on the antennas' output. (b) The analog signals coming out of the tiles enter the EMBRACE back end for filtering, digitization and further signal processing. Courtesy of Dr. Stephen Torchinsky.

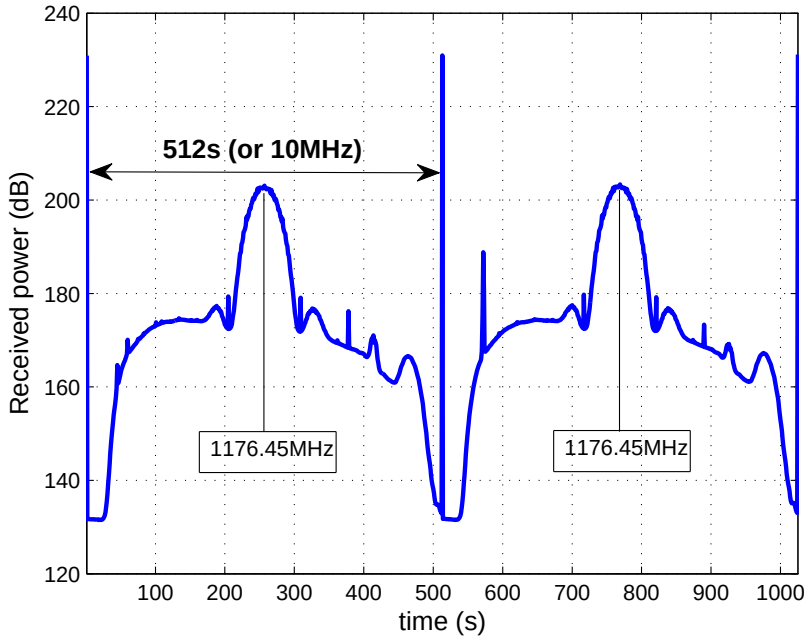

Figure 5.20: EMBRACE observation in the full frequency bandwidth mode. The frequency bandwidth of interest is centered at 1176.45 MHz and is 99.993 MHz wide. It corresponds to a GPS satellite drift scan. The radio telescope analog beam was steered in a fixed direction in the sky while the satellite crossed it (drift scan). After 8 minutes and 32 seconds (512s), the scan restarts at the beginning of the observation bandwidth. Each subband signal is integrated over 1 second and released by the back end.

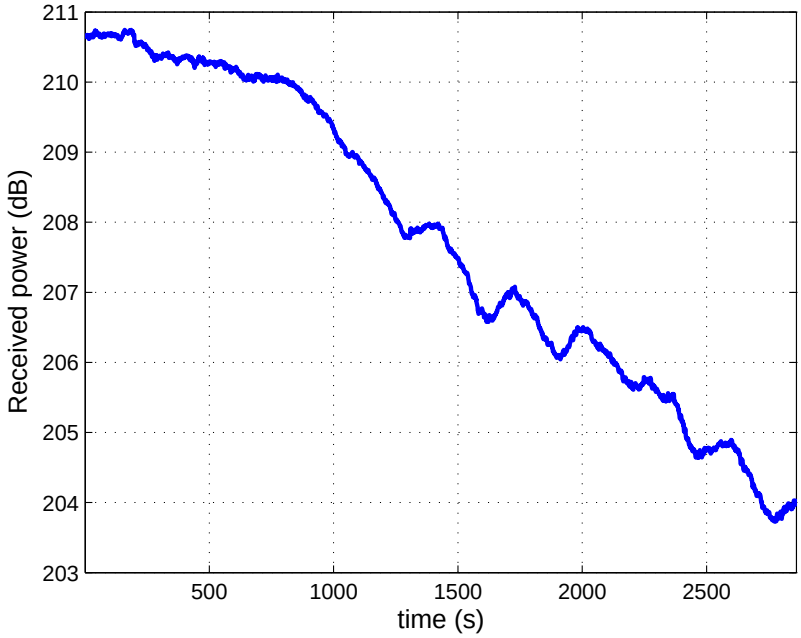

Figure 5.21: EMBRACE observation in the single subband mode. The subband of interest is centered at 1176.45 MHz and is 195.3 kHz wide. This observation is a GPS satellite drift scan. The received power decreases as the satellite exits the analog beam.

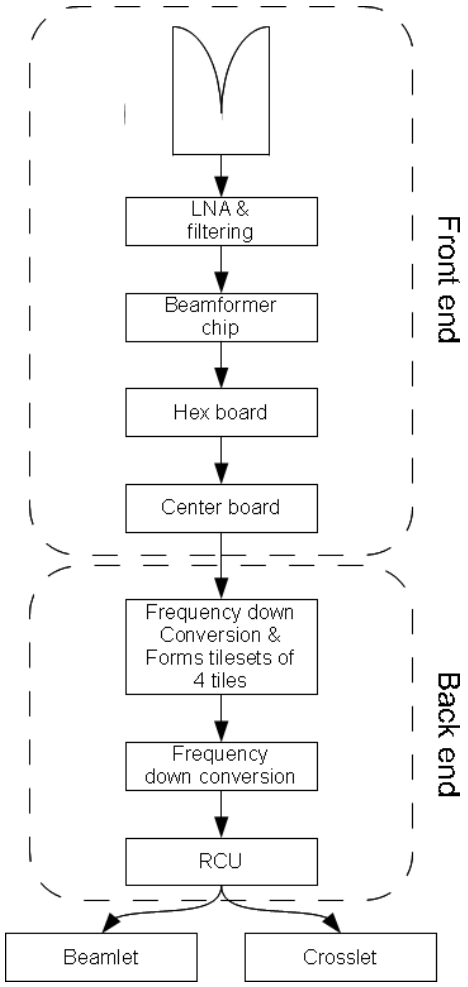

Figure 5.22: EMBRACE architecture. The front end is composed of Vivaldi antenna elements located in a radome. The signals provided by these antennas are amplified, filtered, beamformed (analog beamforming), combined in tiles (groups of hex boards) and sent to the back end. The back end, located in a shielded cabinet combines 4 tiles, converts the signals to a lower frequency, digitizes, digitally beamforms and processes them. The data provided by the system are beamlets (beamformer output samples) and crosslets (tileset correlation matrices)

- $\mathbf{a_r}$ the steering vector corresponding to the narrow band interference $r(t)$,
- $\mathbf{a_c}$ the steering vector corresponding to the cosmic source of interest $c(t)$,
- $\mathbf{n}(t)$ the instantaneous EMBRACE system noise contribution.

Since EMBRACE is a dense aperture array, the noise vector $\mathbf{n}(t)$ of the latter data model could not be modeled with independent entries. However, the system architecture is such that the data vector $\mathbf{x}(t)$ is not made of the individual antenna signals, but antennas tileset signals. The tiles are assumed to be distant enough for the electro magnetic coupling between tiles to be neglected.

Oblique projector

Beamforming using a delay and sum beamformer in the direction of the cosmic source of interest would not remove the interference contribution:

If $\mathbf{w}$ is the digital beamforming weights vector applied to the system, we have:

$$\mathbf{w}^H\mathbf{x}(t) = \|\mathbf{a_r}\|\,\|\mathbf{a_c}\|\cos(\mathbf{a_r},\mathbf{a_c}).r(t) + \|\mathbf{a_c}\|^2.c(t) + \mathbf{w}^H\mathbf{n}(t) \tag{5.2}$$

The oblique projector steering the direction of interest corresponding to the beamforming vector $\mathbf{w}$ and nulling the interference direction defined by $\mathbf{a_r}$ is expressed as (see section 3.3.2):

$$\mathbf{E}_{\mathbf{wa}_r} = \mathbf{w}(\mathbf{w}^H\mathbf{P}^{\perp}_{a_r}\mathbf{w})^{-1}\mathbf{w}^H\mathbf{P}^{\perp}_{a_r} \tag{5.3}$$

with $\mathbf{P}^{\perp}_{a_r} = \mathbf{I} - \mathbf{a}_r(\mathbf{a}_r^H\mathbf{a}_r)^{-1}\mathbf{a_r}^H$. The oblique projection beamforming vector is then defined by:

$$\mathbf{w}^H_{\text{obl}} = \mathbf{w}^H\mathbf{E}_{\mathbf{wa}_r} \tag{5.4}$$

Applied to the data model, the resulting instantaneous signal becomes:

$$\mathbf{w}^H_{\text{obl}}\mathbf{x}(t) = \|\mathbf{a_c}\|^2.c(t) + \mathbf{w}^H_{\text{obl}}\mathbf{n}(t) \tag{5.5}$$

Interference subspace estimation

The interference subspace generated by the vector $\mathbf{a_r}$ has to be estimated in order to build the oblique projector. Since the only data available at the EMBRACE system output is a covariance matrix (crosslet), the Classical Eigen-Value Decomposition technique (see section 4.1.1) was chosen. As the data model involves only one interference, the interference subspace is 1-dimensional. Neglecting the cosmic source ($\mathbb{E}\{r^2(t)\} >> \mathbb{E}\{c^2(t)\}$), the dominant eigenvector of the data covariance matrix is an estimate of the interference steering vector $\mathbf{a_r}$.

The Eigen (or Singular) Value Decomposition computational cost can be reduced using the power method [30]. This method iteratively estimates the singular vectors of a matrix one after the other, from the dominant one to the least relevant one. Figure 5.23 shows the accuracy of the power method accuracy at estimating a dominant eigen vector with regard to the Interference to Noise Ratio and the number of iterations of the method. The performances

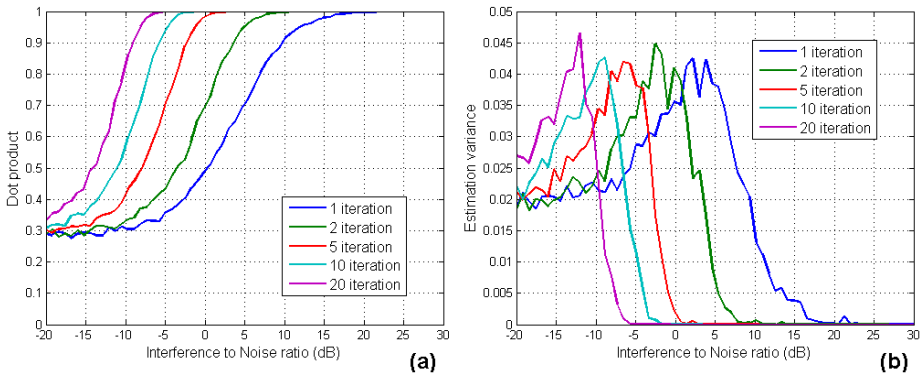

Figure 5.23: Power method performance. (a) Power method dominant eigen vector estimation accuracy. The accuracy is quantified using the dot product between the estimated eigen vector and the true one. This performance is given with regard to the INR and the number of iterations of the power method. (b) Estimation variance with regard to the Interference to Noise Ratio and the number of iterations of the power method.

are quantified using the normalized dot product between the estimated dominant eigen vector and the true one.

The power method is a good way of reducing the cost of a singular value decomposition when only a few singular vectors have to be retrieved. Concerning the EMBRACE system, the implemented algorithm is executed in the Local Control Unit (LCU), which is responsible among other functions for the beamforming vector calculations. This LCU is a computer, and has enough computational power available to perform an eigen value decomposition on a 16×16 crosslet matrix (16 tilesets for the French EMBRACE station).

5.4.2 Implementation

In order to evaluate the performance expected from an RFI mitigation algorithm implementation, we set up an experiment in which an interference is generated, thereby controlling the interfering environment. Figure 5.24.(a) shows the experiment : a home-made antenna has been placed beside the radio telescope. This antenna emits a pure sine signal at a frequency of 1.176 GHz (see Figure 5.24.(b), the signal generator connected to the antenna). This home-made interference is intermittent. At the same time, the radio telescope performs a GPS satellite drift scan in the full frequency bandwidth mode, with a frequency bandwidth centered at 1.176 GHz and 10 MHz wide. Figure 5.25 shows the observation. The first 300 samples correspond to the instrument calibration process. Once done, the observation starts with one crosslet per subband released each second. After 512s, the whole frequency bandwidth has been scanned and the observation starts over at the beginning of the bandwidth. The samples highlighted with red dots are located at the home-made interference frequency. This interference was 'on' during two observation cycles, and 'off' during 4 observation cycles (large peaks when 'on'). Figure 5.26 highlights two spectra observed when the home-made interference is 'on' (in blue) and 'off' (in red).

(a)

(b)

Figure 5.24: Experiment set up. (a) A home-made antenna is placed beside the EMBRACE antenna array in order to emit a controlled interference toward the radio telescope. (b) The antenna shown in (a) is connected to this signal generator. The signal emitted is a pure sine at 1176.45 MHz.

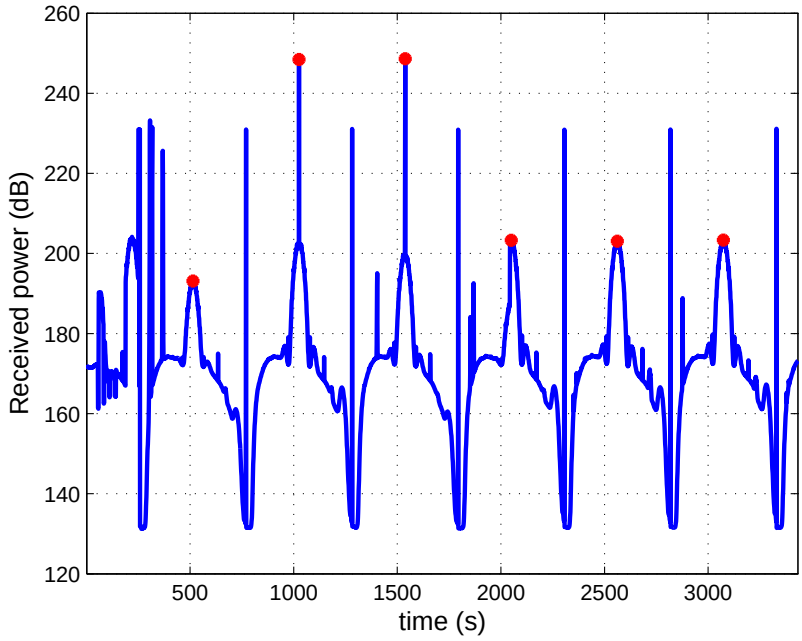

Figure 5.25: GPS satellite drift scan with home-made intermittent narrow band interference.

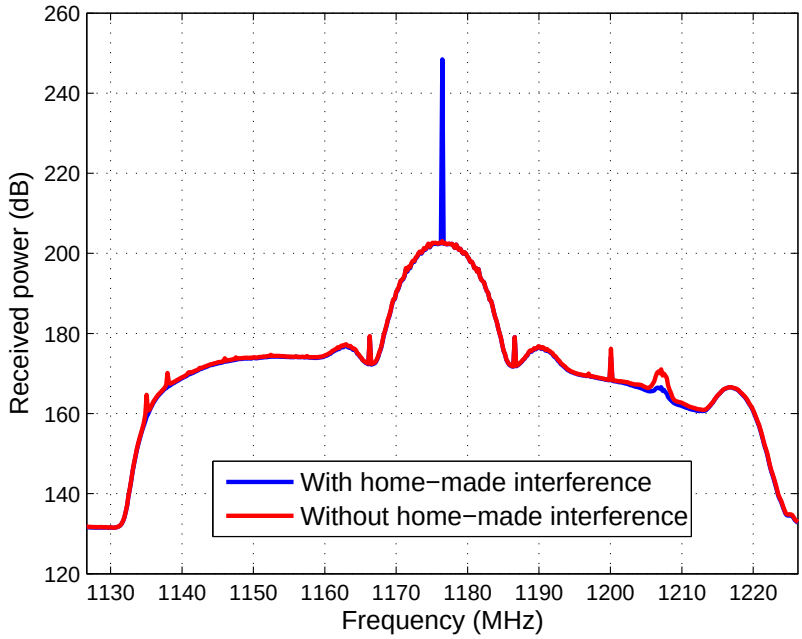

Figure 5.26: Highlight on two spectra observed while the home-made interference is 'on' (blue spectrum) and 'off' (red spectrum).

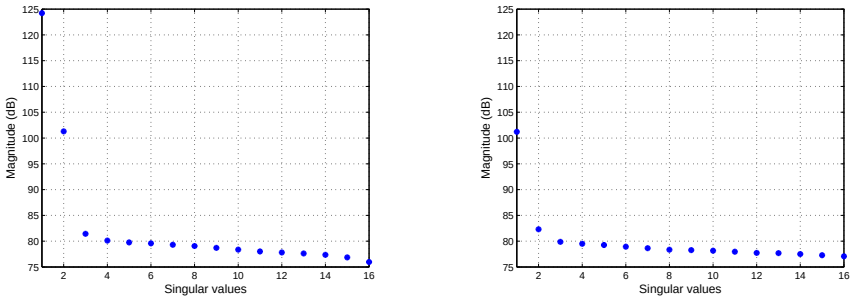

(a) (b)

Figure 5.27: Singular values of two crosslets provided by the system during the observation. (a) Two signals are impinging the radio telescope : the GPS satellite and the home-made interference. The interference subspace is therefore 2-dimensional. (b) Only one interference is impinging the radio telescope (the home-made interference is 'off'). The interference subspace is 1-dimensional.

This observation no longer respects the initial data model given in section 5.4.1 since, depending on the subband considered, more than one interference impinge the radio telescope (GPS satellite and home-made interference or other non-controlled interferences). The interference subspace dimension can be estimated by analyzing the singular values of the crosslets. Figure 5.27 shows the singular values of two crosslets. Figure 5.27.(a) shows the singular values of the crosslet corresponding to the second red star on Figure 5.25, whereas the Figure 5.27.(b) shows the singular values of the crosslet calculated one second later, i.e. the next subband processed. It is clear that the interference subspace is 2-dimensional in the first case since 2 singular values dominate the other 14. In the second case, only one singular value is dominant, and it corresponds to the GPS satellite.

Figure 5.28 shows all the singular values of all the crosslets provided by the EMBRACE back end during the observation. Each of them contributes either to the GPS satellite signal only, the GPS satellite and another interference (home-made or not), or to the system noise.

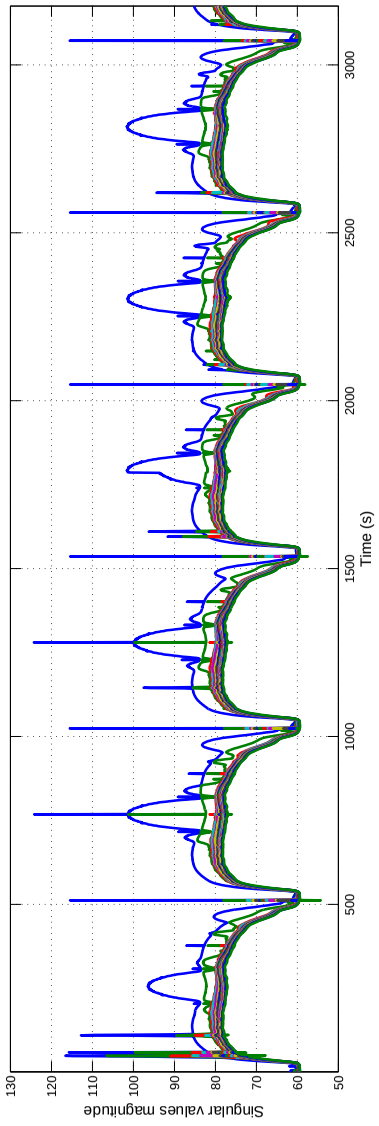

Figure 5.28: Singular values of the crosslets released by the EMBRACE back end during the observation.

The interference subspace dimension cannot, therefore, be a constant parameter of the algorithm; it has to be estimated. Figures 5.29 and 5.30 show the effect on the data after projecting 1 (Figure 5.29) or 2 (Figure 5.30) dimensions out using the orthogonal and the oblique projector. The direction of interest chosen for these tests is the center of the analog beam, i.e. $\mathbf{w} = \mathbf{1}$. The green graphs on both figures are the received power without any processing. The blue graphs correspond to the data obtained after orthogonal projection using either a 1- or 2-dimensional interference subspace, and the red graphs correspond to the same setup with the oblique projector.

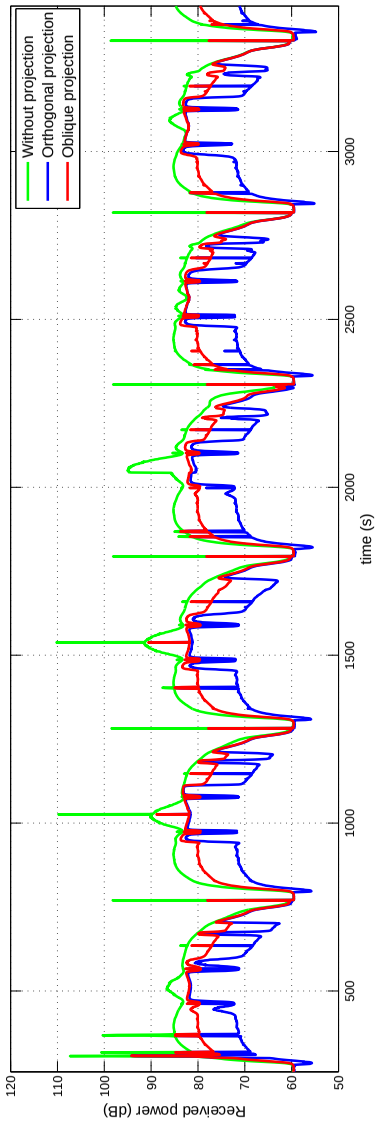

Figure 5.29: Orthogonal and oblique projections projecting a 1-dimensional RFI subspace. In green, the data recovered after beamforming in the direction of the center of the analog beam. In blue, the same results applying an orthogonal projection. In red, the same results applying an oblique projection. The interference subspace is estimated using the dominant singular vector of each crosslet.

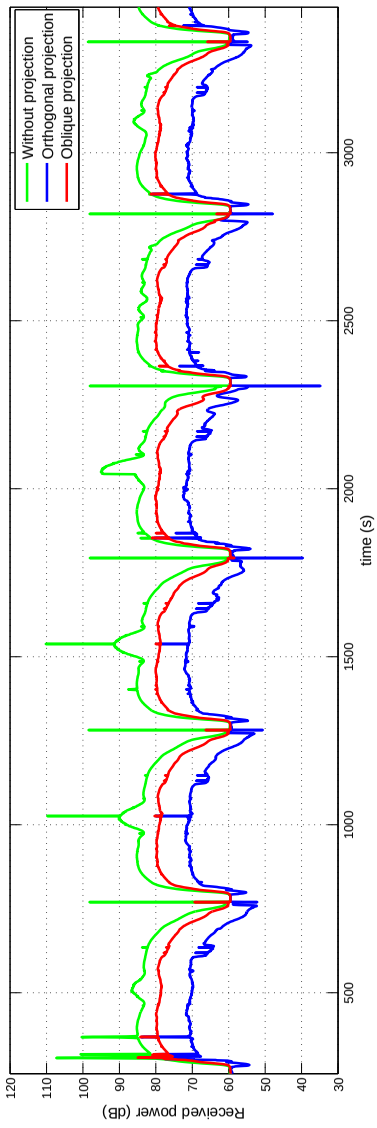

Figure 5.30: Orthogonal and oblique projections projecting a 2-dimensional RFI subspace. In green, the data recovered after beamforming in the direction of the center of the analog beam. In blue, the same results applying an orthogonal projection. In red, the same results applying an oblique projection. The interference subspace is estimated using the two dominant singular vectors of each crosslet.

The discontinuities on these graphs are due to the variation, depending on the subband processed, in the interference subspace dimensionality.

Estimating the number of interfering sources, equivalent to the interference subspace dimension, is necessary in order to apply accurate processing onto the data. This problem has been adressed in different ways [9], and the two most popular techniques for estimating this value are based on information theoretic criteria : the Minimum Description Length (MDL) and the Akaike Information Criterion (AIC) [101, 72, 66].

An implementation of the oblique projector for interference mitigation is suitable for EMBRACE, regarding its back end architecture and computational power. Although the oblique projector can be implemented at the post correlation stage of the signal path, its construction requires the definition of a range subspace, i.e. a particular direction of interest. That is the reason why implementing this projector would be much more efficient in a beamforming application (at the pre-correlation stage).

It has been seen previously that the interference subspace of an observation varies, depending on the frequency subband observed and on the interference environment. Many different ways of estimating this subspace exist, but, according to the data type provided by the system, the classical eigen value decomposition applied on a crosslet matrix is the only possible choice. The eigen or singular values of these matrices allow the interference subspace dimension estimation, with the MDL criterion for instance, whereas its eigen or singular vectors allow the estimation of a basis of it.

However, the EMBRACE back end is built in such a way that all the observation parameters stay constant over the integration time (1 second). Applying any correction to the digital beamforming vector is therefore impossible in real time. Building the oblique projector requires a crosslet to be already available. Since the back end releases one crosslet per second, the oblique projector has to be built as soon as the latest crosslet has been released and applied to the beamforming vector at the next observation of the same frequency subband.

Since most of the interferences are moving objects, implementing this algorithm in the full bandwidth observation mode would be useless. The crosslet provided by the system could be used to build a projection, but this projector would only be applied 8 minutes and 32 seconds later, i.e. once the whole frequency bandwidth had been scanned.

The single frequency subband observation mode is a good candidate since the corrections would be applied within the second after the latest crosslet has been released.

Figure 5.31 is a graphical representation of the algorithm implemented on the EMBRACE back end (except the shaded part of the diagram concerning the RFI subspace dimension estimation). Once the latest crosslet matrix has been released, the interference subspace is estimated with a singular value decomposition applied to this matrix. The interference subspace estimate is then used to build an orthogonal projection matrix. With this projection matrix and the beamforming vector calculated by the system back end, an oblique projector is built. The beamforming vector is finally multiplied with the oblique projector to give a corrected beamforming vector. This corrected beamforming vector is then applied in the same way as the initial beamforming vector to the antenna array output.

Figure 5.32 shows a simulation with real data of the full algorithm as it runs

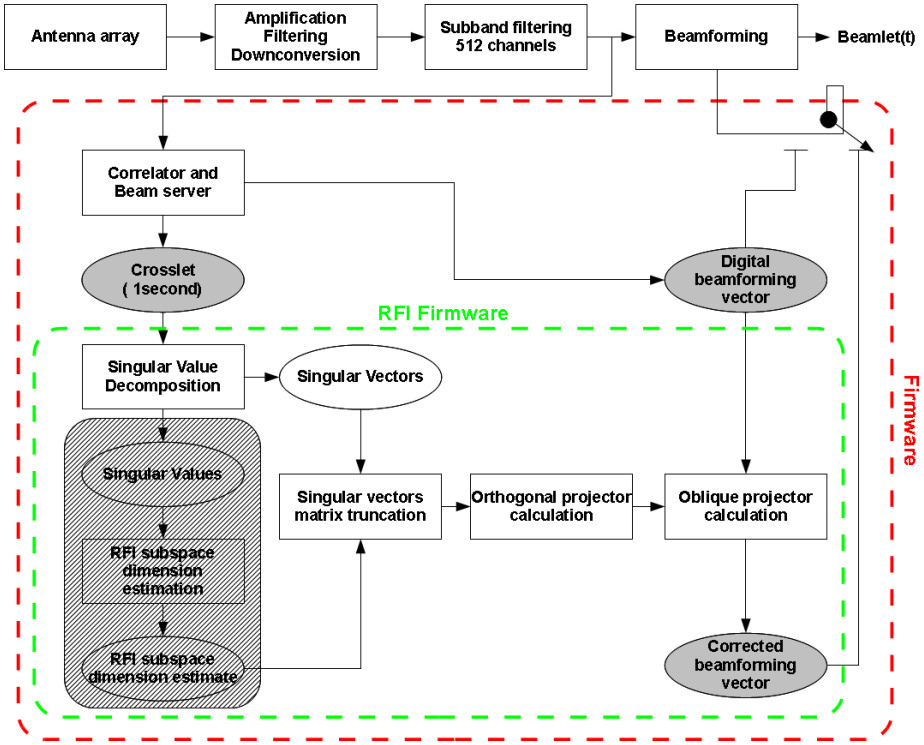

Figure 5.31: RFI mitigation algorithm implementation. The EMBRACE back end provides a crosslet matrix each second and calculates a digital beamforming vector to be applied after the analog beamforming stage. The oblique projection algorithm is based on both data and provides a corrected beamforming vector.

on the EMBRACE back end. The green graph is the received power while a GPS satellite is crossing the analog beam of the system. The direction of interest, defined by the digital beamforming vector, is the analog beam center. The black graph shows the corrected data, after building an oblique projector. The interference subspace has been estimated with a crosslet provided by the system 4 seconds before the correction was applied, its dimension was set to $\hat{N}_r = 2$. In comparison, the red graph shows the corrected data when the interference subspace is estimated at the same time the correction is applied (as it could be done offline). The jitter between ≈ 1500 and ≈ 2200s on the corrected signals corresponds to the time when the satellite reaches the direction of interest. The algorithm then tries to mitigate and recover the signals coming from the same direction. No signal can therefore be recovered during this time slot.

The red and black graphs do not show a marked difference out of this time slot. The interference subspace seems constant enough at a small time scale (≈ 4s) for the algorithm to be efficient when the corrections are applied after the interference subspace has been estimated.

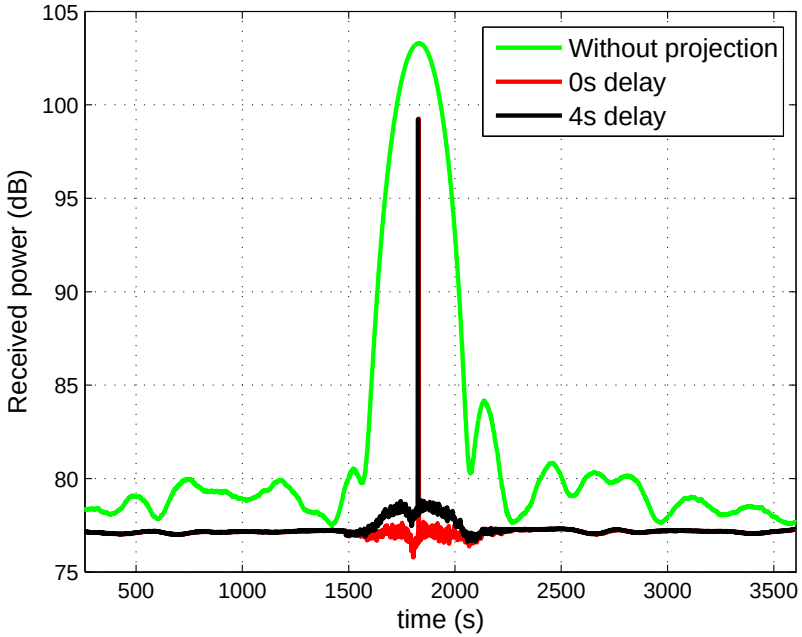

Figure 5.32: RFI mitigation algorithm implementation. In green, the received power while a satellite is crossing the analog beam (digital beam steering the analog beam center). In red, the received power after oblique projection, interference subspace estimated with the crosslet on which it has been applied. In black, the received power after oblique projection, interference subspace estimated with a crosslet calculated 4 seconds before the projector is applied.

5.5 Conclusions on RFI mitigation implementation

Different assumptions are made while developing an algorithm. Implementing it on a real system requires first of all the validation of these assumptions. Without these validations, the theoretical and real performance of an algorithm cannot be compared.

The usual assumptions made in spatial filtering applications concern the antenna array calibration and noise coupling, the narrow band property of the signals impinging the array and, in radio astronomy, the negligible signal strength of the source of interest (cosmic source).

In a first approach, the aim of the implementation made on the radio telescope EMBRACE was to demonstrate the possibility of incorporating a real time interference mitigation process into the system signal path. Quantifying the interference attenuation is also another important point in this project.

When cosmic sources are no longer negligible, the most accurate interference subspace estimation technique would require a lower level implementation on the system by, for example, allowing cyclostationary or time-lagged covariance matrices calculations.

The data provided by EMBRACE are however suitable for an interference mitigation algorithm. The crosslet matrices contain all the statistical information about the sources impinging the array, and particularly the interference. Once the interference subspace has been estimated, a beamforming vector nulling them can be set at the antenna array output.

The algorithm presented in this chapter has been implemented on one beam of the radio telescope EMBRACE. Different scenarii were selected to evaluate its performances on the radio telescope by observing simultaneously the same direction with one corrected beam and another beam without any processing. The algorithm performance cannot, however, be easily quantified since there is no comparison possible between processed corrupted data and interference-free data.

Chapter 6

Conclusions and Future work

6.1 Conclusions

This thesis addresses spatial interference mitigation for phased antenna array radio telescopes.

After building an antenna array data model, based on assumptions regarding the different signals impinging the radio telescope, spatial filtering techniques are introduced. Popular beamforming techniques are briefly discussed, then projection approaches are presented. The concept shared by both the orthogonal and oblique projectors is to project the interference subspace out of the antenna array data vector space. Figure 3.10 particularly shows that in a noise-free model, the oblique projector is able to perfectly recover the source of interest, whereas the performance of the orthogonal projector depends on the orthogonality between the interference and source of interest subspaces. In terms of RFI rejection and SOI gain after processing, projection techniques are preferable to beamforming techniques, as shown on Figure 3.13.

An interference subspace subtraction technique is also introduced. As long as the different assumptions regarding the data model hold (additive model, interference spatial signatures perfectly known...), this technique shows good results.

The signals' spatial signatures, especially for RFI, are considered as unknown for two reasons : there is no a priori information about the interfering environment, and the antenna array is considered as being uncalibrated. In general, blind approaches are preferred in radio astronomy for these reasons. Their estimation remains however an important stage of a spatial RFI mitigation algorithm. Depending on the technique, the estimation can concern the individual RFI spatial signatures, or the basis spanning the RFI subspace.

RFI subspace estimation is addressed in Chapter 4. Based on RFI statistical parameters, three covariance matrices are of interest : the classical covariance matrix, the cyclic and conjugate cyclic covariance matrix, and the time-lagged covariance matrix. In a first approach, the RFI subspace is estimated based on a single matrix. In a second approach, multiple covariance matrix techniques are suggested. Figure 4.9 shows that an ALS-based joint diagonalization applied

to multiple time-lagged covariance matrices is the most accurate among all the RFI subspace estimation techniques presented in this thesis.

Finally, real data processing is presented in the last chapter. The first section shows results of most of the techniques presented in this thesis applied offline to LOFAR Low and High Band Antenna data. Results on LBA data are graphically convincing, especially concerning the time-lag RFI subspace estimation technique (see Figure 5.3) and the oblique projection and RFI subspace subtraction approaches (see Figures 5.7 and 5.8).

The second section presents an RFI mitigation algorithm implementation. The implementation was conducted on the radio telescope demonstrator EMBRACE. Based on the data available at the system output, the (single) classical covariance matrix approach was chosen in order to estimate the interference subspace. Once estimated, this subpace and a direction of interest were used to build an oblique projector, and then a corrected beamforming vector. Preliminary tests on GPS satellite drift scans show that the algorithm response is in accordance with the expected response (see Figure 5.32 for example).

6.2 Future work

In a corrupted radio-environment, the main goal of RFI mitigation for radio astronomy is to perfectly recover astronomical sources. Most of the interference mitigation techniques are compared with respect to their RFI attenuation (or rejection) performance, but not necessarily with respect to their performance in recovering the Signal-Of-Interest. Generalized performance criteria need however to be set in this way, since perfectly recovering the signal of interest remains the main goal.

The data model introduced in this thesis assumes several signal characteristics. For instance, the system noise is assumed to be uncorrelated. This assumption no longer holds for dense aperture arrays, when antenna elements are too close to each other for mutual coupling to be neglected. Whitening can be applied to antenna array output data, in order to make the noise covariance matrix diagonal. However, investigating spatial filtering techniques in the case of non-diagonal noise covariance matrices could improve the practical performances of current approaches. Another example concerns the interference multipath effect. Neglecting this effect leads to assuming that the RFI covariance matrix is diagonal. Depending on the assumptions made on the data model, interference subspace estimation based on diagonalization might not provide accurate enough estimates in the case of RFI multipath. Non-diagonal matrix transformation, like triangularisation, should also be investigated.

The performance of an RFI mitigation algorithm depends not only on the spatial filter performance, but also on the interference subspace estimation accuracy. Subspace tracking techniques, for example, would highly improve their performances. For fixed RFI, the estimation would practically be more accurate due to a longer integration time compared to techniques based on covariance matrices released by the system (1 second for EMBRACE). For moving RFI, interference spatial signature prediction would increase the performance of RFI mitigation algorithms when applied in real time.

Spatio-temporal filtering techniques have already been studied in different fields. Applied to radio astronomy, their use could also improve the perfor-

mances of current spatial filtering approaches, particularly by considering the frequency dependence of spatial signatures inside an antenna array frequency subband.

Chapter 7

Summary in French

7.1 Introduction

La radioastronomie est une science datant des années 1930. Karl Jansky, ingénieur pour les laboratoires Bell, a été le premier observateurs d'ondes électromagnétiques provenant de sources cosmiques. Dans son cas, il s'agissait du centre de notre galaxie, la Voie Lactée. Les émissions dans le domaine radio des sources cosmiques sont classifiées spectralement en deux grandes catégories:

- Les émissions 'continuum', qui sont large bande et dont l'origine peut être thermique ou synchrotron.
- Les lignes spectrales, qui sont des émissions à bande étroite et dépendante principalement de la composition de l'astre. Le mouvement et l'expansion de celui-ci, par exemple, peuvent être identifiés au travers de l'analyse du pic spectral (décalage et largeur).

D'un point de vue temporel, les émissions radio astronomiques sont classifiées en émissions continues ou transitoires pour les pulsars par exemple.

Les instruments utilisés pour capter ces émissions ayant parcourues des années lumières se doivent d'être extrêmement sensibles. On distingue deux types de radiotélescopes:

- Les télescopes paraboliques, dont la résolution est fonction du diamètre de la parabole et de la longueur d'onde observée.
- Les réseaux d'antennes phasés, dont la résolution est fonction de la ligne de base maximum (distance maximale entre deux antennes du réseau) et le longueur d'onde observée.

De plus, d'autres architectures mélangeant les deux types précédent existent, comme les réseau de radio télescopes paraboliques ou les réseaux d'antennes phasés substituant les récepteurs de radiotélescopes paraboliques.

Les radiotélescopes de type réseau d'antennes phasés ont deux types de fonctionnement possibles:

- Réseau d'antennes phasés, permettant la formation de faisceaux et donc de multiples observations simultanées dans de multiples directions dans le ciel sans mouvement mécanique.

- Interféromètre (ou synthèse d'ouverture), permettant l'imagerie radio du ciel suivant le théorème de Van Cittert-Zernike liant la corrélation entre éléments du réseau à la distribution spatiale de la puissance reçue.

La radioastronomie ne s'étend pas sur tout le domaine radio pour des raisons d'opacité de l'atmosphère et de l'ionosphère à certaines fréquences. Cependant, certaines bandes de fréquences sont protégées et destinées à la radioastronomie. Ces allocations sont historiques et correspondent à des fréquences d'émissions et d'absorptions (lignes spectrales) d'éléments bien connus. Pour diverses raisons (e.g. décalage en fréquence des lignes spectrales), les astrophysiciens souhaitent réaliser des observations en dehors de ces bandes protégées. Légalement, ceci est autorisé tant que l'utilisation du spectre électromagnétique reste passive, ce qui est le cas. Cependant les bandes non protégées sont en général allouées à d'autres utilisateurs actifs (systèmes de télécommunications par exemple). Les observations astronomiques se retrouvent donc polluées par des interférences (RFI). En réalité, même les bandes protégées peuvent être polluées par des utilisateurs actifs non autorisées, par exemple dans le cas de filtres d'émissions mal dimensionnés ou des produits d'intermodulations faisant apparaître des harmoniques dans ces bandes.

Le traitement d'interférence est donc nécessaire pour la radioastronomie. Le premier de ces traitements est l'isolation des radiotélescopes dans des régions du globe à faible densité de population. Mais le silence radio est rarement possible, du aux fréquentes émissions spatiales et aéronautiques (géo-positionnement, applications militaires, transpondeurs spatiaux...). Distinguer la source cosmique d'intérêt et le signal interférant est une nécessité pour le traitement d'interférences. La parcimonie dans le plan Temps-Fréquence d'une observation, lorsqu'elle existe, permet une excision de l'interférence au travers de filtres fréquentiels, ou de masquage temporel pour les événements impulsionnels. Lorsque la distinction entre signal d'intérêt et interférence n'est pas possible dans le plan Temps-Fréquence, c'est la diversité spatiale qui peut être exploitée. Les radiotélescopes paraboliques l'exploitent partiellement puisqu'ils sont directifs. Cependant, leur lobes secondaires sont fixes et ne permettent pas d'atténuation adaptative en fonction de la direction du pollueur. En revanche, les radiotélescopes à réseaux d'antennes phasés sont appropriés pour ce type de traitement. Les techniques de beamforming adaptatif, ou filtres spatiaux, ont été largement étudiés par le passé, principalement grâce à l'essor de ce type de système pour les télécommunications.

C'est dans ce dernier cadre que se situe cette thèse. Après la dérivation d'un modèle de données pour les radiotélescopes à réseaux d'antennes phasés, les techniques de filtrage spatial sont abordées. Deux techniques, la projection oblique et la soustraction de sous espace RFI sont introduites. Puisque la mise en œuvre d'un filtre spatial nécessite une information liée à l'interférence, un chapitre est consacré à l'estimation de sous-espace RFI. Notamment, l'exploitation de paramètres statistiques liés aux RFI est introduite pour produire cette estimation. Un dernier chapitre illustrera les différentes techniques présentées dans cette thèse au travers de résultats sur des données astronomiques produites par le radiotélescope Européen LOFAR. De plus, une implémentation d'un algorithme de traitement d'interférences sur le démonstrateur EMBRACE est également présentée dans ce chapitre.

7.2 Modèle de données

Ce chapitre dérive un modèle de données pour les radiotélescopes à réseaux d'antennes phasés. Le réseau, de distribution spatiale arbitraire, est composé de M antennes. Chaque antenne possède son propre gain complexe et son propre terme de bruit (bruit système), et reçoit les contributions de chacune des N_s sources situées dans le champ de vue du télescope. On suppose $Ns = N_c + N_r$, avec N_c le nombre de sources cosmiques et N_r le nombre de sources d'interférences (voir équation 2.1). Du à la propagation des ondes dans le réseau, chaque antenne perçoit les mêmes signaux avec un décalage temporel lié à la fois à la forme du réseau et à la direction d'arrivée de l'onde. Ce décalage temporel est relatif à un point (de l'espace) de référence, qui peut également être l'une des antennes du réseau.

La première hypothèse établie est l'hypothèse bande étroite (section 2.2.1). Chacun des signaux reçu par le réseau d'antennes est supposé occuper une bande de fréquence suffisamment étroite (par nature ou par filtrage) de façon à ce que les décalages temporels soient exprimés par des décalage de phase. Une seconde hypothèse établie dans ce chapitre est l'hypothèse de champ lointain (section 2.2.2). Les sources des ondes électromagnétiques reçues par le télescope sont supposées suffisamment distantes de celui-ci, de sorte à ce que leur front d'onde puisse être considéré comme plan.

Le bruit système est constitué d'une somme de multiples termes de bruits indépendants tout au long de la chaîne de traitement. Par application du Théorème Central Limite, ce bruit est modélisé par un processus centré, blanc, indépendant et identiquement distribué (iid) avec une distribution Gaussienne complexe. La non stationnarité de certaines composantes (e.g. cycles jours/nuit) fait que ce bruit n'est pas stationnaire. Cependant, sur de courtes durées d'observations (de l'ordre de, ou inférieure à la seconde), ce bruit peut être modélisé par un processus stationnaire.

Les sources cosmiques émettent naturellement des ondes radio. Ces émissions sont dues à un grand nombre de phénomènes aléatoires et, de fait, par application du Théorème Central Limite, les signaux cosmiques sont modélisés par des processus centrés, blancs, iid de distribution Gaussienne complexe. Outre certaines sources particulières comme les pulsars, les émissions cosmiques sont stationnaires. Cependant, de lentes variations atmosphériques et dans le medium interstellaire causent également de lentes variations dans les statistiques de ces processus lorsqu'elles atteignent le télescope. A nouveau, sur de courtes durées, ces variations peuvent être négligées et ces processus sont donc considérés stationnaires.

Les interférences peuvent être de multiples natures. Le terme interférence englobe tout signal n'étant pas le signal d'intérêt. Orages, modulation d'amplitude dus aux systèmes éoliens ou émissions provenant de lignes haute tension sont différents exemples d'interférence pour la radioastronomie. Cette thèse s'intéresse particulièrement aux signaux modulés d'origine humaine.

Hypothèse supplémentaire, toutes les sources (cosmiques ou d'interférence) sont supposées indépendantes entre elles et indépendantes du bruit système.

La sortie d'un réseau d'antennes phasées s'écrit sous forme vectorielle où chacune des composantes de ce vecteur de sortie est la sortie de chacune des antennes du réseau (equation 2.12). Le modèle vectoriel est additif, et chacune des sources est liée à un vecteur, appelé vecteur de signature spatiale, corre-

spondant donc aux coefficients complexes décrivant la propagation de leur onde au travers du réseau (hypothèse bande étroite). Les gains complexe de chacune des antennes sont également incorporés dans ces vecteurs. De plus, le terme de bruit système est décrit par un vecteur de bruit où chaque composante est une variable aléatoire centrée, blanche, iid de distribution Gaussienne et stationnaire.

Puisque l'indépendance entre toutes les sources et le bruit système est supposée, le modèle matriciel de covariance des données est également additif (equation 2.14). Il est donc possible d'identifier une sous-matrice de covariance des sources cosmiques, une sous-matrice de covariance des RFI et une sous-matrice du bruit système.

La plupart des signaux de télécommunications étant cyclostationnaires, cette propriété est introduite en section 2.4.2. Cette propriété est importante puisqu'elle permet d'isoler les contributions des interférence par rapport aux sources cosmiques et au bruit système.

7.3 Filtrage spatial

Les techniques classiques de traitement d'interférences en radioastronomie consistent à surveiller un ou plusieurs paramètres statistiques de l'observation, et détecter puis exciser dans le plan Temps-Fréquence les canaux fréquentiels ou temporels corrompus. Lorsque interférence et signal d'intérêt partagent les même canaux, ces traitements deviennent inutiles. L'information spatiale peut cependant pousser le traitement plus loin en atténuant des directions d'arrivées correspondant aux RFI. Les réseaux d'antennes phasés ont fait l'objet d'une attention particulière ces dernières années puisqu'ils permettent de facilement contrôller la réponse du système de sorte à atténuer certaines directions de visée. Ce traitement est appelé beamforming, ou formation de faisceaux. Quatre techniques de beamforming sont présentées en section 3.2: beamforming classique, Multiple Sidelobe Canceller, Maximum SNR et LCMV. Ces techniques font intervenir l'information spatiale des données au travers de la matrice de covariance du réseau. L'atténuation atteinte avec ce type de traitement est similaire aux filtres numériques à Réponse Impulsionnelle Finie.

Un autre type de traitement spatial fait intervenir les projections. La première projection présentée dans ce chapitre est la projection orthogonale (voir section 3.3.1). Le principe de cette technique est de visualiser un espace vectoriel M-dimensionnel, correspondant à l'espace de l'observation. Cet espace vectoriel est constitué de plusieurs sous-espaces:

- sous-espace sources cosmiques,
- sous-espace RFI
- sous-espace bruit

Ces sous-espaces ne sont cependant pas nécessairement supplémentaires puisque le bruit système est spatialement blanc. La projection orthogonale consiste à projeter les données de l'observation parallèlement au sous-espace RFI, sur un sous-espace orthogonal et supplémentaire à ce même sous-espace RFI. La contribution des interférences est donc annulée. Cependant, la projection orthogonale

'déforme' l'espace vectoriel des observations, excepté le sous-espace orthogonal au sous-espace RFI (voir illustration 3.8).

Pour corriger cet effet, l'utilisation de la projection oblique pour le traitement des interférences est introduite en section 3.3.2. Le concept de cette technique reste le même que la projection orthogonale. La projection se fait toujours parallèlement au sous-espace RFI, mais sur le sous-espace sources cosmique, ou plus particulièrement sur le sous-espace correspondant à la source cosmique d'intérêt (voir illustration 3.9). La construction de ce projecteur nécessite à la fois une information correspondant au sous espace RFI et une information correspondant à la source cosmique d'intérêt. De construction plus complexe que la projection orthogonale, ce projecteur permet toutefois la récupération de la source cosmique sans biais. Pour le projecteur orthogonal, l'erreur sur la source après traitement est dépendante du produit scalaire entre la source cosmique et le sous-espace RFI.

Tant que le modèle de données reste additif et que l'indépendance entre sources et bruit système est valide, il est également envisageable de considérer une technique basée sur la soustraction de sous-espace RFI, comme présenté en section 3.4. Cette technique consiste à annuler la puissance atteinte dans une direction définie par un vecteur de signature spatial (qui ne correspond donc pas nécessairement à une réelle direction de visée.) En estimant les signatures spatiales de chacun des brouilleurs individuellement, cette technique permet leur annulation du point de vue des données observées.

Ce chapitre présente plusieurs techniques de filtrage spatial basées sur la connaissance du sous-espace RFI (hormis les techniques de beamforming qui se basent en général sur la matrice de covariance du réseau en général). Le sous-espace RFI est supposé connu pour le moment, mais en réalité la première étape d'un algorithme de traitement spatial d'interférence consiste à l'estimer. C'est le thème adressé par le chapitre suivant.

7.4 Estimation de sous-espace RFI

La connaissance du sous-espace RFI est nécessaire pour appliquer un traitement spatial d'interférence. La précision de l'estimation correspond généralement à la limite de performance d'un tel algorithme.

La première partie de ce chapitre traite de trois différents types de matrices de covariance et de leur utilisation dans l'estimation de sous-espace RFI.

Le premier type de matrice est la matrice de covariance classique (section 4.1.1). Lorsque les sources cosmiques sont négligeables et la matrice de covariance du bruit est diagonale (couplage entre antennes négligé), une décomposition en valeurs propres de cette matrice permet d'identifier deux sous-espaces en somme directe : le sous-espace RFI et un sous-espace bruit. Lorsque le système est calibré, le bruit système pour chaque antenne est le même. De fait, l'identification du sous-espace RFI se fait par identification des valeurs propres dominantes (et non-constantes) de la matrice de covariance. Les vecteurs propres correspondant à ces valeurs propres forment une base du sous-espace RFI. Cette technique est simple à mettre en œuvre, mais les hypothèses faites sur le modèle de données sont trop contraignantes.

La deuxième technique présentée est basée sur une matrice de covariance cyclique (section 4.1.2). Cette fois, la propriété de cyclostationnarité au sec-

ond ordre d'une interférence est exploitée pour isoler l'interférence des sources cosmiques et du bruit système. La matrice calculée ne contient d'information qu'au sujet des processus α-cyclostationnaires des données observées. Il ne s'agit que de l'interférence. Idéalement, les valeurs singulières de cette matrice sont non-nulles pour le sous-espace RFI (puissance cyclique à la fréquence cyclique α) ou nulles. Les vecteurs singuliers correspondant aux valeurs singulières non-nulles forment donc à nouveau une base du sous RFI dans le cas d'une seule RFI α-cyclostationnaire, ou uniquement la signature spatiale d'une RFI α-cyclostationnaire. Cette technique requiert toutefois la connaissance de la fréquence cyclique de l'interférence considérée (pouvant être obtenue en calculant un spectre cyclique de l'observation), et le calcul de N_r matrices de covariance cyclique pour N_r RFI de fréquences cycliques différentes.

La troisième technique présentée est basée sur une matrice de covariance classique décalée de $\tau \neq 0$. La blancheur des sources cosmiques et du bruit système implique que leur covariance à $\tau \neq 0$ est nulle. Les interférences véhiculent en général une information, et ne sont donc pas des processus blancs. A nouveau, une décomposition en valeur singulière de cette matrice permet d'isoler le sous-espace RFI des autres sous-espaces (sources cosmiques et bruit système), et donc de l'estimer de la même manière que pour la matrice de covariance cyclique. Cette technique permet d'identifier le sous-espace RFI au complet avec une seule matrice.

Une deuxième partie de ce chapitre (section 4.2) présente des techniques de diagonalisation conjointe, permettant donc de faire intervenir plusieurs informations (par exemple, plusieurs matrices de covariance cyclique calculées pour différentes fréquences cycliques).

Une troisième partie du chapitre (section 4.3) présente des techniques de haute résolution. Ces techniques consistent à définir une fonction de contraste, puis identifier les différents maxima de cette fonction sur un intervalle de définition (le champ de vue de l'instrument en général). Ce type de technique n'est pas adapté à la radioastronomie puisque le coût de calcul de l'optimisation de telles fonctions est important. De plus, les sous-espaces RFI ne correspondent pas nécessairement à des directions d'arrivée spatiales (lobes secondaires).

7.5 Implémentation d'un algorithme de traitement d'interférences

Ce chapitre présente les résultats des traitements présentés dans cette thèse, appliqués à des données acquises avec une station néerlandaise du radiotélescope Européen LOFAR. Le premier exemple traite une acquisition faite à 55 MHz, corrompue par une interférence de type communication de véhicule terrestre. Les cartes du ciels montrent le champ de vue complet de l'instrument. L'interférence est située à l'horizon. De plus, deux puissantes sources cosmiques sont visibles à plus haute élévation. L'interférence est cyclostationnaire, comme peut être vu sur la figure 5.2, et la figure 5.3 montre l'approche décalage temporel (τ) mettant en évidence la blancheur des sources cosmiques contrairement à l'interférence. Les approches haute résolution sont également présentées sur les figures 5.4 et 5.5. Respectivement, le projecteur orthogonal et le projecteur oblique, ainsi que la soustraction de sous-espace RFI sont également présentés sur les figures

5.6, 5.7 et 5.8. Les mêmes traitements ont ensuite été appliqués à des données acquises dans une bande de fréquence supérieure (109.28 MHz), corrompues par un signal d'aviation.

La deuxième partie de ce chapitre (section 5.3) présente une implémentation d'un algorithme de traitement spatial d'interférences basé sur la diagonalisation de la matrice de covariance classique pour l'estimation du sous-espace RFI et sur un projecteur oblique. Cette implémentation a été effectuée sur une station du démonstrateur EMBRACE, dont la chaîne de traitement est similaire à celle d'une station LOFAR bien que les fréquences d'observation diffèrent. Après une présentation succinte du système, l'algorithme proposé est développé. L'estimation de sous-espace RFI n'a pu être basée que sur la matrice de covariance classique du réseau car la reconfiguration du système pour incorporer les aspects cyclostationnaires ou décalage temporel n'était pas possible. Le choix d'une implémentation temps-réel est dictée par le mode de fonctionnement de l'instrument (scan de bande de fréquence complète ou scan de canal de fréquence unique voir figures 5.20 et 5.21). Dans le cas du mode bande de fréquence complète, la projection ne peut être appliqué aux données que 512 secondes après avoir estimé le sous-espace RFI. Un traitement offline est donc plus avantageux dans ce cas car le sous-espace RFI est susceptible de grandement évoluer en 512s. Dans le cas du fonctionnement simple canal fréquentiel, la projection est appliquée au maximum 4 secondes après l'estimation du sous-espace RFI. Une implémentation temps-réel est réalisable dans ce cas comme le montre la figure 5.32.

Le problème de l'estimation automatique de la dimension du sous-espace RFI n'a cependant pas été abordée. La dimension de ce sous-espace est donc fixée à 2.

7.6 Conclusion

Cette thèse s'intéresse au traitement spatial des interférences pour les radiotélescopes à réseaux d'antennes phasés. Après avoir modélisé les données issues d'un réseau d'antennes partant d'hypothèses faites sur les natures des signaux, le filtrage spatial est abordé. Les techniques classiques de beamforming ainsi que les projections orthogonale et oblique sont présentées et comparées. Ces deux dernières techniques offrent de meilleures réjections que le beamforming (voir figure 3.13), mais la projection orthogonale atténue également le signal d'intérêt suivant l'angle entre ce signal et le sous-espace RFI contrairement à la projection oblique. Une technique basée sur la soustraction du sous-espace RFI est également présentée et montre de bons résultats. Cependant elle nécessite la connaissance des vecteurs de signature spatiale de chacun des brouilleurs.

Le sous-espace RFI est inconnu et nécessite une estimation. Certaines techniques présentées dans cette thèse permettent une estimation d'une base de ce sous-espace, tandis que d'autres permettent l'estimation des vecteurs de signature spatiale de chacun des brouilleurs individuellement. Les méthodes introduites sont basées sur les paramètres statistiques des interférences permettant de les distinguer des sources cosmiques et du bruit système afin d'améliorer la précision de l'estimation.

Enfin, une implémentation d'algorithme de traitement spatial temps-réel des interférences est proposée en section 5.3.

Le traitement d'interférences pour la radioastronomie deviendra de plus en plus important au vue de l'occupation croissante du spectre électromagnétique par des applications humaines. Diverses pistes peuvent néanmoins être encore explorée, comme le suivi de sous-espace RFI ou les traitements spatio-temporels. Les hypothèses faites sur les signaux peuvent également être affinées afin de prendre en compte le couplage entre les antennes d'un réseau ou les trajets multiples des interférences.

Appendix A

Multipath effect and rank analysis

Any emitted electromagnetic wave can be subjected to multiple reflections, and therefore impinge an antenna array radio telescope multiple times. While receiving one (or more) signals from an (arbitrary) primary emitter, the array also receives a time-shifted copy of this signal.

Cosmic sources are uncorrelated by nature (see section 2.2.3). The cosmic sources covariance matrix $\mathbf{R_c}(t,\tau)$ is therefore assumed to be diagonal (i.e. $\mathbb{E}\{c_n(t+\frac{\tau}{2}){c_m}^*(t-\frac{\tau}{2})\}=0$ for $i\neq j$, $\forall\tau$).

However, RFI signals are easily subjected to multi paths propagations. Consider the following narrowband interference-only data model:

$$\mathbf{x_r}(t)=\sum_{n=1}^{N_r}\left(\sum_{m=1}^{M_n}\mathbf{a}_{r_{n,m}}(t,\theta_{r_{n,m}},\phi_{r_{n,m}})r_n(t-\tau_{n,m})\right) \tag{A.1}$$

We have here N_r uncorrelated interference signals impinging the radio telescope. Each interference $r_n(t)$, $n\in[1\dots N_r]$, is subjected to M_n-1 reflections, and is therefore copied M_n times at the antenna array output as coming from M_n different directions. $\tau_{n,m}$ represents here a time delay caused by the path length difference between an interference signal emitted by a primary emitter and its copy emitted by any reflective device. The $\sum_{n=1}^{N_r}M_n\times\sum_{n=1}^{N_r}M_n$ interference covariance matrix $\mathbf{R_r}(t,\tau)$ related to this data model is then block-diagonal. Its coefficients are defined by:

$\forall\tau, n\in[1\dots N_r], m\in[1\dots M_n]$

$$\sigma^2_{n,n',m,m'}(\tau)=\mathbb{E}\{r_n(t-\tau_{n,m}+\frac{\tau}{2})r^*_{n'}(t-\tau_{n',m'}-\frac{\tau}{2})\} \tag{A.2}$$

with $\sigma^2_{n,n',m,m'}(\tau)=0$ for $n\neq n'$, and $\sigma^2_{n,n',m,m'}(\tau)=\Gamma_{r_n}(t,\tau-\tau_{n,m}+\tau_{n',m'})$ for $n=n'$, with $\Gamma r_n(t,\tau)$ the autocovariance function of $r_n(t)$.

For simplicity, suppose we have only one interference $r(t)$ following 2 different paths. The simplified data model is then expressed by:

$$\mathbf{x_r}(t)=\mathbf{a}_{r_1}(t,\theta_{r_1},\phi_{r_1})r(t)+\mathbf{a}_{r_2}(t,\theta_{r_2},\phi_{r_2})r(t-\tau_{1,2}) \tag{A.3}$$

with $\tau_{1,2}$ the time delay between the two copies of the signal $r(t)$ due to the difference in path lengths.

First, we consider the two path lengths close enough for $\tau_{1,2}$ to be neglected. The two copies of the signal $r(t)$ are then said to be *fully correlated*. We have:

$$\mathbf{x_r}(t) \sim (\mathbf{a}_{r_1}(t, \theta_{r_1}, \phi_{r_1}) + \mathbf{a}_{r_2}(t, \theta_{r_2}, \phi_{r_2}))\, r(t) \tag{A.4}$$

$$\sim \tilde{\mathbf{a}}_r(t, \tilde{\theta}, \tilde{\phi}) r(t) \tag{A.5}$$

The resulting covariance matrix of this model is 2-dimensional since two signals impinge the antenna array. However, its rank is one since its four coefficients are the same.

Now, lets consider the path lengths different enough for $\tau_{1,2}$ not to be neglected. The two signals are said to be *partially correlated*.

With $r_1(t) = r(t)$ and $r_2(t) = r(t - \tau_{1,2})$, we have:

$$\mathbf{R_r} = \begin{bmatrix} \Gamma_{r_1}(t,0) & \Gamma_{r_1,r_2}(t,0) \\ \Gamma_{r_2,r_1}(t,0) & \Gamma_{r_2}(t,0) \end{bmatrix} \tag{A.6}$$

$$= \begin{bmatrix} \Gamma_r(t,0) & \Gamma_r(t,\tau_{1,2}) \\ \Gamma_r(t,-\tau_{1,2}) & \Gamma_r(t-\tau_{1,2},0) \end{bmatrix} \tag{A.7}$$

with $\Gamma_r(t,\tau)$ the autocovariance function of $r(t)$ and $\Gamma_{r_1,r_2}(t,\tau)$ the covariance function of $r_1(t)$ and $r_2(t)$.

The covariance matrix of this data model is now full-rank.

The rank of the RFI covariance matrix depends then on the number of interference signals impinging the antenna array, the amount of path each of them is following and on the kind of multipath effect they are subjected to (*fully* or *partially correlated*).

In a noise-free scenario, the rank of the covariance matrix $\mathbf{R}(t,\tau)$ is theoretically the sum of the rank of the cosmic sources covariance matrix $\mathbf{R_c}(t,\tau)$ and the rank of the interference covariance matrix $\mathbf{R_r}(t,\tau)$:

$$\text{Rank}(\mathbf{R}(t,\tau)) = \text{Rank}(\mathbf{R_c}(t,\tau)) + \text{Rank}(\mathbf{R_r}(t,\tau)) \tag{A.8}$$

However, in practice, the rank of $\mathbf{R}(t,\tau)$ also depends on the frequency bandwidth over which this matrix has been evaluated and on the signal's narrow band properties [109]. Indeed, consider the non-zero-bandwidth signal expressed in eq.2.2 impinging an antenna array radio telescope. It has been seen in section 2.2.1 that the propagation delay related to a narrow band signal $s(t)$ impinging an antenna array at an antenna l, and relative to an antenna k, has a frequency dependence ($e^{-j2\pi f_0 \tau_{kl}}$). The spatial signature of $s(t)$ is therefore time, frequency and direction dependent. If $\mathbf{a}_s(t, f_0, \theta, \phi)$ is the spatial signature related to the signal $s(t)$:

$$\mathbf{x}(t) = \mathbf{a}_s(t, f_0, \theta, \phi) s(t) \tag{A.9}$$

and if the subband of interest is larger than Δf, then the covariance matrix of $\mathbf{x}(t)$ is defined by:

$$\mathbf{R}(t,\tau) = \mathbb{E}\{s(t + \frac{\tau}{2}) s^*(t - \frac{\tau}{2})\} \int_{f_0 - \frac{\Delta f}{2}}^{f_0 + \frac{\Delta f}{2}} \mathbf{a}_s(t, f, \theta, \phi) \mathbf{a}_s^H(t, f, \theta, \phi) df \tag{A.10}$$

This resulting covariance matrix is clearly full-rank since it can be seen as an infinite sum of zero-bandwidth signal covariance matrices. The effective rank of a covariance matrix in a non-zeros-bandwidth case is defined as the amount of eigenvalues higher than the noise power in a noisy scenario.

On real data, the amount of signals impinging an antenna array radio telescope can therefore not be estimated using a rank analysis of the covariance matrix. However, other techniques allow this estimation, as will be seen in Chapter 5.

Appendix B

Noise coupling model

When the distance $d_{k,l}$ between antennas k and l of an antenna array radio telescope is large enough ($d_{k,l} \gg \lambda$, with λ the observed signal wavelength), the noise mutual coupling between the antennas can be neglected. The resulting noise covariance matrix $\mathbf{R_n}(t,\tau)$ is then diagonal. Moreover, if the array is calibrated, $\mathbf{R_n}(t,\tau)$ is expressed in the following way:

$$\mathbf{R_n}(t,\tau) = \sigma_n^2 \mathbf{I} \tag{B.1}$$

Unfortunately, the distance between the antennas of an array radio telescope is not always large enough. The noise mutual coupling can then be seen as a non-zero noise correlation between two (or more) antennas.

Many array signal processing techniques involving a matrix decomposition require a diagonal noise covariance matrix, as seen in this thesis. When this condition is not verified, the following two techniques can be applied to the radio telescope output covariance matrix $\mathbf{R}(t,\tau)$ in order to get rid of this disadvantage [20].

The first technique requires an estimate $\hat{\mathbf{R}}_\mathbf{n}(t,\tau)$ of $\mathbf{R_n}(t,\tau)$. Since the second order data model shown in eq.2.14 is additive, a noise covariance estimate could lead to a noise-free data covariance estimate, $\mathbf{R_{nf}}(t,\tau)$, simply by subtracting:

$$\mathbf{R_{nf}}(t,\tau) = \mathbf{R}(t,\tau) - \hat{\mathbf{R}}_\mathbf{n}(t,\tau) \tag{B.2}$$

However, subtracting the noise covariance matrix estimate from the antenna array covariance might result in the latter no longer being positive definite, and the positive definiteness of the covariance matrix is necessary for most of the interference techniques presented here. The second technique also requires an estimate of $\mathbf{R_n}(t,\tau)$. This technique consists in whitening $\mathbf{R}(t,\tau)$ in the following way:

$$\mathbf{R_w}(t,\tau) = \hat{\mathbf{R}}_\mathbf{n}(t,\tau)^{-\frac{1}{2}} \mathbf{R}(t,\tau) (\hat{\mathbf{R}}_\mathbf{n}(t,\tau)^{-\frac{1}{2}})^H \tag{B.3}$$

Applied to the covariance data model in eq.2.14, the noise covariance matrix of the whitened covariance matrix is now the identity matrix:

$$\mathbf{R_w}(t,\tau) = \hat{\mathbf{R}}_\mathbf{n}(t,\tau)^{-\frac{1}{2}}(\mathbf{A_c}\cdot\mathbf{R_c}(t,\tau)\cdot\mathbf{A_c}^H + \mathbf{A_r}\cdot\mathbf{R_r}(t,\tau)\cdot\mathbf{A_r}^H)(\hat{\mathbf{R}}_\mathbf{n}(t,\tau)^{-\frac{1}{2}})^H + \mathbf{I} \tag{B.4}$$

The Figure B.1 shows an example of the structure taken by a noise covariance matrix on the LOFAR Low Band Antenna array. The Figure B.1.(a) is the Power Spectral Density of the observation. The green point on this spectrum corresponds to an interference-free subband (centered at $f_0 \approx 46$ MHz), whereas the red point corresponds to a corrupted subband (centered at $f_1 \approx 21.7$ MHz, broadcasting frequency bandwidth).

The Figure B.1.(b) is the covariance matrix calculated at f_0. Since no interference impinges the antenna array at this frequency, the covariance matrix is a good approximation of the noise covariance matrix of the system. Its structure is diagonal.

The Figure B.1.(c) is the covariance matrix calculated at f_1. Since the considered subband is corrupted by an interference, the covariances between the antennas of the array are non-zero.

Figure B.2 is the same than Figure B.1, but with an observation made with the LOFAR High Band Antenna (regular antenna array). The corrupted subband considered here is centered at $f_0 \approx 139.6$ MHz, corresponding to an aviation or a land mobile signal.

Again, the covariance matrix is diagonal when no interference corrupts the observed subband.

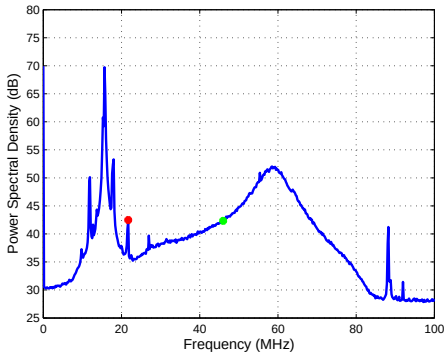

(a)

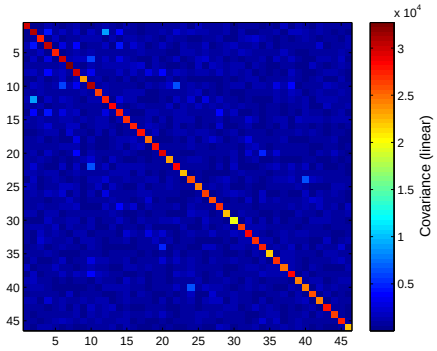

(b)

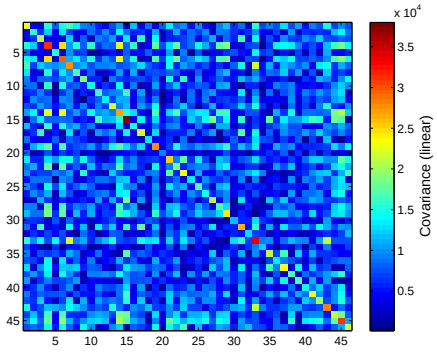

(c)

Figure B.1: Noise covariance structure example on real LOFAR Low Band Antenna data. 46-sub-antennas array, 512 subbands, 1024 samples. (a) Power Spectral Density of a LOFAR (single) Low Band Antenna observation. (b) Covariance matrix obtained at the frequency highlighted by a green point on Figure (a). (c) Covariance matrix obtained at the frequency highlighted by a red point on Figure (a).

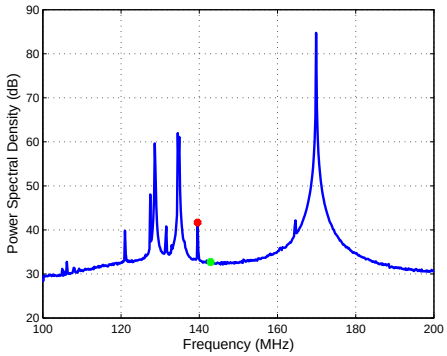

(a)

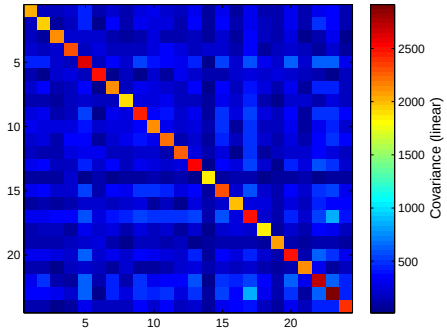

(b)

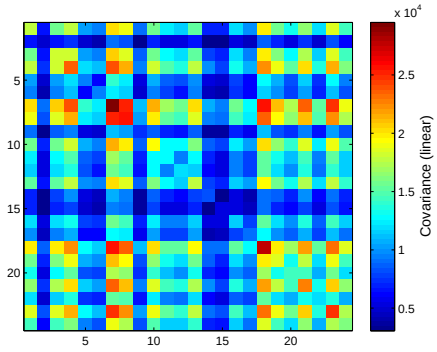

(c)

Figure B.2: Noise covariance structure example on real LOFAR High Band Antenna data. 24-sub-antennas array, 512 subbands, 1024 samples. (a) Power Spectral Density of a LOFAR (single) High Band Antenna observation. (b) Covariance matrix obtained at the frequency highlighted by a green point on Figure (a). (c) Covariance matrix obtained at the frequency highlighted by a red point on Figure (a).

List of Tables

List of Figures

Bibliography

[1] http://www.itu.int/.

[2] http://www.lofar.org/.

[3] http://www.skatelescope.org/.

[4] M. Abdalla, M. Abuitbel, and M. Hassan. Performance evaluation of direction of arrival estimation using music and esprit algorithms for mobile communication systems. In *Wireless and Mobile Networking Conference (WMNC), 2013 6th Joint IFIP*, pages 1–7, 2013.

[5] K. Abend and H. Subbaram. Interference suppression via orthogonal projections. In *Statistical Signal and Array Processing, 1992. Conference Proceedings., IEEE Sixth SP Workshop on*, pages 239–242, 1992.

[6] D. Ait-Allal, C. Dumez-Viou, R. Weber, G. Desvignes, I. Cognard, G. Theureau, et al. RFI mitigation at nançay observatory: Impulsive signal processing. In *Widefield Science and Technology for the SKA SKADS Conference 2009*, pages 201–205, 2010.

[7] D. A. Allal, R. Weber, I. Cognard, G. Desvignes, and G. Theureau. RFI mitigation in the context of pulsar coherent de-dispersion at the nançay radio astronomical observatory. 2009.

[8] R. Ambrosini, R. Beresford, A. Boonstra, S. Ellingson, K. Tapping, and Y. Terzian. RFI measurement protocol for candidate ska sites. *SKA Memo Series*, 2003.

[9] N. Arkind and B. Nadler. Parametric joint detection-estimation of the number of sources in array processing. In *Sensor Array and Multichannel Signal Processing Workshop (SAM), 2010 IEEE*, pages 269–272, 2010.

[10] W. Baan, P. Fridman, and R. Millenaar. Radio frequency interference mitigation at the westerbork synthesis radio telescope: Algorithms, test observations, and system implementation. *The Astronomical Journal*, 128(2):933, 2004.

[11] C. Barnbaum and R. F. Bradley. A new approach to interference excision in radio astronomy: Real-time adaptive cancellation. *The astronomical journal*, 116(5):2598, 1998.

[12] T. Bastian. Radio interferometry and fourier synthesis imaging. *High energy solar physics, SPD summer school, University of New Hampshire*, 2006.

[13] R. Behrens and L. Scharf. Signal processing applications of oblique projection operators. *Signal Processing, IEEE Transactions on*, 42(6):1413–1424, 1994.

[14] A. Belouchrani, K. Abed-Meraim, J.-F. Cardoso, and E. Moulines. A blind source separation technique using second-order statistics. *Signal Processing, IEEE Transactions on*, 45(2):434–444, 1997.

[15] J. Benesty, J. Chen, and Y. Huang. *Microphone array signal processing*, volume 1. Springer, 2008.

[16] P. Benthem and G. Kant. Embrace: Results from an aperture array for radio astronomy. In *Antennas and Propagation (EUCAP), 2012 6th European Conference on*, pages 629–633, 2012.

[17] P. Benthem, G. Kant, S. Wijnholds, M. Arts, R. Maaskant, M. Ruiter, and E. Van der Wal. Aperture array development for future large radio telescopes. In *Antennas and Propagation (EUCAP), Proceedings of the 5th European Conference on*, pages 2601–2605, 2011.

[18] A. Boonstra and S. Van der Tol. Spatial filtering of interfering signals at the initial low frequency array (lofar) phased array test station. *Radio science*, 40(5), 2005.

[19] A. Boonstra and R. Weber. RFI mitigation methods inventory. *SKADS DS4T3 Report*, 2009.

[20] A.-J. Boonstra. *Radio frequency interference mitigation in radio astronomy*. 2005.

[21] S. Bosse, S. Barth, S. Torchinsky, and B. Da Silva. Beamformer asic in uhf-l band for the square kilometer array international project. In *Microwave Integrated Circuits Conference (EuMIC), 2010 European*, pages 106–109. IEEE, 2010.

[22] S. Bretteil and R. Weber. Comparison of two cyclostationary detectors for radio frequency interference mitigation in radio astronomy. *Radio science*, 40(5), 2005.

[23] F. Briggs, J. Bell, and M. Kesteven. Removing radio interference from contaminated astronomical spectra using an independent reference signal and closure relations. *The Astronomical Journal*, 120(6):3351, 2000.

[24] F. Briggs and M. Kesteven. RFI subtraction with a reference horn: Application to pulsars and VLBI.

[25] J. Capon. High-resolution frequency-wavenumber spectrum analysis. *Proceedings of the IEEE*, 57(8):1408–1418, 1969.

[26] L. Castedo and A. R. Figueiras-Vidal. An adaptive beamforming technique based on cyclostationary signal properties. *Signal Processing, IEEE Transactions on*, 43(7):1637–1650, 1995.

[27] L. Castedo, C.-Y. Tseng, A. Figueiras-Vidal, and L. Griffiths. Linearly-constrained adaptive beamforming using cyclostationary signal properties. In *Acoustics, Speech, and Signal Processing, 1994. ICASSP-94., 1994 IEEE International Conference on*, volume 4, pages IV–249. IEEE, 1994.

[28] P. Comon, X. Luciani, and A. de Almeida. Tensor decompositions, alternating least squares and other tales. *Journal of Chemometrics*, 23:393–405, 2009.

[29] R. DeGroat, E. Dowling, and D. Linebarger. Subspace tracking. *The Digital Signal Processing Handbook*, 1998.

[30] J. W. Demmel. *Applied numerical linear algebra*. Siam, 1997.

[31] S. W. Ellingson. A study of adaptive canceling for microwave radiometry and spectrometry. *Rapport Technique*, pages 743467–1, 2002.

[32] S. W. Ellingson. Beamforming and interference canceling with very large wideband arrays. *Antennas and Propagation, IEEE Transactions on*, 51(6):1338–1346, 2003.

[33] S. W. Ellingson, J. D. Bunton, and J. F. Bell. Removal of the glonass c/a signal from oh spectral line observations using a parametric modeling technique. *The Astrophysical Journal Supplement Series*, 135(1):87, 2001.

[34] S. W. Ellingson and W. Cazemier. Efficient multibeam synthesis with interference ing for large arrays. *Antennas and Propagation, IEEE Transactions on*, 51(3):503–511, 2003.

[35] R. Feliachi. *Traitement spatial des interférences cyclostationnaires pour les radiotélescopes à réseau d'antennes phasé*. PhD thesis, Université d'Orléans, 2010.

[36] P. Fridman. Dsp experimental system for radio frequency interference mitigation at radio telescope. In *Proceedings of the IEEE NORDIC Signal Processing Symposium*, pages 13–15, 2000.

[37] P. Fridman. Statistically stable estimates of variance in radio-astronomy observations as tools for radio-frequency interference mitigation. *The Astronomical Journal*, 135(5):1810, 2008.

[38] P. Fridman and W. Baan. RFI mitigation methods in radio astronomy. *ASTRONOMY AND ASTROPHYSICS-BERLIN-*, 378(1):327–344, 2001.

[39] W. Fuxiang, L. Zhongkan, and Z. Jun. A new joint diagonalization algorithm with application in blind source separation. *Signal Processing Letters, IEEE*, 13(1):41–44, 2006.

[40] W. Gardner. Spectral correlation of modulated signals: Part i–analog modulation. *Communications, IEEE Transactions on*, 35(6):584–594, 1987.

[41] W. Gardner, W. Brown, and C.-K. Chen. Spectral correlation of modulated signals: Part ii–digital modulation. *Communications, IEEE Transactions on*, 35(6):595–601, 1987.

[42] W. Gardner and L. Franks. Characterization of cyclostationary random signal processes. *Information Theory, IEEE Transactions on*, 21(1):4–14, 1975.

[43] W. A. Gardner. Cyclic wiener filtering: theory and method. *Communications, IEEE Transactions on*, 41(1):151–163, 1993.

[44] W. A. Gardner, A. Napolitano, and L. Paura. Cyclostationarity: Half a century of research. *Signal processing*, 86(4):639–697, 2006.

[45] G. H. Golub and C. F. Van Loan. *Matrix computations. 1989.* Johns Hopkins University Press, Baltimore.

[46] J. Guerci. Theory and application of covariance matrix tapers for robust adaptive beamforming. *Signal Processing, IEEE Transactions on*, 47(4):977–985, 1999.

[47] A. Gunst and M. Bentum. The lofar phased array telescope system. In *Phased Array Systems and Technology (ARRAY), 2010 IEEE International Symposium on*, pages 632–639, 2010.

[48] I. Gupta and J. Ward. Effects of desired signal on the performance of a sidelobe canceller. *Antennas and Propagation, IEEE Transactions on*, 37(9):1109–1115, 1989.

[49] F. Haddock. Introduction to radio astronomy. *Proceedings of the IRE*, 46(1):3–12, 1958.

[50] C. K. Hansen, K. F. Warnick, B. D. Jeffs, J. R. Fisher, and R. Bradley. Interference mitigation using a focal plane array. *Radio science*, 40(5), 2005.

[51] F. J. Harris. On the use of windows for harmonic analysis with the discrete fourier transform. *Proceedings of the IEEE*, 66(1):51–83, 1978.

[52] S. Haykin. Array signal processing. *Englewood Cliffs, NJ, Prentice-Hall, Inc., 1985, 493 p. For individual items see A85-43961 to A85-43963.*, 1, 1985.

[53] S. S. Haykin. *Adaptive Filter Theory, 4/e.* Pearson Education India, 2005.

[54] G. Hellbourg, R. Weber, C. Capdessus, and A.-J. Boonstra. Oblique projection beamforming for RFI mitigation in radio astronomy. In *Statistical Signal Processing Workshop (SSP), 2012 IEEE*, pages 93–96, 2012.

[55] G. Hislop and C. Craeye. On the mathematical link between the music algorithm and interferometric imaging. *Antennas and Propagation, IEEE Transactions on*, 59(4):1412–1414, 2011.

[56] A. Hjorungnes and D. Gesbert. Complex-valued matrix differentiation: Techniques and key results. *Signal Processing, IEEE Transactions on*, 55(6):2740–2746, 2007.

[57] X. Huang, H.-C. Wu, and J. Principe. Robust blind beamforming algorithm using joint multiple matrix diagonalization. *Sensors Journal, IEEE*, 7(1):130–136, 2007.

[58] K. G. Jansky. Directional studies of atmospherics at high frequencies. *Proceedings of the Institute of Radio Engineers*, 20(12):1920–1932, 1932.

[59] Y. Jiao, J. Huang, and Y. Hou. Multidimensional music doa estimation using ant colony optimization algorithm. In *Signal Processing (ICSP), 2010 IEEE 10th International Conference on*, pages 291–294, 2010.

[60] J. Jonas. Threats to radio astronomy: now and the future. In *Communications and Signal Processing, 1998. COMSIG '98. Proceedings of the 1998 South African Symposium on*, pages 275–276, 1998.

[61] G. Kant, P. Patel, S. Wijnholds, M. Ruiter, and E. Van der Wal. Embrace: A multi-beam 20,000-element radio astronomical phased array antenna demonstrator. *Antennas and Propagation, IEEE Transactions on*, 59(6):1990–2003, 2011.

[62] L. Kogan. A minimum gradient algorithm for phased-array null formation. *Radio science*, 40(2), 2005.

[63] J. Kraus. *Radio Astronomy*. Cygnus Quasar Books; 2nd edition, 1986.

[64] H. Krim and M. Viberg. Sensor array signal processing: two decades later. 1995.

[65] H. Krim and M. Viberg. Two decades of array signal processing research: the parametric approach. *Signal Processing Magazine, IEEE*, 13(4):67–94, 1996.

[66] S. Kritchman and B. Nadler. Non-parametric detection of the number of signals: hypothesis testing and random matrix theory. *Signal Processing, IEEE Transactions on*, 57(10):3930–3941, 2009.

[67] A. Leshem, A. jan Van Der Veen, and A. jan Boonstra. Multichannel interference mitigation techniques in radio astronomy. In *in 2005, and the BYU Young Scholar Award (2007), and served as Technical Program Co-Chair for the 2007 IEEE International Symposium on Antennas and Propagation. Jonthan*. IEEE, 1972.

[68] A. Leshem and A.-J. van der Veen. Radio-astronomical imaging in the presence of strong radio interference. *Information Theory, IEEE Transactions on*, 46(5):1730–1747, 2000.

[69] A. Leshem and A.-J. van der Veen. Multichannel detection of gaussian signals with uncalibrated receivers. *Signal Processing Letters, IEEE*, 8(4):120–122, 2001.

[70] S. O. Lodge. *Signalling through space without wires*. Arno Press, 1974.

[71] J. Monari, F. Perini, S. Mariotti, G. Kant, J. Morawietz, and E. van der Wal. Embrace receiver design. *Image*, 17:1450MHz, 2010.

[72] B. Nadler. Nonparametric detection of signals by information theoretic criteria: performance analysis and an improved estimator. *Signal Processing, IEEE Transactions on*, 58(5):2746–2756, 2010.

[73] G. M. Nita, D. E. Gary, Z. Liu, G. J. Hurford, and S. M. White. Radio frequency interference excision using spectral-domain statistics. *Publications of the Astronomical Society of the Pacific*, 119(857):805–827, 2007.

[74] R. Nitzberg. Some properties of the multiple sidelobe canceller (mslc) perturbation beam. In *Signals, Systems and Computers, 1989. Twenty-Third Asilomar Conference on*, volume 1, pages 69–73, 1989.

[75] A. Offringa, A. de Bruyn, S. Zaroubi, G. van Diepen, O. Martinez-Ruby, P. Labropoulos, M. Brentjens, B. Ciardi, S. Daiboo, G. Harker, et al. The lofar radio environment. *arXiv preprint arXiv:1210.0393*, 2012.

[76] A. R. Offringa. *Algorithms for radio interference detection and removal*. University Library Groningen, 2012.

[77] A. R. Offringa, A. G. de Bruyn, M. Biehl, S. Zaroubi, G. Bernardi, and V. N. Pandey. Post-?correlation radio frequency interference classification methods. *Monthly Notices of the Royal Astronomical Society*, 405(1):155–167, June 2010.

[78] P. Picard, P. Renaud, C. Taffourau, V. Macaire, L. Mercier, and W. Paule. An overview of embrace station processing. 2010.

[79] B. Picinbono. On circularity. *Signal Processing, IEEE Transactions on*, 42(12):3473–3482, 1994.

[80] A. Poulsen, B. Jeffs, K. Warnick, and J. Fisher. Programmable real-time cancellation of glonass interference with the green bank telescope. *The Astronomical Journal*, 130(6):2916, 2005.

[81] K. J. Priya and D. A. Roshi. An experimental setup to develop RFI mitigation techniques for radio astronomy. *arXiv preprint astro-ph/0602270*, 2006.

[82] P. RAVIER and R. Weber. Détecteur robuste de signaux cyclostationnaires: application à la suppression d'interférences en radioastronomie. In *18 Colloque sur le traitement du signal et des images, FRA, 2001*. GRETSI, Groupe dEtudes du Traitement du Signal et des Images, 2001.

[83] J. Raza, A.-J. Boonstra, and A.-J. van der Veen. Spatial filtering of rf interference in radio astronomy. *Signal Processing Letters, IEEE*, 9(2):64–67, 2002.

[84] A. E. Rogers, P. Pratap, J. C. Carter, and M. A. Diaz. Radio frequency interference shielding and mitigation techniques for a sensitive search for the 327 mhz line of deuterium. *Radio science*, 40(5), 2005.

[85] R. Schmidt. Multiple emitter location and signal parameter estimation. *Antennas and Propagation, IEEE Transactions on*, 34(3):276–280, 1986.

[86] E. Serpedin, F. Panduru, I. Sarı, and G. B. Giannakis. Bibliography on cyclostationarity. *Signal Processing*, 85(12):2233–2303, 2005.

[87] B. Smolders and G. Hampson. Deterministic rf ing in phased arrays for the next generation of radio telescopes. *Antennas and Propagation Magazine, IEEE*, 44(4):13–22, 2002.

[88] L. E. Spence, A. J. Insel, and S. H. Friedberg. *Elementary Linear Algebra: A Matrix Approach*. Pearson/Prentice Hall, 2008.

[89] H. Subbaram and K. Abend. Interference suppression via orthogonal projections: a performance analysis. *Antennas and Propagation, IEEE Transactions on*, 41(9):1187–1194, 1993.

[90] A. Thompson, J. Moran, and G. Swenson. *Interferometry and Synthesis in Radio Astronomy*. John Wiley and Sons, New York; 1st edition, 1986.

[91] S. Torchinsky, A. Olofsson, A. Karastergiou, B. Censier, M. Serylak, P. Renaud, and C. Taffoureau. Characterization and initial results with embrace. In *SF2A-2013: Proceedings of the Annual meeting of the French Society of Astronomy and Astrophysics*, volume 1, pages 439–444, 2013.

[92] T. Trainini and E. Moreau. A least squares algorithm for global joint decomposition of complex matrix sets. In *Computational Advances in Multi-Sensor Adaptive Processing (CAMSAP), 2011 4th IEEE International Workshop on*, pages 313–316, 2011.

[93] S. van Der Tol and A.-J. van der Veen. Performance analysis of spatial filtering of rf interference in radio astronomy. *Signal Processing, IEEE Transactions on*, 53(3):896–910, 2005.

[94] A.-J. van der Veen. Joint diagonalization via subspace fitting techniques. In *Acoustics, Speech, and Signal Processing, 2001. Proceedings. (ICASSP '01). 2001 IEEE International Conference on*, volume 5, pages 2773–2776 vol.5, 2001.

[95] A.-J. van der Veen, A. Leshem, and A.-J. Boonstra. Signal processing for radio astronomical arrays. In *Sensor Array and Multichannel Signal Processing Workshop Proceedings, 2004*, pages 1–10, 2004.

[96] B. Van Veen. Minimum variance beamforming. *Adaptive radar detection and estimation*, pages 161–236, 1992.

[97] B. Van Veen and K. Buckley. Beamforming: a versatile approach to spatial filtering. *ASSP Magazine, IEEE*, 5(2):4–24, 1988.

[98] B. Van Veen and K. Buckley. Beamforming techniques for spatial filtering. *Digital Signal Processing Handbook*, pages 61–1, 1997.

[99] N. Varshney and R. Jain. An adaptive notch filter for narrow band interference removal. In *Communications (NCC), 2013 National Conference on*, pages 1–5. IEEE, 2013.

[100] M. Viberg and H. Krim. Two decades of statistical array processing. In *Signals, Systems & Computers, 1997. Conference Record of the Thirty-First Asilomar Conference on*, volume 1, pages 775–777. IEEE, 1997.

[101] M. Wax and T. Kailath. Detection of signals by information theoretic criteria. *Acoustics, Speech and Signal Processing, IEEE Transactions on*, 33(2):387–392, 1985.

[102] R. Weber, P. Zarka, V. Ryabov, R. Feliachi, J. Grießmeier, L. Denis, R. Kozhyn, V. Vinogradov, and P. Ravier. Data preprocessing for decametre wavelength exoplanet detection: an example of cyclostationary RFI detector. *Eusipco, Poznan, Poland*, 2007.

[103] B. Widrow and S. D. Stearns. *Adaptive signal processing*, volume 15. IET, 1985.

[104] S. Wijnholds, S. van der Tol, R. Nijboer, and A.-J. van der Veen. Calibration challenges for future radio telescopes. *Signal Processing Magazine, IEEE*, 27(1):30–42, 2010.

[105] T. Wilson, K. Rohlfs, and S. Httemeister. *Tools of Radio Astronomy*. Springer; 5th ed. 2009 edition, 2008.

[106] J. Winters. Optimum combining in digital mobile radio with cochannel interference. *Selected Areas in Communications, IEEE Journal on*, 2(4):528–539, 1984.

[107] W. Yuanyuan and C. Hao. A new algorithm based on joint diagonalization by the householder transformation for convolutive blind separation. In *Computer Science and Automation Engineering (CSAE), 2011 IEEE International Conference on*, volume 3, pages 348–352, 2011.

[108] P. Zarka, J. Queinnec, B. P. Ryabov, V. B. Ryabov, V. A. Shevchenko, A. V. Arkhipov, H. O. Rucker, L. Denis, A. Gerbault, P. Dierich, et al. Ground-based high sensitivity radio astronomy at decameter wavelengths. *Planetary Radio Emissions IV*, pages 101–127, 1997.

[109] M. Zatman. How narrow is narrowband? *IEE Proceedings-Radar, Sonar and Navigation*, 145(2):85–91, 1998.

[110] F. Zernike. The concept of degree of coherence and its application to optical problems. *Physica*, 5(8):785–795, 1938.

Grégory Hellbourg

Traitement spatial des interférences pour les radiotélescopes de nouvelle génération

La radio astronomie étudie les sources cosmiques au travers de leur rayonnement dans le domaine radio. Les astronomes, ustilisateurs passifs du spectre électromagnétique, ont à faire face à une pollution radio de plus en plus importante. Cette thse s'intéresse particulirement aux interférences radio d'origine humaine (RFI), et comment les observations radio astronomiques peuvent tre réalisées en bandes de fréquences non-protégées.
Les approches classiques consistent à contrller les paramtres statistiques d'une observation. Une fois détectées, les données polluées sont retirées avant post-traitement.
En plus d'autres avantages techniques par rapport aux radiotélescopes paraboliques classiques, les réseaux d'antennes offrent une information spatiale lors d'une observation astronomique. La diversité spatiale entre source cosmique d'intért (SCOI) et RFI peut tre exploitée pour développer des traitements spatiaux d'interférences.
Aprs la formulation d'un modle de données multidimensionnel, une technique de soustraction de sous espace RFI est introduite. Cette technique consiste à soustraire la contribution des RFI aux données d'une observation.
La projection orthogonal a déjà été considérée auparavant. Cependant, l'orthogonalité requise entre CSOI et RFI pour retrouver une source d'intéret non biaisée ne peut vraisemblablement pas tre satisfaite. Une approche basée sur une porjection oblique est introduite afin de pallier à cette condition.
Les techniques de projections sont comparées au techniques classiques de beamforming en termes de réjection de l'interference et de récupération de la source d'intért.
Le sous-espace RFI est inconnu de manire générale et se doit d'tre estimé. Plusieurs techniques permettant cette estimation, basées sur des propriétés statistiques des RFI et sources cosmiques, sont également présentées et comparées.
Les différentes techniques ont été appliquées à des données astronomiques délivrées par le radio télescope Européen LOFAR.
Enfin, une implémentation d'un algorithme de traitement spatial d'interférences sur le démonstrateur EMBRACE est présenté.
Mots clés : Suppression d'interférences, Réseaux d'antennes, Cycostationarité, Radioastronomie

Radio Frequency Interference spatial processing for modern radio telescopes

Radio astronomy studies cosmic sources through their radio emissions. As passive users, astronomers have to deal with an increasingly corrupted radio spectrum. The research presented here focuses on man-made Radio Frequency Interference (RFI), and how astronomical observations can be performed in non-protected frequency bands.
Traditional approaches consist in monitoring radio telescopes output data through statistical parameters. Once detected, the corrupted data is removed before further processing.
Besides other technical advantages compared to single dish radio telescopes, antenna arrays provide spatial information about astronomical observations. The spatial diversity between cosmic sources-of-interest (CSOI) and RFI can be exploited to develop spatial RFI processing.
After formulating a multidimensional radio astronomical data model, an interference subspace subtraction technique is introduced. This approach consists in subtracting RFI contributions from antenna array radio telescopes data.
Orthogonal projection applied to astronomical observation vector spaces has already been considered by the past. The orthogonality between RFI and CSOI subspaces is required to recover the CSOI without bias. In order to avoid this latter requirement, an oblique projection approach is here proposed.
The projection techniques are compared to classic beamforming techniques in term of interference rejection and CSOI recovering.
Being usually unknown, the RFI subspace has to be estimated. Several techniques allowing this estimation, based on statistical properties of RFI and cosmic sources (whiteness and cyclostationarity), are also presented and compared.
The different techniques have been applied to real astronomical data, provided by the European radio telescope LOFAR.
A last section presents an RFI mitigation algorithm implemented on the demonstrator EMBRACE.
Keywords : RFI mitigation, Antenna arrays, Cyclostationarity, Radio astronomy

Centre Val de Loire UNIVERSITÉ Spirit of the Loire Valley

Laboratoire PRISME (France)
CNRS (France)
ASTRON (The Netherlands)

UNIVERSITE D'ORLEANS